ISSN 0469-4732

(1)

INSTITUTE OF PLASMA PHYSICS

NAGOYA UNIVERSITY

Proceedings of the US-Japan Workshop
on
Advanced Plasma Modeling II
March 23-27, 1987
Nagoya, Japan

(Received — Mar. 1, 1988)

IPPJ- 863 Mar. 1988

RESEARCH REPORT

NAGOYA, JAPAN

Proceedings of the US-Japan Workshop

on

Advanced Plasma Modeling II

March 23-27, 1987

Nagoya, Japan

Further communication about this report is to be sent to the Research Information Center, Institute of Plasma Physics, Nagoya University, Nagoya 464, Japan.

Preface

"The Second U.S.-Japan Workshop on Advanced Plasma Modeling" meet at IPP Nagoya from March 23-27th, 1987. The program for the meeting is attached as appendix I.

There were seven American participants and 26 Japanese participants;the list of participants is attached as appendix II.

We consider that this workshop was very successful. There was lively discussion from both sides on detail of modeling techniques, their advantages and disadvantages, how they might be improved and what types of physics problems could be treated. It was clear that Japanese-U.S.collaboration has played a large role in developing many powerful new techniques for handling large time step large space scale problems. There were also developments that took place in one country or the other and it was clear that the participants learned a lot from hearing of each others work. We have drawn a number of conclusion from this workshop.

J.M. Dawson

T. Kamimura

Summary

Gyrokinetic Particle Simulation

The numerical properties of a gyrokinetic plasma have been discussed in detail in this workshop. It is generally agreed that considerable improvement in time step, grid spacing and noise level can indeed be realized with the present model. Numerical schemes for solving the nonlinear gyrokinetic equations have also been presented. The consensus is that the treatment of the electron motion parallel to the magnetic field is very crucial. The proposed sub-cycling scheme should be examined carefully.

With the arrival of the present generation of super-computers, Prof. Dawson feels very strongly that it is the time has come for us to work actively toward the realistic simulation of tokamak discharges with particle codes — gyrokinetic or implicit. However, there are numerous important issues one has to resolve before achieving that goal, such as particle re-cycling techniques, 3D diagnostics, the MHD equilibrium problem, the development of collision operators and the choice of the appropriate coordinate systems for the simulation. Another important aspect is the inclusion of the "kitchen physics" in the code.

In view of the man power shortage in this area, Profs. Dawson and Kamimura have proposed a collaboration effort between the US and Japan. The initial phase of this joint endeavor will start this summer at UCLA.

W. W. Lee

US-Japan Workshop on Advanced Plasma Modeling

March 23-27, 1987

IPP, Nagoya, Japan

A G E N D A

March 23 (Monday)

Registration (9:30)

Opening Remarks (10:00-10:20)
J. M. Dawson and T. Kamimura

Morning Session (10:20-12:30) Chairman I. Kawakami

A. Aydemir(IFS) : Generalized Reduced MHD and Full MHD Calculations with Semi-Implicit Techniques

D. D. Schnack(SAI) : Semi-Implicit Methods for 3D MHD Computations

G. Kurita(JAERI) : Nonlinear Evolution of Free Boundary Modes in Tokamak

Lunch (12:30-14:00)

Afternoon Session ① (14:00-15:30) Chairman: A. Aydemir

T. Hayashi(HIFT) : 3D-Equilibrium and Stability code of Helical System

T. Hayashi(HIFT) : A Simulation of Driven Reconnection by a high precision MHD code

Coffee Break (15:30-15:45)

Afternoon Session ② (15:45-17:15) Chairman: G. Kurita

T. Ogino (Nagoya Univ.) : An MHD Simulation Of the Solar Wind and Cometary Plasma (An MHD Model with Plasma Production)

C. Z. Cheng(PPPL) : NOVA-2: A Kinetic MHD Stability Code

March 24 (Tuesday)

Morning Session ① (9:15-10:50) Chairman: H. Abe

J.M.Dawson(UCLA) : A Hybrid Vlasov-Fluid Model with Kinetic Ions and Massless Fluid Electrons

W.W.Lee(PPPL) : Gyrokinetic Particle Simulation of Finite-Beta Plasma

Coffee Break (10:50-11:00)

Morning Session ② (11:00-12:30) Chairman: C.Z.Cheng

M.Tanaka(HIFT) : Macroscale Particle Simulation of Kinetic Alfven Waves (Code Description and Application)

A.Friedman(LLL) : Advanced Particle-in-cell Plasma Modeling at LLNL

Lunch (12:30-14:00)

Afternoon Session ① (14:00-15:50) Chairman: M.Tanaka

K.Nishihara (Osaka Univ.) : Particle-Particle Particle-Mesh code for Nonideal High Density Plasma and Its Application on Rayleigh-Taylor Instability in ICF Plasma

S.Kawata (Nagaoka Tec.) : TRIPIC: Triangular-Mesh PIC code for LIB Diode Simulation

S.Y.Kim (KIT, Korea) : Particle Simulation Technique using FEM Methods

Coffee Break (15:50-16:00)

Afternoon Session ② (16:00-17:30) Chairman: M.Aizawa

K.Miki (Hitachi Ltd.) : A Domain Decomposition and Overlapping Method for 3D Large Scale Numerical Simulation

R.Sydora(UCLA) : Subtraction Technique for Plasma Physics and Evaluation of Numerical Effects in Codes

Group Dinner (18:30-)

March 25 (Wednesday)

Morning Session (9:15-10:50) Chairman: T. Ogino

A. Friedman(LLL) : Numerically Induced Stochasticity

T. Yabe(Osaka Univ.) : Reduced Atomic Model for Calculation of Charge Distribution in Multiply-Charged Plasma

Working Time for Discussion Leaders and Group Photo (10:50-11:30)

Lunch (11:30-13:00)

……

Discussion and Working Sessions ① (13:00-17:30)

① Advanced MHD Model (13:00-15:00)
Discussion Leaders: T. Hayashi and D. D. Schnack

comments: I. Kawakami, T. Ogino, and T. Hayashi

Coffee Break (15:00-15:30)

② Implicit Particle Model (15:30-17:30)
Discussion Leaders: K. Nishihara and A. Friedman

comments: T. Kamimura, H. Abe, M. Tanaka, A. Friedman, and W. W. Lee

March 26 (Thursday)

Discussion and Working Sessions ② (9:15-15:00)

③ Gyrokinetic Particle Model (9:15-11:15)
Discussion Leaders: H. Naitou and W. W. Lee

comments: W. W. Lee and J. M. Dawson

Coffee Break (11:15-11:30)

④-1 Improvement of Simulation Model (11:30-12:30)
Discussion Leaders: T.Yabe, I.Katanuma, and R.Sydora

comments: S.Takeuchi, K.Hanatani, and Y.Abe

Lunch (12:30-14:00)

④-2 Continuation (14:00-15:00)

……

Summary and Conclusions (15:00-16:00)

Co-chairmen : J.M.Dawson and T.Kamimura

March 27 (Friday)

Working Session

Closing

……

The maximum time allowed for speakers including discussions;
(40 - 45) min. for the oral presentations
(10 - 15) min. for comments

List of Participants
US-Japan Workshop on Advanced Plasma modeling
March 23-27, 1987
IPP, Nagoya, Japan

U.S.A.

Dawson John M.	University of California, Los Angeles Department of Physics 405 Hilgard Ave. Los Angeles, Calif. 90024
Aydemir Ahmet	University of Texas Austin Institute for Fusion Studies Austin, Texas 78712
Cheng C.Z.	Plasma Physics Laboratory Princeton University P.O. Box 451, Princeton, N.J. 08544
Friedman Alex	University of California Lawrence Livermore Lab. P.O. Box 808, Livermore CA. 94550
Lee W.W.	Plasma Physics Laboratory Princeton University P.O. Box 451, Princeton, N.J. 08544
Schnack Dalton.D.	Science Applications International Corp. San Diego, Calif. 92121
Sydora Richard	University of California, Los Angeles Department of Physics 405 Hilgard Ave. Los Angeles, Calif. 90024

JAPAN

Abe Hirotada	Dept. of Engineering Kyoto Univ., Kyoto 606
Abe Yoshihiko	Institute of Plasma Physics Nagoya Univ., Nagoya 464
Aizawa Masamitsu	Atomic Energy Research Institute College of Science & Technology Nihon Univ., Tokyo 101
Amano Tsuneo	Institute of Plasma Physics Nagoya Univ., Nagoya 464
Hanatani Kiyoshi	Plasma Physics Laboratory Kyoto Univ., Gokasho, Uji, Kyoto 611
Hayashi Takaya	Institute for Fusion Theory Hiroshima Univ., Hiroshima 730
Ichiguchi Katsuji	Plasma Physics Laboratory Kyoto Univ., Gokasho, Uji, Kyoto 611
Ichikawa Yoshi H.	Institute of Plasma Physics Nagoya Univ., Nagoya 464
Ishiguro Seiji	Institute of Plasma Physics Nagoya Univ., Nagoya 464
Kamimura Tetsuo	Institute of Plasma Physics Nagoya Univ., Nagoya 464
Katanuma Isao	Institute of Applied Physics Plasma Research Center Univ. of Tsukuba, Ibaraki 305
Kawakami Ichiro	College of Science & Technology Nihon Univ., Tokyo 101

Kawata Shigeo — Technological Univ. of Nagaoka
Nagaoka, Niigata, 940-21

Kurita Genichi — Japan Atomic Energy Research Institue
Tokai Research Establishment
Ibaraki 319-11

Miki Kazuyoshi — Energy Research Laboratory
Hitachi, Ltd.,
Hitachi-shi, Ibaraki, 316

Mizuno Yukio — Institute of Plasma Physics
Nagoya Univ., Nagoya 464

Naitou Hiroshi — Institute of Plasma Physics
Nagoya Univ., Nagoya 464

Nakajima Noriyoshi — Institute of Plasma Physics
Nagoya Univ., Nagoya 464

Nishihara Katsunobu — Institute of Laser Engineering
Osaka Univ., Suita 565

Ogino Tatsuki — Research Institute of Atmospherics
Nagoya Univ., Toyokawa 442

Takemoto Yukimasa — Institute of Plasma Physics
Nagoya Univ., Nagoya 464

Takeuchi Satoshi — Faculty of Engineering
Yamanashi Univ., Kofu 400

Tanaka Motohiko — Institute for Fusion Theory
Hiroshima Univ., Hiroshima 730

Terashima Yoshinosuke
Institute of Plasma Physics
Nagoya Univ., Nagoya 464

Wakatani Masahiro Plasma Physics Laboratory
Kyoto Univ., Gokasho, Uji, Kyoto 611

Yabe Takashi Institute of Laser Engineering
Osaka Univ., Suita 565

Observers

U.S.A.

Horton Wendell University of Texas, Austin
Institute for Fusion Studies
Austin, Texas 78712

Sadowski Walter. D.O.E.

KOREA

Kim Soo Yong Korea Institute of Technology
Department of Physics
400 Kusong-dong Chung-gu Taejon-shi
Chung chong nam-do Korea

EGYPT

Makar Malak N. Assuit National Univ.
Dept. of Mathematics
Assuit, Egypt

GENERALIZED REDUCED MHD, AND FULL MHD CALCULATIONS WITH SEMI-IMPLICIT TECHNIQUES

A. Aydemir

University of Texas Austin
Institute for Fusion Studies
Austin, Texas 78712

The Four-Field model of Hazeltine, et al[1], generalizes the well-known reduced MHD (RMHD) equation to include parallel and perpendicular compressibility, diamagnetic dift frequencies, and pressure gradients in the parallel Ohm's law. This model is applied to the study of drift-tearing modes in tokamaks; newly-found Alfvén-resonant modes[2] are discussed. Applications of recently-developed semi-implicit techniques[3] for efficient treatment of shear Alfvén waves, ion sound waves, and semi-collisional terms are presented.

semi-implicit techniques are discussed in the context of non-reduced, full MHD equations also. Fully toroidal, linear and nonlinear studies of m = 1 modes in tokamaks are presented and discussed in terms of their application to fast saw-tooth crashes.

(1) R.D. Hazeltine. et al, Phys. Fluids, 28, 2466 (1985).

(2) A.V. Aydemir. et al, Phys. Fluids, 30, 4(1987).

(3) D.S. Harred, and D.D. Schnack, J. Comp. Phys. (1986).

SEMI-IMPLICIT METHODS FOR 3-D MHD COMPUTATIONS

D.D. Schnack

Science Applications International Corp.
San Diego, Calif. 92121

Nonlinear MHD systems often evolve on time scales that are long compared to those associated with the fastest normal modes of the system. Stability restrictions placed on explicit temporal approximations may result in uneconomically small time steps, while the fully implicit treatment of nonlinear terms requires iteration, or results in unacceptably large matrices. Recently, a new class of methods for solving the time-dependent MHD equations, based on an algorithm developed for long-range weather simulation, has been introduced. These semi-implicit methods allow very large time steps, yet avoid the complexity and large memory requirements associated with implicit methods. In the semi-implicit methods for MHD new terms are added to the time-discretized equations that do not affect the consistency of the solution, yet provide a simple and efficient means of enhancing stability. This method is unconditionally stable with respect to all Alfven modes, and consequently permits such large time steps that accuracy becomes the most important consideration in the chioice of step size. The semi-implicit method may be implemented using a variety of different time advance schemes and choices for the semi-implicit terms. The proper choices can lead to improved efficiency and accuracy for long-time scale 3-d nonlinear MHD computations. Examples of such simulations of fusion devices (tokamaks and RFPs) and the solar corona are presented.

NONLINEAR EVOLUTION OF FREE BOUNDARY MODE IN A TOKAMAK

Gen ichi KURITA, Tomonori TAKIZUKA, Masafumi AZUMI
and Tatsuoki TAKEDA

Department of Thermonuclear Fusion Research
Naka Fusion Research Establishment
Japan Atomic Energy Research Institute
Naka-machi, Naka-gun, Ibaraki-ken

Nonlinear MHD calculations of the m/n=2/1 free-boundary mode including tearing mode in a cylindrical tokamak are carried out by taking account of the parallel diffusion of resistivity. When $1.75<q_a\lesssim 1.9$ for $q_0/q_a=0.5$ (q_0 is the safety factor at the magnetic axis and q_a is that at the plasma surface), the plasma column shrinks with the elliptic deformation, the value of q_a is decreased in time, the plasma becomes stable against the m/n 2/1 mode, and finally damping oscillation is observed. The vacuum bubbles inside the plasma are formed for $1.9\lesssim q_a<2.$ due to free-boundary kink mode and for $2.0\leqq q_a\lesssim 2.25$ due to surface tearing mode, respectively. The saturation of magnetic islands are observed for $2.25\lesssim q_a\lesssim 2.4$ due to surface tearing mode with plasma expansion and for higher q_a values due to usual tearing mode with fixed plasma surface position, respectively. Interaction between the plasma and material limiter causes the shrinkage for all the unstable values of q_a to free-boundary mode. When q_0 is nearly equal to or larger than unity, the plasma shrinks rapidly and q_a can be reduced less than unity below which the m/n=1/1 kink mode becomes unstable. This plasma shrinkage is a candidate of the major disruptions in the tokamak discharge with q_a around 2.

1. INTRODUCTION

In the tokamak discharges with q_a nearly equal to 2, some major disruptions are observed which limit the maximum plasma current [1,2]. The m/n=2/1 tearing mode (m and n are the poloidal and toroidal mode numbers, respectively) is considered to play an importnat role in this major disruption process. This disruption process has been studied by numerical calculations [3,4,5]. The m/n=2/1 free boundary kink mode is also considered to play an importnat role in the major disruption. The following scenario has been supposed: The plasma deforms elliptically due to the growth of the kink mode and the deformation is saturated by the negative surface current. With the dissipation of the surface current due to the plasma limiter interaction [6] or due to high electric resistivity near the plasma surface [7], however, the deformation continues to grow and the current disruption is caused. A new scenaroi of the disruption has been presented by Kurita et al. [8] by means of numerical calculaiton of the m/n=2/1 free-boundary kink modes, where the resistivity evolution including parallel diffusion is considered. The plasma is deformed by the interaction with the limiter. This shrinkage may cause the major disruption. The plasma deformation by the m/n=2/1 surface tearing mode has been also presented by Kurita et al. [9]. In this report we review these results and present detailed results of numerical calculations. In section 2, basic equations are described. The linear stability of free boundary modes and tearing mode including resistivity equation with finite parallel diffusion is analysed in section 3. The results of nonlinear evolutions are shown in section 4, and summary and discussion are given in section 5.

2. BASIC EQUATIONS

As basic equations, we employ the single helicity reduced set of resistive MHD equations of a low beta cylindrical plasma including the resistivity evolution equation. Fourier expanded equations in poloidal and toroidal directions are written as follows:

$$\frac{\partial \Psi_{m/n}}{\partial t} = [\Psi,\Phi]_{m/n} + \sum_{m=m'+m''n=n'+n''}\sum \eta_{m'/n'}J_{m''/n''} - E^w\delta_{m0}\delta_{n0} \quad , \tag{1}$$

$$\frac{\partial U_{m/n}}{\partial t} = [U,\Phi]_{m/n} + [J,\Psi]_{m/n} \quad , \tag{2}$$

$$\frac{\partial \eta_{m/n}}{\partial t} = [\eta,\Phi]_{m/n} - \kappa_{\parallel}[\nabla_{\parallel}\eta,\Psi]_{m/n} + \kappa_{\perp}\Delta\eta_{m/n} \quad , \tag{3}$$

$$U_{m/n} = \Delta\Phi_{m/n} \quad , \tag{4}$$

$$J_{m/n} = \Delta\Psi_{m/n} + 2R_{\hat{m}/\hat{n}}\delta_{m0}\delta_{n0} \quad , \tag{5}$$

$$[X,Y]_{m/n} \equiv \sum_{m=m'+m''n=n'+n''}\sum \frac{m'}{r}\left(X_{m'/n'}\frac{\partial Y_{m''/n''}}{\partial r} - Y_{m'/n'}\frac{\partial X_{m''/n''}}{\partial r}\right) \quad , \tag{6}$$

$\Psi_{m/n}$ is the helical poloidal magnetic flux, $\Phi_{m/n}$ the stream function, $\eta_{m/n}$ the resistivity, $J_{m/n}$ the current density, $U_{m/n}$ the vorticity, E^w the electric field at the wall, δ_{ij} the Kronecker delta and $R_{\hat{m}/\hat{n}}$ is the ratio of $\hat{m}/\hat{n}$, where $\hat{m}$ and $\hat{n}$ are the Fourier mode numbers of our interest. In these equations, the uniform plasma density is assumed, and the time is normalized by the poloidal Alfvén transit time $\tau_{pa}=B_t/\sqrt{\rho}R$ (B_t is the toroidal magnetic field, ρ the plasma density, and R the major radius). Other normalization factors are $\sqrt{\rho}R/(B_t b^2)$ (b is the shell radius) for η and $\sqrt{\rho}R/(B_t R^2)$ for $\kappa_{\parallel}$.

The resistivity is assumed to follow the same equation as that for the electron temperature. The parallel diffusion coefficient of resistivity, $\kappa_{\parallel}$, and perpendicular one, $\kappa_{\perp}$, are assumed to be uniform for simplicity. The parallel gradient of η is defined as $(\nabla_{\parallel}\eta)_{m/n}=[\eta,\Psi]_{m/n}$. To calculate

the free-boundary problem, we use the 'pseudo-vacuum' model, where the vacuum is replaced by the plasma with high resistivity. This method has been successfully applied to nonlinear simulations of free-boundary modes [10,11]. The above set of nonlinear equations is solved by the predictor-corrector time integration scheme. The diffusion terms in Eqs.(1) and (3) are approximated by the implicit representation. These implicit parts of nonlinear calculation spend almost CPU time of the computer. The equation for resistivity, Eq.(3), including the diffusion term is solved by a mapping method. In this method, the radial plasma displacement, S, is solved instead of resistivity equation, that is,

$$\frac{\partial S}{\partial t} = [S,\varphi] - \kappa_{\parallel}\left[[\nabla_{\parallel}\eta,\Psi] + \frac{\eta''}{\eta'}(\nabla_{\parallel}\eta)^2\right] + \kappa_{\perp}\Delta^{*}S \tag{7}$$

The additional term, $(\eta''/\eta')(\nabla_{\parallel}\eta)^2$, is appeared by the variable transformation of $\eta \rightarrow S$, and plays a very important role in the resistivity evolution of free-boundary case. Obtaining new $S_{m/n}$ and Fourier-composed $\hat{S}(r,\theta)$, we calculate $\hat{\eta}(r,\theta)$ by a mapping,

$$\hat{\eta}(\hat{S},\theta) \equiv \hat{\eta}(\hat{S}_{t=0},\theta) \;\; ; \;\; \hat{S}_{t=0}=r. \tag{8}$$

After expandeing $\hat{\eta}(r,\theta)$ in Fourier series, we can calculate the right hand side of Eq.(1), and can advance the time step. By this procedure, the resistivity is always kept positive at all grid points, which is necessary to integrate Eq.(1) in time without numerical instability [10].

3. LINEAR STABILITY ANALYSIS

In this section, we investigate the effect of parallel diffusion on the linear stability of tearing mode and free-boundary modes; kink and surface tearing modes [10,12]. From Eqs.(1)~(6), the following linearized reduced set of resistive MHD equations is derived,

$$\gamma\Delta\Phi = F\Delta\Psi - \frac{m}{r}\frac{dJ_{eq}}{dr}\Psi \;, \tag{9}$$

$$\gamma\Psi = -F\Phi + \eta_{eq}\Delta\Psi + \eta J_{eq} \;, \tag{10}$$

$$\gamma\eta = -\frac{m}{r}\frac{d\eta_{eq}}{dr}\Phi + \kappa_{\parallel}F\left(\frac{m}{r}\frac{d\eta_{eq}}{dr}\Psi - F\eta\right) \;, \tag{11}$$

$$F = \frac{1}{q}(m-nq) \;, \tag{12}$$

where q is the safety factor, subscript 'eq' means equilibrium quantities, and the time derivatives are replaced by the growth rate, γ. The perpendicular diffusion is negligibly small in general. Since the singular surface ($F=0$) does not exist in the plasma region for the kink mode ($q_a<m/n$), $\gamma\Psi \cong -F\Phi$ holds and Eq.(11) becomes

$$\left(1 + \frac{\kappa_{\parallel}F^2}{\gamma}\right)\left(\gamma\eta + \frac{m}{r}\frac{d\eta_{eq}}{dr}\Phi\right) \cong 0 \;. \tag{13}$$

This relation implies that the parallel diffusion scarcely affects the kink mode in the linear stage. The ratio of the plasma radius, a, to the wall radius, b, is $a/b=0.66$. The resistivity, $\eta_{eq}(r)$, is inversely proportional to $J_{eq}(r)$ with $\eta_{eq}(0)=10^{-6}$ and $\eta_{eq}(b)=1$. The profile of current density is chosen as

$$J_{eq}(r) = \{ J_{eq}(0) - J_{eq}(b) \}\{ 1 - (r/a)^{3.56} \}^2 + J_{eq}(b), \qquad (14)$$

for $0 \leqq r \leqq a$, and $J_{eq}(r) = J_{eq}(b) = J_{eq}(0)\eta_{eq}(0)/\eta_{eq}(b)$ for $a < r \leqq b$. The ratio, q_0/q_a, is 0.5 for this current profile, and the value of $J_{eq}(0)$ is determined by the value of q_0. In Fig.1, the graph of linear growth rate versus q_a for three values of $\kappa_\parallel$ is shown by three solid curves. The dependence to $\kappa_\parallel$ is small in free-boundary kink mode region ($q_a \leq 2$) as indicated by Eq.(13). Numerical calculations of the eigenvalue problem support above prediction. The growth rate of the kink mode is smoothly connected to that of the "surface tearing mode" in the $q_a \geqq 2$ region [12]. The growth rate for higher $\kappa_\parallel$ value is higher than that of lower $\kappa_\parallel$ at q_a around 2. This relation is inverted in the surface tearing mode region, and the growth rate for higher $\kappa_\parallel$ becomes smaller than that of lower case. For sufficiently large $\kappa_\parallel$ value, the growth rate of tearing mode with resistivity perturbation tends to that without resistivity perturbation ($\eta = const.$) shown by the broken curve in the figure. This result is consistent to that in Refs.[13,14]. The relatively large value of the linear growth rate at $q_a \cong 2.0$ is attributed to finite and relatively large plasma resistivity near the singular surface, details of which will be presented elsewhere. The parallel diffusion of resistivity becomes very important in the nonlinear phase, especially in the phase of the interaction between plasma and limiter.

4. NONLINEAR CALCULATIONS

In this section, we carry out nonlinear calculations of the m/n=2/1 free-boundary mode including tearing mode for the cases (4.a) without a limiter and (4.b) with a limiter. The initial profile of current density is given by Eq.(14) ($q_0/q_a|_{t=0}=0.5$). Total plasma current is assumed to be constant in time. The resistivity at $t=0$ is determined as $\eta(r)=E^w/J(r)$ with $\eta(0)=10^{-6}$ and $\eta(b)=1$. We choose, in the following calculations, the initial plasma radius, a_0, as $a_0/b=0.66$. The parallel diffusion coefficient, $\kappa_\parallel$ is set 10^2, and $\kappa_\perp=10^{-8}$. The nonuniformity of η on a magnetic surface disappears within the time interval of about 0.1 due to the diffusion of $\kappa_\parallel=10^2$. This value of $\kappa_\parallel$ corresponds to the following actual parameters; toroidal magnetic field $B_t=4$ T, major radius R=1 m, electron temperature $T_e=1$ keV, and plasma density $n=10^{20}$ m^{-3}. Number of Fourier components, M, and radial meshes, N_r, are typically M=10 and $N_r=200$.

4.a Case without limiter

The nonlinear evolutions without limiter are studied at first for various initial values of $q_{a0}=q_a(t=0)$; (a) $q_{a0}=1.85$, (b) $q_{a0}=1.95$, (c) $q_{a0}=2.05$, (d) $q_{a0}=2.15$, and (e) $q_{a0}=2.5$. Figures 2 and 3 show the time evolutions of Ψ-contour for $q_{a0}=1.85$ and $q_{a0}=1.95$, respectively. The bold line in the figure represents crowded resistivity contours which correspond to the approximate position of the plasma surface. For $q_{a0}=1.85$, the elliptic deformation grows with the shrinkage of the plasma column ($0 < t \lesssim 100$). Since the plasma current is constant, this shinkage makes q_a value smaller from 1.85 to 1.25, and the plasma becomes linearly stable against the m/n=2/1 kink mode. Finally the damping oscillation of the shrunk plasma is observed ($t \gtrsim 100$). The radius of each shrunk plasma with circular cross section is $0.95a_0$ for $q_{a0}=1.75$, $0.85a_0$ for $q_{a0}=1.8$ and $0.80a_0$ for $q_{a0}=1.85$. The shrinkage of the plasma column is caused by the following processes. An η-contour in a resistive plasma crosses Ψ-contours near the plasma surface due to the convection, and the plasma periphery connected with the vacuum region is drastically cooled by the parallel thermal conduction. It is to be noted for the case of $\kappa_\parallel=0$ that the plasma area is conserved and the saturation state with elliptic deformation can be realized [10].

On the other hand, for larger q_{a0} value (q_{a0}~1.95), the vacuum bubbles are formed by the free boundary kink mode, as shown in Fig.3, even for such a decreasing current profile ($q_0/q_a|_{t=0}=0.5$). The hot plasma flows out into the "pseudo-vacuum" region along the magnetic fild line and the vacuum region penetrates into the plasma to form the vacuum bubbles. It was shown by Rosenbluth et al. that the saturation state of the ideal kink mode is the elliptic deformation for the parabolic current profile [15]. The vacuum bubbles were found to be formed by the surface tearing mode in a resistive plasma for $q_{a0}>2$ and $q_0/q_a|_{t=0}=0.5$ [10]. The bubble formation by the free boundary kink mode for the initial condition of $q_a=1.85$ and $q_0=1.2$ has been found by Dnestrovskii et al. using the "heating" model for the transport of η in which the convection of plasma boundary is not considered [11]. The transition from the formation of vacuum bubbles to the shrinkage with elliptic deformation occurs between the q_{a0} values of 1.85 and 1.9 for this current profile. The current profile determines this transition point, but the detailed mechanism or the criterion of this transition is not clarified yet.

When q_{a0} becomes larger than 2, the formation of vacuum bubbles by the surface tearing mode is observed even for finite $\kappa_\parallel$ value just the same as for the case of no $\kappa_\parallel$ [10]. This bubble formation occurs in the following process; First, the plasma boundary touches the magnetic islands formed inside of the plasma due to the horizontal plasma flow. Because of finite large $\kappa_\parallel$, the cold plasma in the vacuum flows into the hot plasma along the magnetic field line instantaneously and the magnetic islands with plasma current are put to the vacuum region, being separated from the plasma hot core. At this point, the singular surface is also put in the vacuum and after that the vacuum bubbles are formed just the same process as that in free-boundary kink mode (see Fig.4).

We observe the magnetic island saturation with plasma expansion for higher q_{a0} values $2.05 \lesssim q_{a0} \lesssim 2.3$ as shown in Fig.5. The transition from formation of vacuum bubbles to saturation due to magnetic islands occurs about $q_{a0}=2.05$ for the plasma of this current profile with $\kappa_\parallel=10^2$. To see this, we rewrite Eq.(11) by elimination of Ψ by use of Eq.(10) as follows;

$$[\gamma+\kappa_\parallel F^2]\eta = -\frac{m}{r}\frac{d\eta_{eq}}{dr}(\Phi-\kappa_\parallel F\Psi) \quad . \tag{15}$$

Sign of resistivity perturbation at the plasma surface, $\eta(a)$, determines whether vacuum bubbles are formed or not, so the condition for the formation of vacuum bubbles can be written by the following condition for $\kappa_\parallel$;

$$\kappa_\parallel < \frac{\Phi}{\Psi}\frac{q}{m-nq}\Big|_{r=a} \quad . \tag{16}$$

In the case of $\kappa_\parallel=0$, since $m-nq < 0$ and $\Psi > 0$ at plasma surface r=a, this condition becomes to be $\Phi < 0$, just the same as the condition of surface tearing mode [10,12]. So, in this case, the plasma always forms the vacuum bubbles by the surface tearing mode, which is consistent to our former results [10]. In the case of $\kappa_\parallel \to \infty$, this condition cannot be satisfied and in this case plasma always saturate to form the magnetic islands. When q_{a0} value becomes much larger, and the unstabel mode changes from surface tearing mode to tearing mode, the usual magnetic islands saturation with fixed plasma surface position is realized in the simulation (see Fig.6).

4.b Case with limiter

In this subsection, the effect of the limiter on the nonlinear evolution of free-boundary kink mode and surface tearing mode is studied. We assume, for simplicity, that the plasma is surrounded by the limiter for all poloidal and toroidal angles. The limiter radius, b_l, is chosen as $b_l/a_0=1.03$ for

all cases. The value of $\kappa_\perp$ in the plasma region is 10^{-8}, while that in the vacuum region is set 10^{-4} for numerical reasons. Other parameters are the same as those for the case without the limiter.

At first, we investigate the effect of limiter to the case of m/n=2/1 free boundary kink mode; $1.75 \lesssim q_{a0} < 2.0$. We show the time evolutions of q_a and the internal inductance, l_i, for the cases with (solid line) and without (broken line) the limiter in Fig.7 for q_{a0}=1.85 (a) and q_{a0}=1.95 (b), where $l_i = \int_S (\vec{\nabla}\Psi)^2 dS \,/\, (\vec{\nabla}\Psi)_a^2 S$ (S is the plasma area and a denotes the plasma surface) and its initial value is 1. The bold line, shown upper side of the figure, denotes the time duration when the plasma contacts with limiter. In the shrinkage phase with the constant total current, the values of q_0 is unchanged in contrast with the decrease of q_a value, the positive skin current flows near the plasma surface, and the value of l_i becomes small. In the case of q_{a0}=1.85, the final value of q_a is about 1.3 and that of l_i is about 0.7, respectively, for both cases with and without the limiter. After the plasma surface touches the limiter (t>55) the plasma is shrinking as the ellipticity is increasing. In contrast to this case, the time evolutions of q_a and l_i for q_{a0}=1.95 are quite different between two cases with and without limiter. Figure 8 shows the time evolutions of Ψ and η contours for the case of q_{a0}=1.95, in the region of formation of vacuum bubbles. The deformation of plasma is much restricted by the limiter shown by a row of small rectangles in the figure. After the plasma touches the limiter ($t \gtrsim 40$), it is hardly sharpened by the limiter, shrinks rapidly and finally goes into the stable state to m/n=2/1 free boundary kink mode. When the plasma becomes stable against the m/n 2/1 kink mode, the plasma is detatched from the limiter and and the damping oscillation begins ($t \gtrsim 80$), which is clearly seen by the magnetic energy evolution of each mode shown in Fig.9. Since the separatrix always crosses the limiter, the vacuum bubbles cannot be formed and plasma periphery is cooled as the same as the case of $q_{a0} \lesssim 1.9$. As shown by solid lines in Fig.7(b), the minimum value of q_a becomes to be less than one and the value of l_i becomes about 0.6 in this case. To demonstrate the plasma shrinkage and the fluttening of average current density, the radial current profiles of m/n 0/0 mode before (t=0) and after (t=187.5) the shrinkage are shown in Fig.10. This phenomenon is much different from that without the limiter; the formation of large vacuum bubbles. The evolutions of q_a and l_i of that case are shown by broken lines in Fig.7(b) and the evolution of Ψ and η are shown in Fig.2, respectively.

Next, we investigate the limiter effect in the case of surface tearing mode, $2. \lesssim q_{a0} \lesssim 2.45$. In Figs. 11 and 12, time evolutions of Ψ and η contours are shown for q_{a0}=2.05 and q_{a0}=2.15, respectively. In both cases, when the singular surface is put into the vacuum region, the magnetic islands with ths plasma current are also put there. This helical current flowing in the magnetic islands, which is separated from the hot plasma core, makes the plasma in the equilibrium state stable to m/n=2/1 kink mode and the plasma is detached from the limter once ($t \gtrsim 130$ in Fig.11 and $t \gtrsim 230$ in Fig.12). The helical current, however, disappears due to the interaction with the limiter and the plasma becomes unstable to m/n=2/1 kink mode again, and the same process develops as that in the free-boundary kink mode. The values of q_a become nearly equal to 1 in both cases.

Figure 13 is the stability diagram in the $(q_a, q_0/q_a)$ plane for approximated current profile to that realized in the nonlinear calculations with the limiter, where the hatched region denotes the unstable one. The trajectories of q_0=const. for q_{a0}=1.85 and q_{a0}=1.95 are also depicted, which correspond to the results of nonlinear calculations. In this stability calculation, the plasma radius is determined from the condition of constant total current, that is, $a = a_0\sqrt{q_a/q_{a0}}$ with a_0/b=0.66. It is easily seen from the figure that higher q_{a0} values for the same q_0/q_a value reslut in lower q_a value in the final stable state. Final q_a values of nonlinear calculations for both q_{a0} cases are shown in the figure by open circles. Because of its inertial effect, the final q_a values decrease lower than the

marginaly stable values. It should be noted, however, that the numerical results here are obtained from the single helicity calculation and in an actual plasma with q_a less than unity, the most dangerous m/n 1/1 free boundary kink mode becomes unstable, which can easily lead the current disruption. The existence of this m/n 1/1 free boundary kink mode in a tokamak is already detected in T-10 experiment,and the relation to major disruption is also suggested in Ref.[16]. To show the whole disruption process, multiple helicity calculation must be carried out.

It is also easily seen from Fig.13 that, if the plasma can pass the dangerous zone, q_a of about 2, without large deformation of plasma surface in some way, the m/n=2/1 free-boundary kink mode becomes not so dangerous and the shrinkage due to the instability makes the value of q_a a littiel bit smaller; just the intermediate one, $1.3 \lesssim q_a \lesssim 1.7$, where the plasma is stable to both m/n=2/1 kink mode and m/n=1/1 surface tearing and kink modes. This can explain the reason of realizing the very low q_a value in a few tokamak experiments, once q_a is lowered blow 2 [17].

4.c Negative surface current

In this subsection, the evolution of negative surface current, which is considered to play an important role in the major disruption process, is studied. Figure 14 shows the time evolution of the maximum value of negative surface current near top or bottom of plasma poloidal plane in Fig.8 for q_{a0}=1.95 without limiter(broken line) and with limiter(solid line). The negative surface current developed to suppress the instability does not disappear in spite of the interaction between the plasma and limiter, but even grows rapidly during the contact and disappears suddenly when the plasma reaches the stable state and is detached from the limiter. This fact is different from the prediction of Kadomtsev[6] or Zakharov[7], but it is plausible because the plasma surface is always formed just inside of limiter, the plasma is unstable during the interaction and, furthermore, the negative surface current grows almost exponentially.

5. SUMMARY AND DISCUSSION

In this section, we summarize the results of nonlinear calculations. The parallel diffusion of resistivity plays a crucial role in the evolution of free-boundary modes, especially in the case with the limiter; The plasma shrinks due to the diffusion, while the plasma area and the value of q_a is conserved in time without the diffusion. The final states of nonlinear m/n=2/1 free-boundary modes evolutions without the limiter are classified into following four cases according to the value of initial q_a, q_{a0}.

1. Saturation of magnetic islands without plasma surface deformation
2. Saturation of magnetic islands with plasma expansion
3. Saturation due to formation of vacuum bubbles
4. Stable state of shrunk plasma

The ranges of q_{a0} are $4 \gtrsim q_{a0} \gtrsim 2.3$, $2.3 \gtrsim q_{a0} \gtrsim 2.05$, $2.05 \gtrsim q_{a0} \gtrsim 1.9$ and $1.9 \gtrsim q_{a0} \gtrsim 1.75$ for cases 1, 2, 3 and 4, respectively, which are values for calculation parameters in this report, and depend on the current profile and/or the value of κ_s. The boundary between cases 1 and 2 almost coincide with that between tearing and surface tearing modes, and that of cases 2 and 3 is given by Eq.(16). As for the boundary between cases 3 and 4, however, the mechanism is not clarified yet, and we can determine this boundary only by the nonlinear calculations at present.

When the plasma is surrounded by the limiter placed near the plasma surface, the above-mentioned final states of cases 2 and 3 becomes completely different one, that of case 4, and in this case, all unstable free-boundary modes with plasma surface deformation go into stable state of shrunk plasma to m/n=2/1 kink mode . In some cases, however, the minimum value of q_a

becomes even less than 1, where the most dangerous m/n 1/1 free boundary kink mode is unstable. New disruption scenario of tokamak discharges with $q_a \cong 2$ is described briefly in the following;

1. When $q_a \cong 2$, m/n=2/1 free-boudary kink mode becomes unstable.
2. Plasma shrinks due to the interaction with the limiter.
3. If $q_0 \cong 1$, this shrinkage makes q_a value to be less than or nearly equal to 1.
4. Then m/n=1/1 free-boundary kink mode becomes unstable, which causes the major disruption.

This process occurs in the neighborhood of the broken line in the stability diagram shown in Fig.13. It can be concluded that the condition, $q_0<1$, is required to pass the dangerous zone of $q_a \cong 2$ in tokamak discharges, because, by the interaction with the limiter, q_a decreases nearly equal to 1 for $q_0 \cong 1$ and the m/n=1/1 kink mode is destabilized. The condition of $q_0<1$ for realization of low q_a ($q_a \lesssim 1.5$) discharges is the same as that in Ref.[7], but the mechanisms are completely different each other. The nonlinear calculations of multiple helicity are now being carried out and the complete results of this disruption scenario will be presented elsewhere.

REFERENCES

[1] TOI, K., ITOH, S., KADOTA, K., KAWAHATA, K., NODA, N., SAKURAI, K., SATO, K., TANAHASHI, S., YASUE, S., Nucl. Fusion 19 (1979) 1643.
[2] NAGAMI, M., YOSHIDA, H., SHINYA, K., JAHNS, G.L., YOKOMIZO, H., SHIMADA, M., IOKI, K., IZUMI, S., KITSUNEZAKI, A., Nucl. Fusion 22 (1982) 409.
[3] WADDELL, B.V., CARRERAS, B., HICKS, H.R., HOLMES, J.A., LEE, D.K., Phys. Rev. Lett. 41 (1978) 1368; WADDELL, B.V., CARRERAS, B., HICKS, H.R., HOLMES, J.A., Phys. Fluids 22 (1979) 896.
[4] SYKES, A., WESSON, J.A., Phys. Rev. Lett. 44 (1980) 1215.
[5] BONDESON, A., Nucl. Fusion 26 (1986) 929.
[6] KADOMTSEV, B.B., POGUTSE, O.P., Sov. Phys. JETP 38 (1974) 283.
[7] ZAKHAROV, L.E., Sov. Phys. JETP Lett. 31 (1981) 714.
[8] KURITA, G., TAKIZUKA, T., AZUMI, M., TAKEDA, T., to be published in Nucl. Fusion.
[9] KURITA, G., TAKIZUKA, T., AZUMI, M., TAKEDA, T., in Proceedings of International Conference on Plasma Physics, 1987, Vol.3, 90.
[10] KURITA, G., AZUMI, M., TAKIZUKA, T., TUDA, T., TSUNEMATSU, T., TANAKA, Y., TAKEDA, T., Nucl. Fusion 26 (1986) 449.
[11] DNESTROVSKII, Yu.N., KOSTOMAROV, D.P., POPOV, A.M., SHAGIROV, E.A., Sov. J. Plasma Phys. 11 (1985) 616.
[12] TAKIZUKA, T., KURITA, G., AZUMI, M., TAKEDA, T., Surface Tearing Modes in Tokamaks, JAERI-M 85-156 (Oct. 1985).
[13] BISKAMP, D., WELTER, H., in Proceedings of Plasma Physics and Controlled Nuclear Fusion Research (International Atomic Energy Agency, Vienna, 1977), Vol.1, 579.
[14] CARRERAS, B., HICKS, H.R., HOLMES, J.A., WADDELL, B.V., Phys. Fluids 23 (1980) 1811.
[15] ROSENBLUTH, M.N., MONTICELLO, D.A., STRAUSS, H.R., WHITE, R.B., Phys. Fluids 19 (1976) 1987.
[16] ALEXANDER, K.F., HINZE, W., LAUX, M., PECH, P., WOLFF, H., CHICHEROV, V.M., Nucl. Fusion 24 (1984) 631.
[17] RUTHERFORD, P., Nucl. Fusion 20 (1980) 1086.

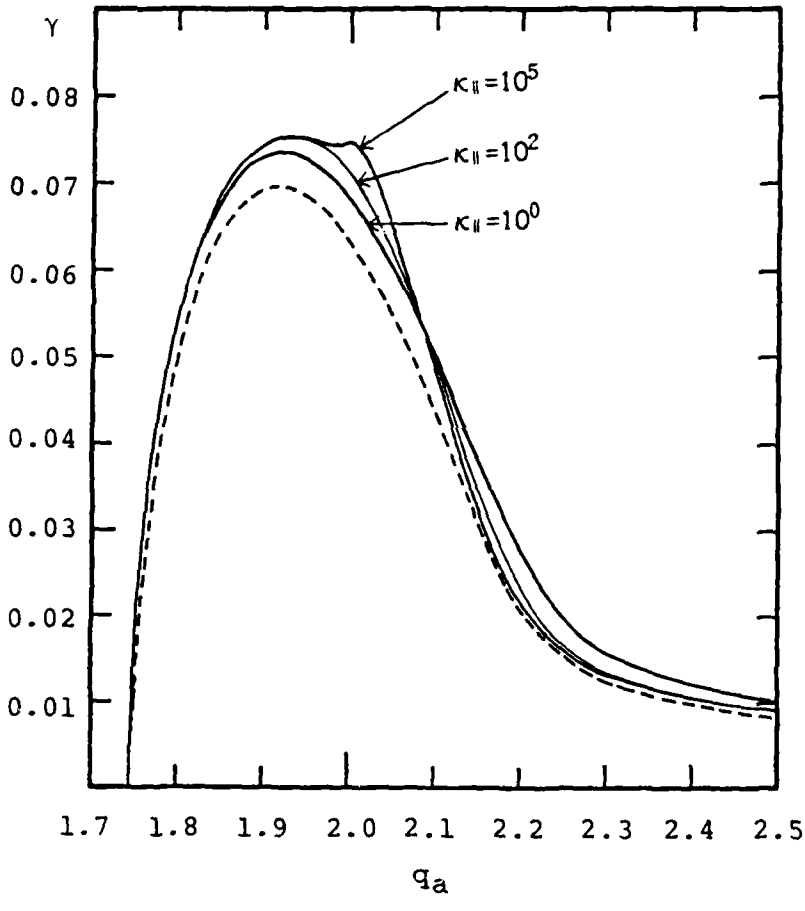

FIG.1 Linear growth rate, γ, versus safety factor at the plasma surface q_a for various values of parallel resistivity diffusion coefficients $\kappa_\parallel$ for current profile; $J(r)=J(0)(1-(r/a)^{3.56})^2$. Parameters are chosen as $a/b=0.66$ and $\eta(b)/\eta(0)=10^6$. Values of $\kappa_\parallel$ are 10^5, 10^2 and 10^0 for three solid lines. Broken line is growth rate without resistivity perturbation, Eq.(11).

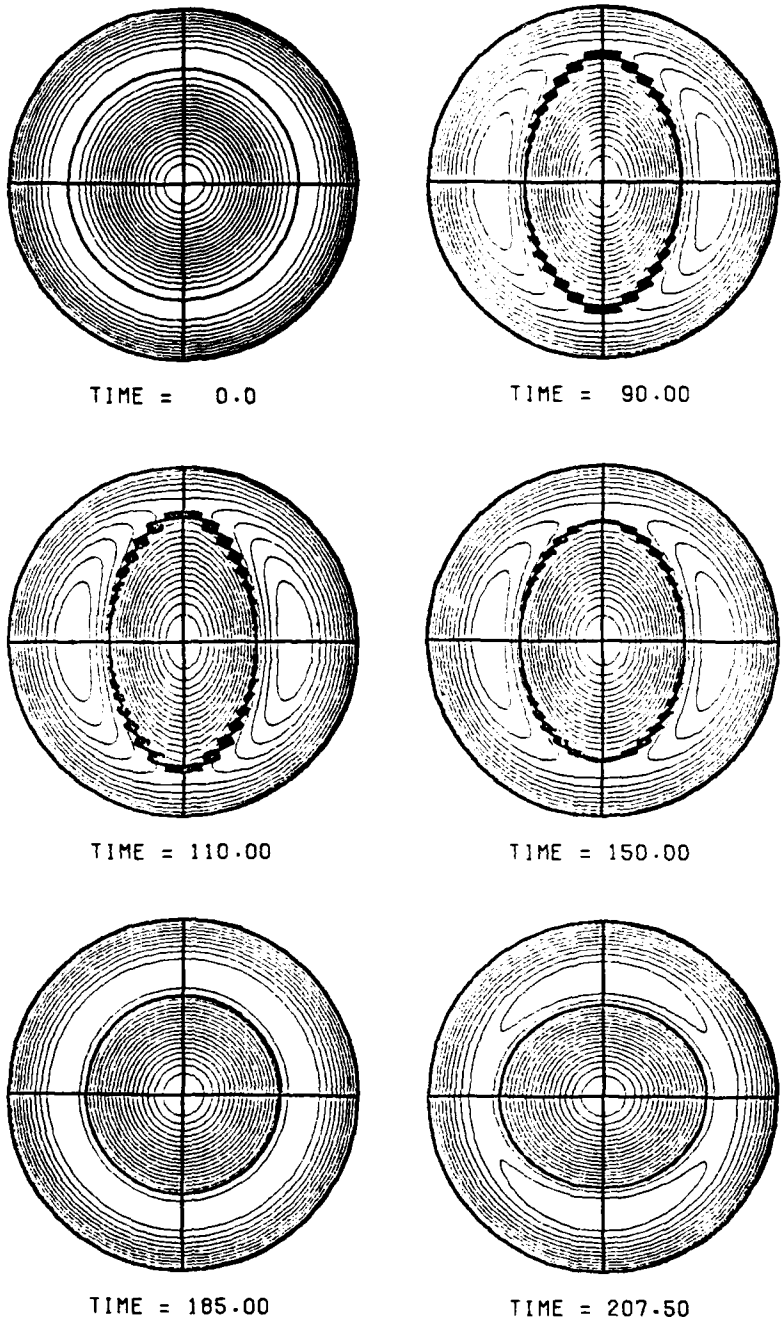

FIG.2 Time evolutions of Ψ contours and plasma surface (bold line) for current profile, $J(r)=J(0)(1-(r/a)^{3.56})^2$, with q_{a0} 1.85. Plasma shrinks with elliptic deformation.

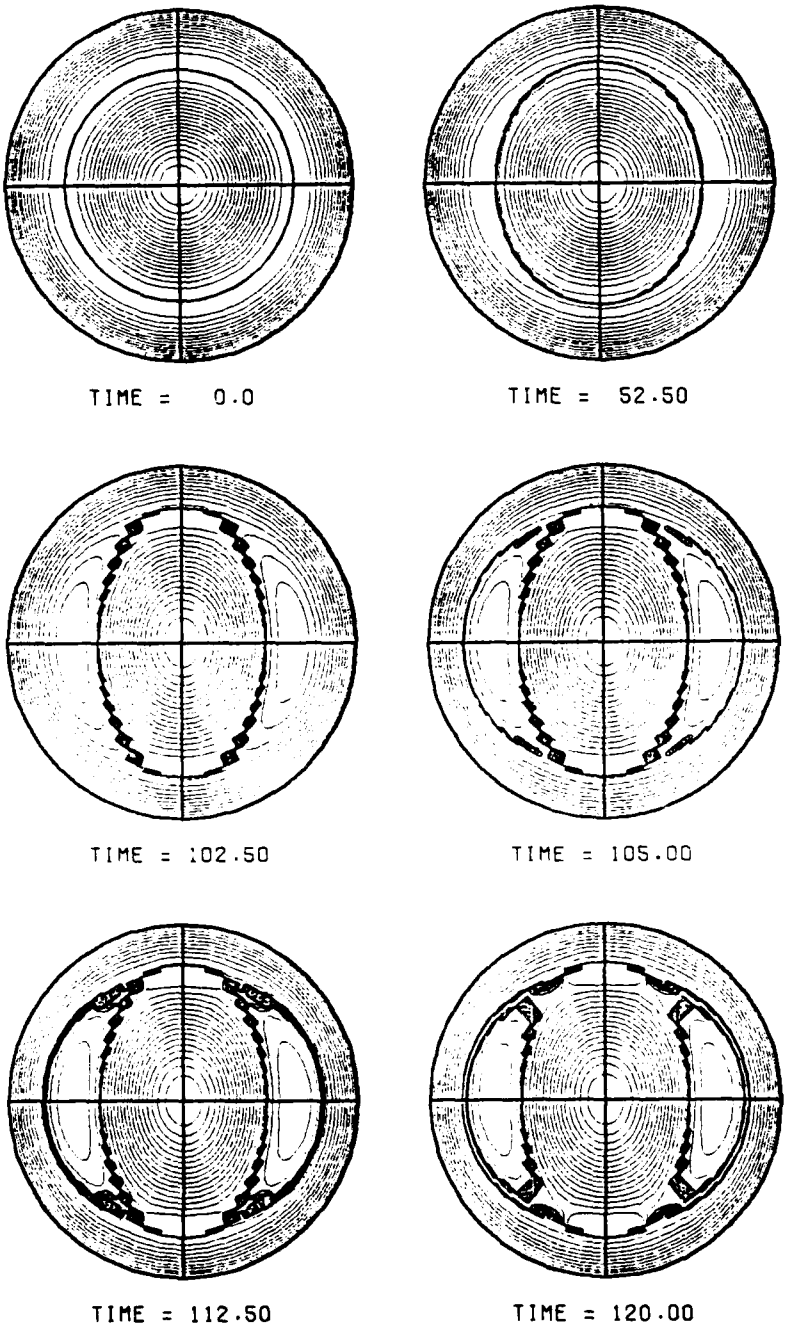

FIG.3 Time evolutions of Ψ-contours and plasma surface for $q_{\alpha 0}$=1.95. Formation of large vacuum bubbles is observed.

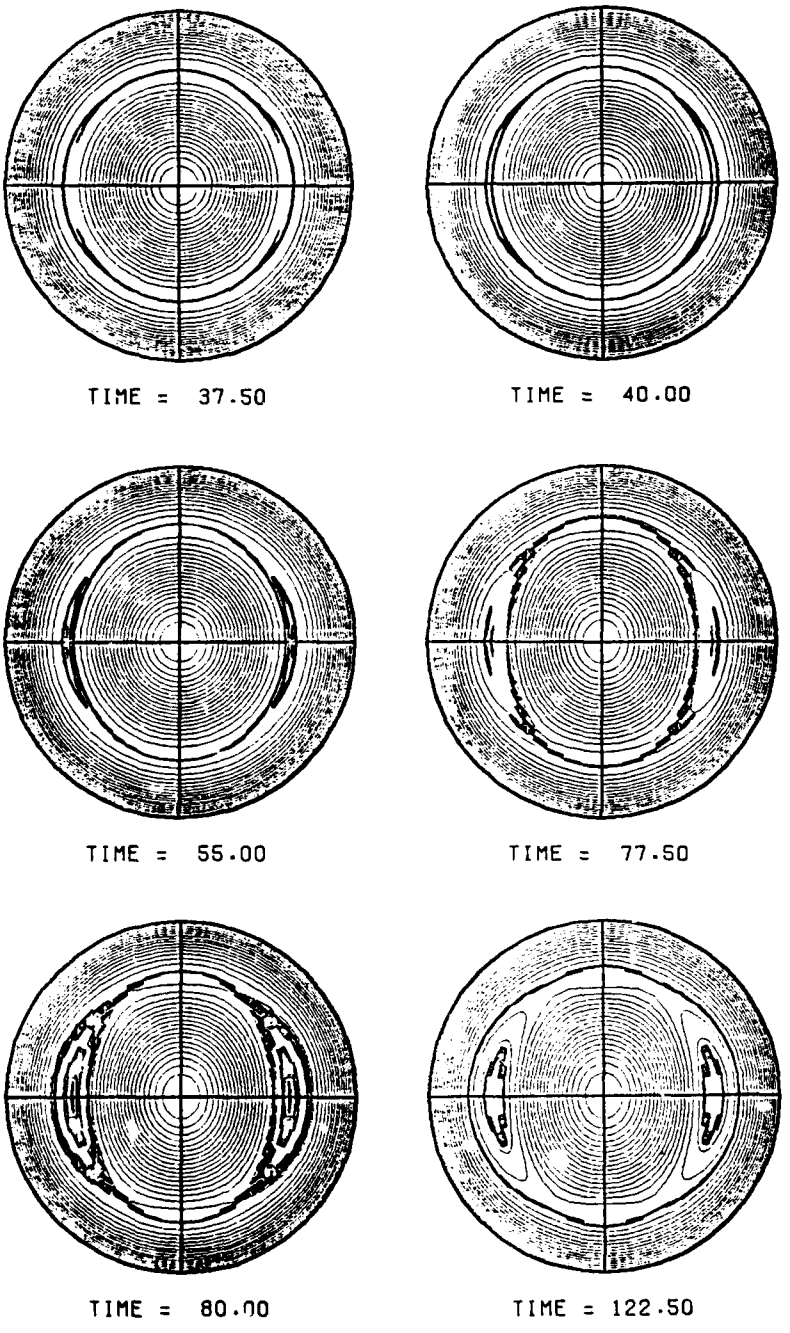

FIG.4 Time evolutions of Ψ-contours and plasma surface for q_{a0}=2.05. Formation of vacuum bubbles is observed for plasma of $q_a \gtrsim 2$ with finite $\kappa_{\parallel}$.

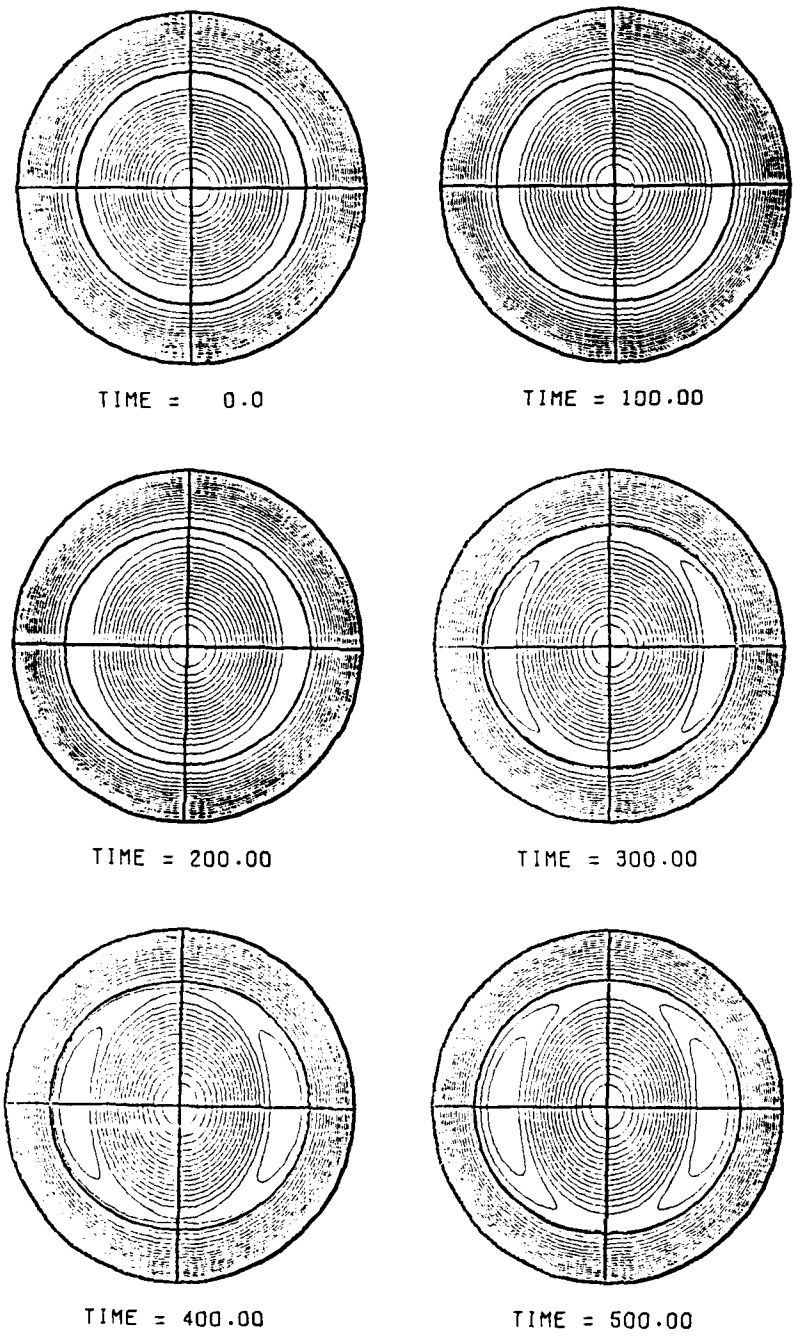

FIG.5 Time evolutions of Ψ-contours and plasma surface for q_{a0}=2.15. Plasma expands due to surface tearing mode with magntic islands.

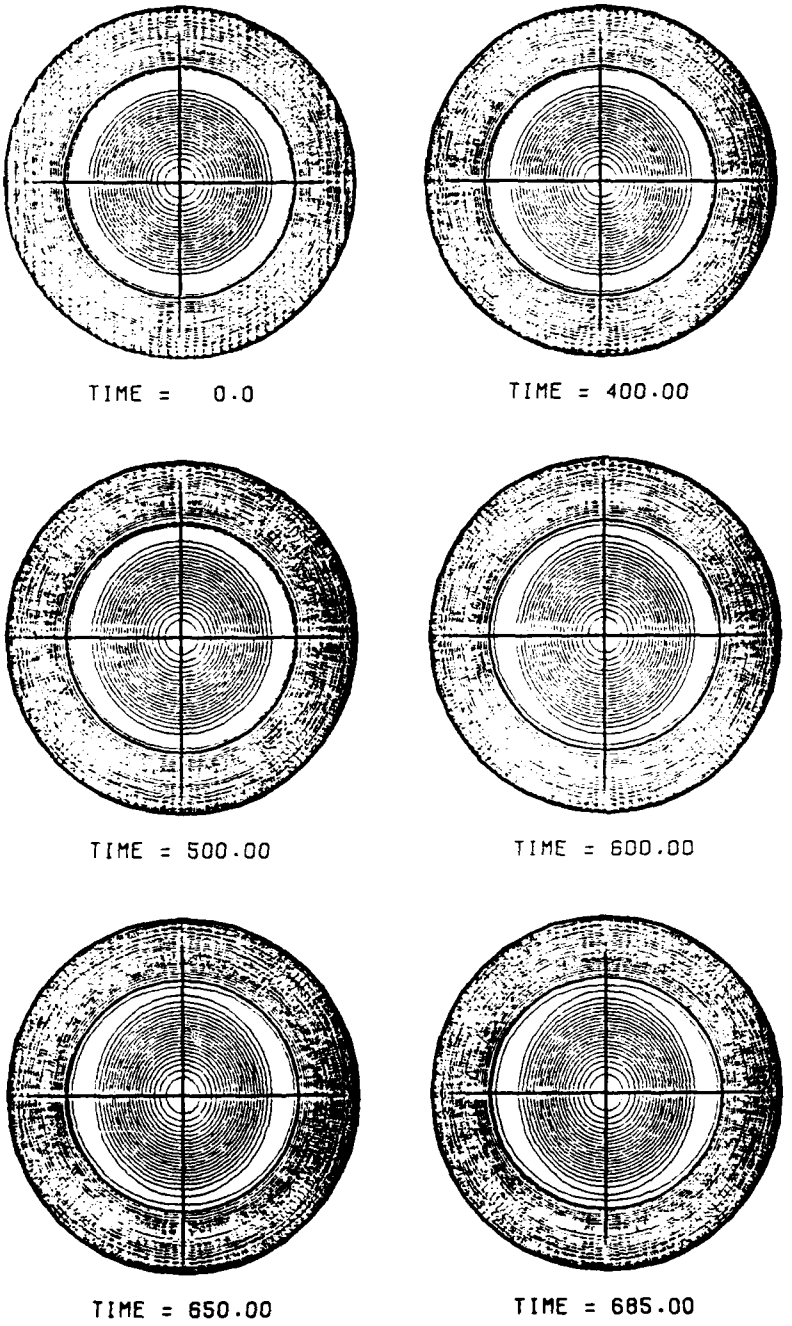

FIG.6 Time evolutions of Ψ-contours and plasma surface for $q_{\alpha 0}$=2.5. For this sufficiently high q_a value, usual tearing mode saturation with fixed plasma surface is observed.

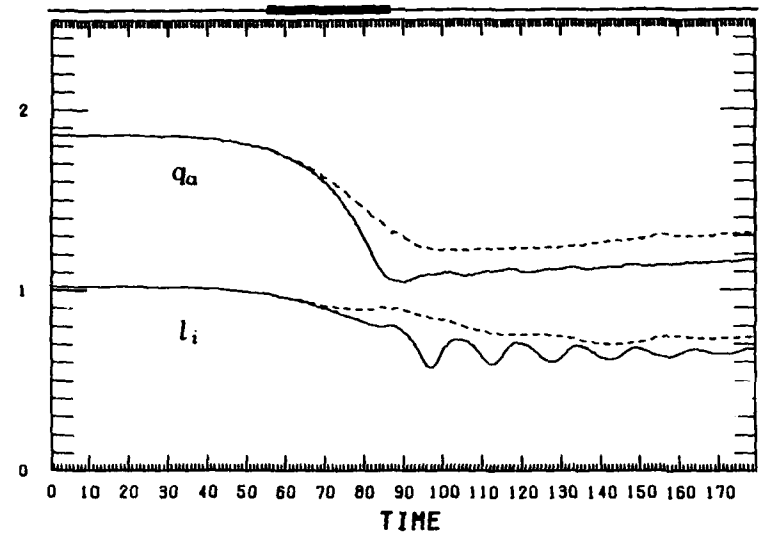

(a)

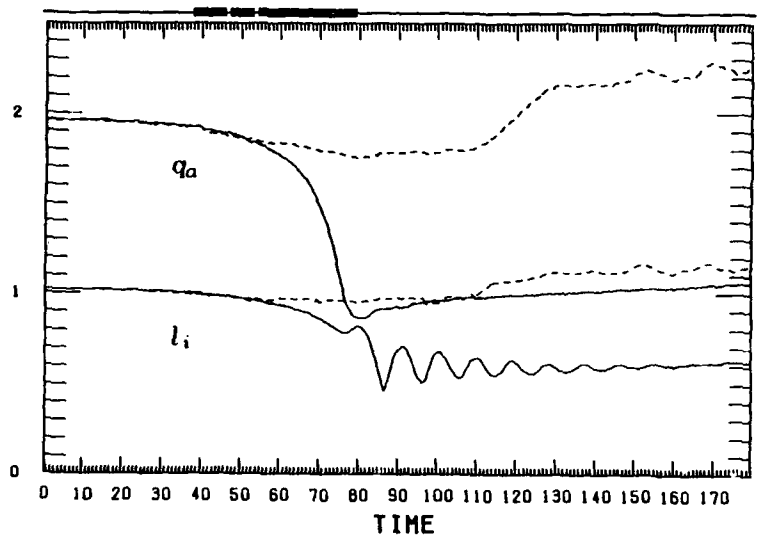

(b)

FIG.7 Time evolutions of q_a and internal inductance l_i for (a) q_{a0}=1.85 and (b) q_{a0}=1.95. Results of calculation with and without limiter are shown by solid and broken curves, respectively. Bold line, shown upper side of figure, denotes the time duration when plasma contacts with limiter.

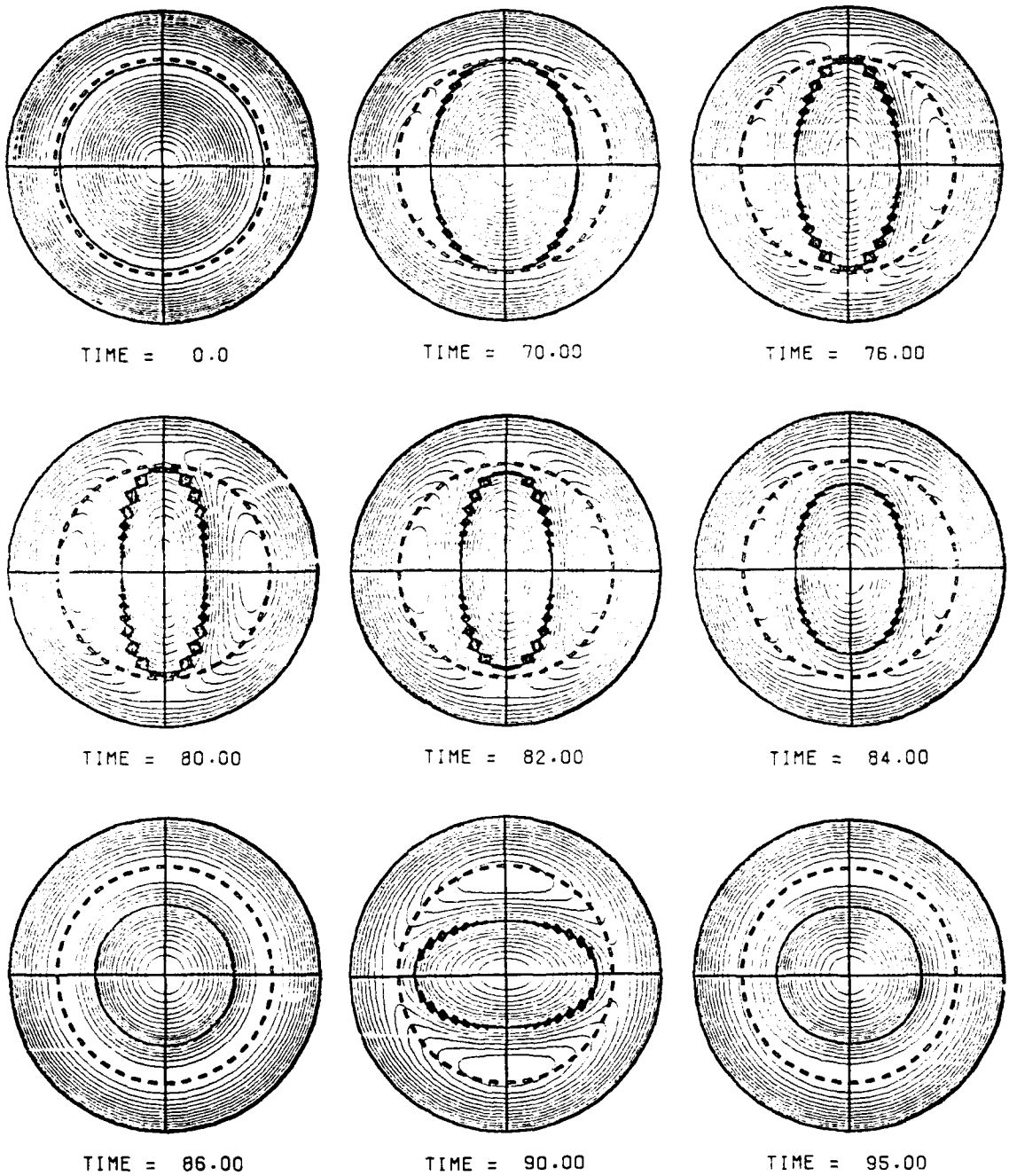

FIG.8 Time evolutions of Ψ-contour and plasma surface for q_{a0}=1.95. Limiter is placed at r=1.03a_0. The plasma touches limiter at t≅38 and is detached from it at t≅79.

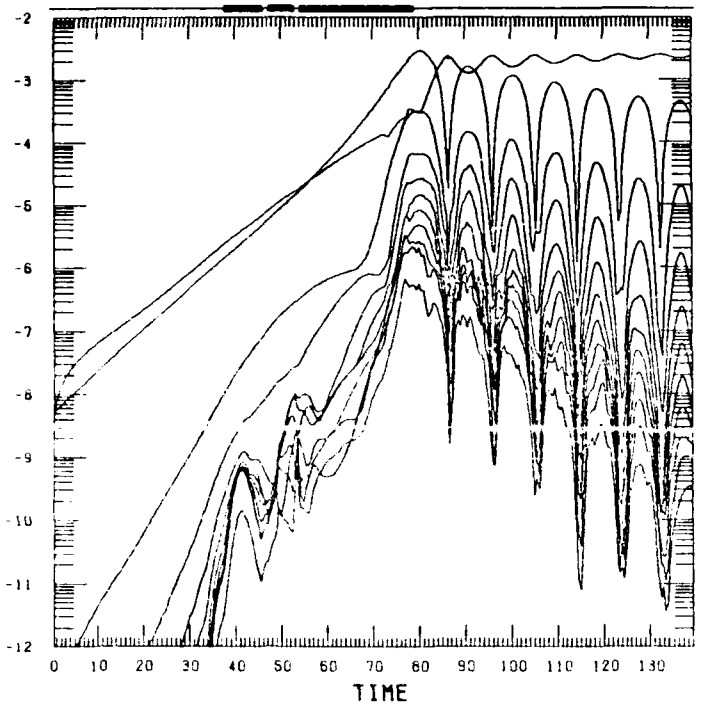

FIG.9 Time evolutions of magnetic energy of each mode for q_{a0} = 1.95 with limiter. Bold lines shown upper side of figure denotes the time duration when the plasma contacts with limiter.

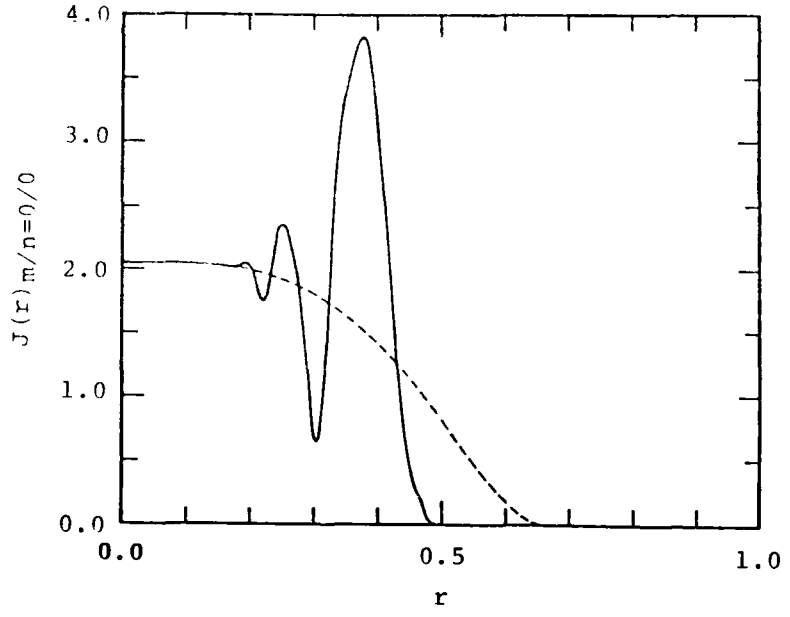

FIG.10 Radial current profiles of m/n=0/0 mode before (t=0; broken line) and after (t=187.5; solid line) plasma shrinkage for q_{a0}=1.95. Plasma radius, a/b=0.66 initially, becomes a/b=0.485 through this shrinkage.

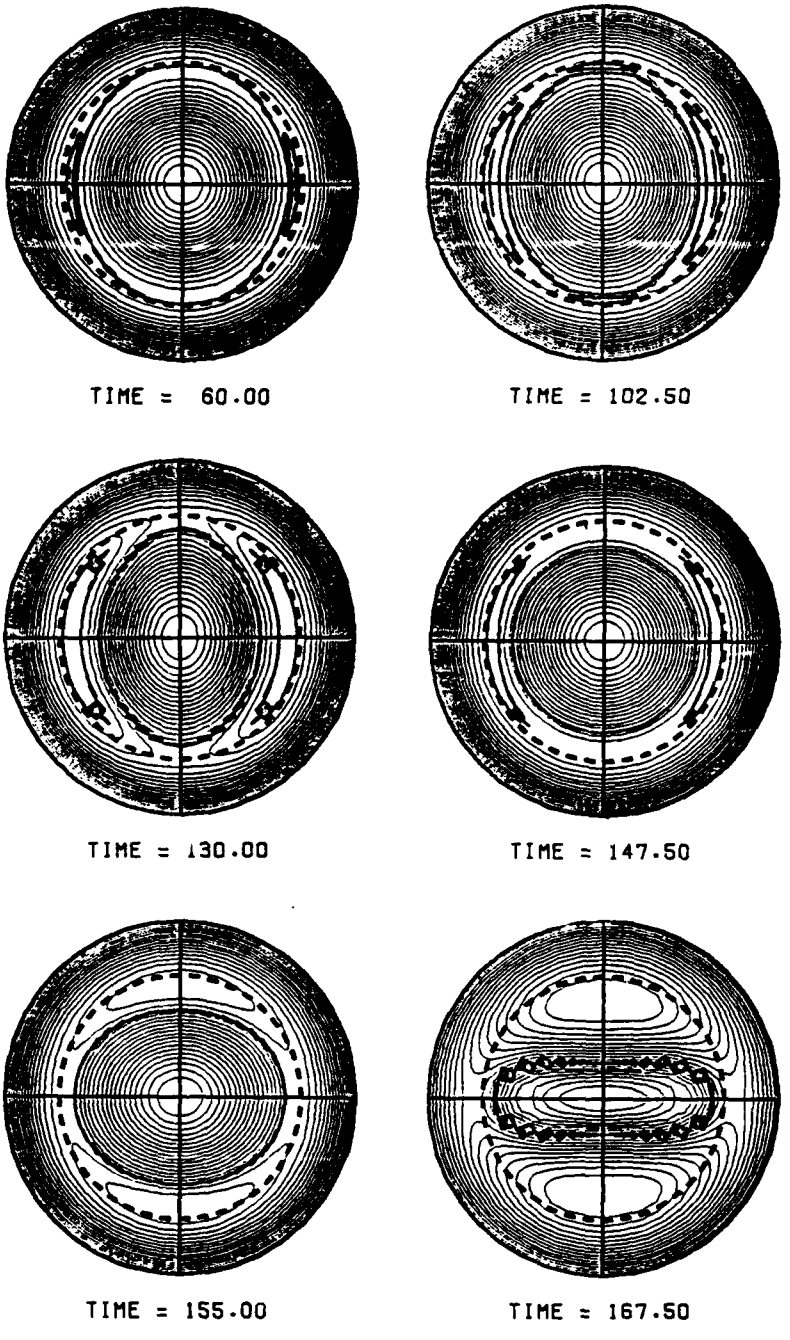

FIG.11 Time evolutions of Ψ-contour and plasma surface for surface tearing mode with q_{a0}=2.05. After helical current disappears due to interaction with limiter, the same phenomenon occurs as that in Fig.8.

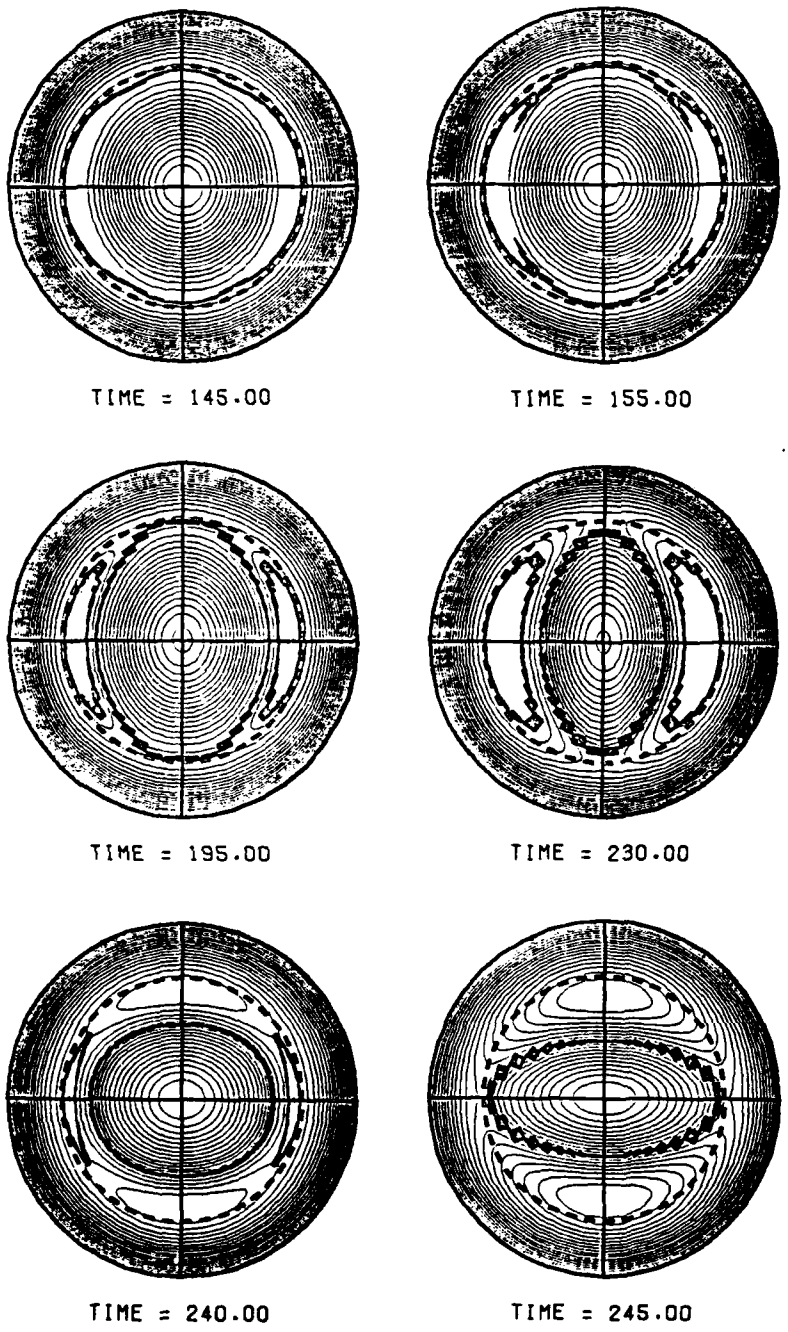

FIG.12 Time evolutions of Ψ-contour and plasma surface for surface tearing mode with q_{a0}=2.15. Almost the same phenomenon occurs as that in Fig.11.

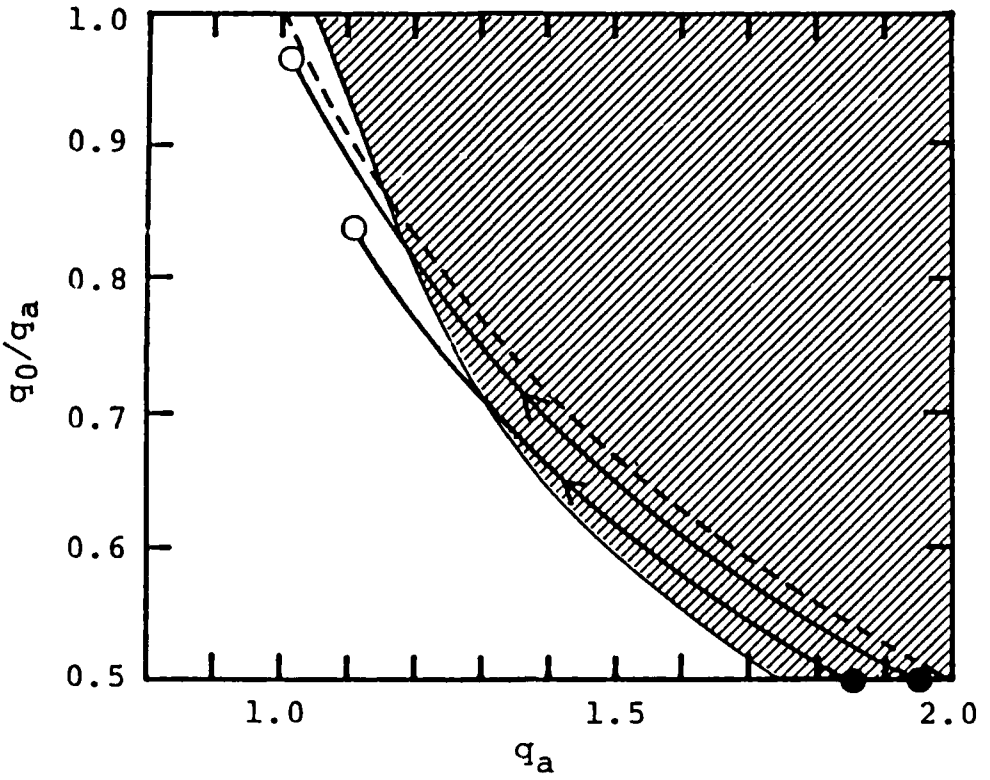

FIG.13 Stability diagram of m/n=2/1 free-boundary kink mode for approximated current density profile to that realized in nonlinear calculations. Hatched region denotes unstable one, and two broken lines of trajectory correspond to nonlinear calculations with limiter for q_{a0}=1.85 and q_{a0}=1.95. Black and open squares denote start and final positions, respectively. Trajectory of q_{a0}=2 (q_0=1) is shown by dotted line. Plasma radius is determined from condition of constant total current, i.e., $a=a_0\sqrt{q_a/q_{a0}}$ with $a_0/b=0.66$.
Current density profiles are determined from following formula,

$$j(r)=j_0\left[(1-(r/a_0)^{3.56})^2+\lambda exp(-2((r-a+\mu)/\nu)^2)\right]\{1-(r/a)^{\upsilon}\}^2.$$

Height of skin current, λ, is determined from condition of constant total current for fixed position of skin current, $\mu=0.1a_0$, and width of that, $\nu=0.05a_0$. Value of υ, which denotes current gradient near plasma surface, is chosen to be several ten.

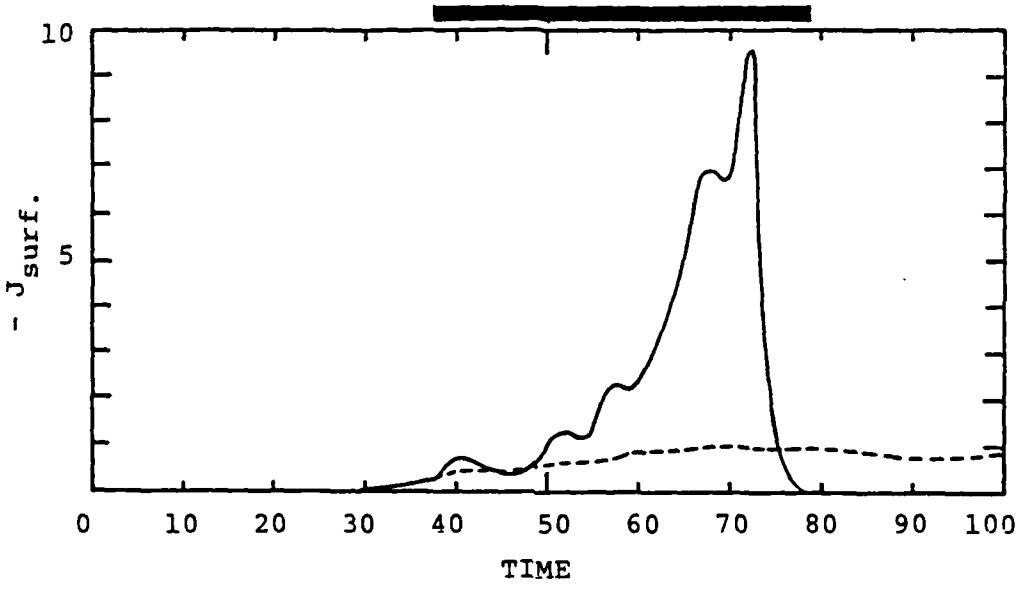

FIG.14 Time evolutions of maximum value of negative surface current near top or bottom of plasma poloidal plane in Fig.8. This is the same calculation as in Fig.7(b). Bold line, shown upper side of figure, denote the time duration when the plasma contacts with limiter. Broken line denotes result without limiter.

A Simulation of Driven Reconnection by a High Precision MHD Code

Kanya Kusano, Yasuo Ouchi, Takaya Hayashi,[*]
Ritoku Horiuchi,[**] Kunihiko Watanabe,[**] and
Tetsuya Sato[*]

Faculty of Science, Hiroshima University, Hiroshima 730, Japan
[*] *Institute for Fusion Theory, Hiroshima University, Hiroshima 730, Japan*
[**] *Science Project Corp., 3-40-17-304 Kuchita-minami, Hiroshima 739-17, Japan*

A high precision MHD code, which has the fourth-order accuracy for both the spatial and time steps, is developed, and is applied to the simulation studies of two dimensional driven reconnection. It is confirm that the numerical dissipation of this new scheme is much less than that of two-step Lax-Wendroff scheme. The effect of the plasma compressibility on the reconnection dynamics is investigated by means of this high precision code.

§1. Introduction

The magnetohydrodynamic (MHD) simulations have given a great contribution to the researches of the nuclear fusion and astrophysical plasmas. The widely used numerical schemes of the MHD simulation codes are categorized to two types of schemes, i.e. Fourier and finite difference schemes. The former is useful for the problems that have a periodic boundary condition, and the latter is favorable for the free boudary problems, the typical example being space plasma phenomena. Two-step Lax-Wendroff scheme[1] is one of the most widely used finite difference schemes. This scheme time-centres the integration by defining temporary or intermediate values of the dependent variables at the half time steps, and this is a explicit method that has the second-order accuracy in the spatial and time steps. Because of the stability and the convenience for the implementation, two-step Lax-Wendroff scheme is much powful for analyzing the global MHD dynamics. In this scheme, however, large numerical diffusion occurs in short wavelength components, and hence this method is not so appropriate for the problem in which short wavelength components are important, for example, turbulence and shock problems.

In this research, we develop a high precision MHD code that has the fourth-order accuracy in both the spatial and time steps, and apply that to the simulation of two dimensional driven reconnections. It is widely known that there are two types of reconnections, one being tearing mode reconnection and the another being driven reconnection. Sato and Hayashi in detail investigated the dynamics of driven reconnection by means of two-step Lax-Wendroff simulation code, and they found that driven reconnection leads to accelaration of plasma as high as the local Alfven speed, and that slow MHD shocks is formed just downstream of the separatrix. They also revealed that once reconnection proceeds, its ultimate fate no longer seems to be dependent on the resistivity, but is largely controlled by the boundary conditions.

The first objective of this paper is to reconfirm the above conclusions by means of high precision code. The second one is to show the effectiveness of the high precision code by quantitatively comparing the simulation results by two different codes. And the another objective is to investigate the influence of the plasma compressibility on the reconnection dynamics by using of the high precision code.

§2. Numerical Scheme and Simulation Model

We employ the fourth-order finite difference approximation to the spatial derivative

$$\left(\frac{\partial f}{\partial x}\right)_j = \left\{8(f_{j+1}-f_{j-1}) - (f_{j+2}-f_{j-2})\right\}/12\Delta x, \quad j = 3, 4, \ldots, N_{x-2}$$

where the simulation region, $x=-L_x/2\sim L_x/2$, is implemented on a set of N_x mesh points x_j; $x_j=-L_x/2+(j-1)\Delta x$, $\Delta x=L_x/(N_x-1)$. For the other spatial dimensions, the same fashion is employed. And the time integral is carried out by means of the fourth-order Runge-Kutta-Gill method. The time integral scheme for eq. $\partial \mathbf{f}/\partial t=\mathbf{F}(\mathbf{f})$ is given as follows,

$$\begin{aligned}
\Delta \mathbf{f}^0 &= \mathbf{F}(\mathbf{f}_n{}^0)\cdot\Delta t \\
\mathbf{f}_*{}^1 &= \mathbf{f}_n{}^0 + c_1\cdot\Delta \mathbf{f}^0 \\
\\
\Delta \mathbf{f}^1 &= \mathbf{F}(\mathbf{f}_*{}^1)\cdot\Delta t \\
\mathbf{f}_*{}^2 &= \mathbf{f}_n{}^1 + c_2\cdot(\Delta \mathbf{f}^1 - \Delta \mathbf{f}^0) \\
\Delta \mathbf{f}_*{}^1 &= Q_2\cdot\Delta \mathbf{f}_n{}^0 + S_2\cdot\Delta \mathbf{f}^1 \\
\\
\Delta \mathbf{f}^2 &= \mathbf{F}(\mathbf{f}_*{}^2)\cdot\Delta t \\
\mathbf{f}_*{}^3 &= \mathbf{f}_n{}^2 + c_3\cdot(\Delta \mathbf{f}^2 - \Delta \mathbf{f}^1)
\end{aligned}$$

$$\Delta \mathbf{f}_*^2 = Q_3 \cdot \Delta \mathbf{f}_n^1 + S_3 \cdot \Delta \mathbf{f}^2$$

$$\Delta \mathbf{f}^3 = \mathbf{F}(\mathbf{f}_*^3) \cdot \Delta t$$

$$\mathbf{f}_{n+1}^0 = \mathbf{f}_n^3 + c_4 \cdot (\Delta \mathbf{f}^3 - 2 \cdot \Delta \mathbf{f}_*^2)$$

where $c_1 = 1/2$, $c_2 = 1 - 1/\sqrt{2}$, $c_3 = 1 + 1/\sqrt{2}$, $c_4 = 1/6$, $Q_2 = 1 - 3c_2$, $Q_3 = 1 - 3c_3$, $S_2 = 2c_2$, $S_3 = 2c_3$, and n denotes the time step.

The boundary condition, the initial condition and the basic equations are just same as Sato and Hayashi's ones.[2] The initial distributions of the magnetic field $B_x(z)$, the current $j(z)$, and the pressure $p(z)$, are chosen to be

$$B_x(z) = B_{x0}\tanh(z), \quad j(z) = j_0 \mathrm{sech}^2(z), \tag{1}$$

$$p(z) = p_0 \mathrm{sech}^2(z) + \mathrm{P}_0, \tag{2}$$

where $p_0 = B_{x0}^2/2$, and P_0 is constant for space. (But P_0 is usually zero, if not indicated differently.) The simulation region is a square box surrounded by four planes, two being parallel to the x axis and placed at $z = \pm 2$ (normalized), and the other two being parallel to the z axis and placed at $x = \pm 3$. We inject the plasmas with a given mass flux, magnetic energy flux, and total energy flux symmetrically from the boundaries placed at $z = \pm 2$ (input boundary). The boundaries at $x = \pm 3$ (output boundary) are assumed to be free boundary. We presume that the resistivity η takes the form

$$\eta(j) = \begin{cases} \alpha(j - j_c)^2 & \text{for } j \geq j_c \\ 0 & \text{otherwise.} \end{cases}$$

And the basic equations to be solved are the compressible, isotropic, one-fluid magnetohydrodynamic equations. The real calculation is carried out by using of the normalized set of these equations as same as in Ref.2.

§3. Results

Figure 1 is the contour plot of the magnetic flux at three different times, where A_0 is the maximum speed of the injected flow from the input boundaries. As same as Fig.1 in Ref.2, the X-type neutral point and the separatrix are formed before t=12 Alfven times. Afterwards, reconnection proceeds and plasma is accelerated as high as local Alfven speed, the slow shock being generated. Figure 2 shows the cross section distributions of j, B_x and p in the results by two-step Lax-Wendroff code and high precision code. All parameters in both calculations by two codes are same. Note that the global structures of these two simulations are almost same. This global agreement strongly supports the correctness of the main result in Ref.2, i.e. the slow shocks are formed just downstream of the separatrix. Furthermore, we can see that the high prcision code more sharply reproduce the shock structure on about $z=0.5$. In the up-stream side of shock front, however, the current distribution by the high pricision code has a wavy structure. These small differences in the local structure between two simulations are caused by the reduction of the numerical diffusion in the high prcision code.

Figures 3, 4, and 5 show the temporal evolutions of the electric field by both two-step Lax-Wendroff and the high precision codes, when α, j_c, and A_0 are changed. No remarkable change between two different calculations confirms Sato and Hayashi's conclusion that the crucial parameter for the electric field on the reconnection point, i.e. for the reconnection rate, is not the resitivity, but the plasma flow on the input boundary, A_0.[2] The interesting difference between two-step Lax-Wendroff code and the high precision code is that the pulsation of the electric field is more clearly observed in the high precision code than in two-step Lax-Wendroff code. The difference clearly appears in the curves of $A_0=0.2$ in Fig.5. This pulsation is caused by the effect of magnetosonic wave, which is bouncing between two input boundaries. The disappearance or tne reduction of magnetoson-

ic wave pulsations in two-step Lax-Wendroff code seems to be caused by large numerical diffusion in two-step Lax-wendroff code. These results show that the numerical diffusion of the high precision code is less than that in two-step Lax-Wendroff code.

Lastly, we investigate the effect of the plasma compressivility on the reconnection dynamics by this high precision code. Though driven reconnection have been studied numerically by many authors, the most of them employed the incompressible approximation.[3-6] Recently, however, it is revealed in the reversed-field pinch study that the rate of driven reconnection is reduced by the effect of the finite β of plasma.[7] The reason is that the converging flow into the X-point can lead to the peaking of the plasma pressure on the X-point by the influence of the adiabatic compression, and the peaked pressure on the X-point acts to suppress the converging flow and to delay the reconnection process. From this results, we can suspect that as the system is approaching to the incompressible system the driven reconnection is being reduced, since the incompressible approximation is corresponding to the large pressure limit or large magnetic field limit. In order to confirm this suspection, we execute some calculations of several P_0 in eq.(2). The results are shown in Fig.6, where the up- and down-side panels show the evolutions of the plasma density and electric field on the reconnection (X-)point, respectively. In this simulation, the plasma resistivity is settled to a constant value ($\eta = 0.01$), and the injected plasma flow is adjusted so that the electric field on the input boundaries is constant ($E_0 = 0.2$). We can see that as P_0 is increasing the change of the density on the reconnection point is reduced. If we remember that the uniform density profile is unchanged everywhere in the incompressible approximation, we can consider that the system is approaching to the incompressible system as P_0 is increasing. And we can see also that the electric field, that is proportional to the reconnection rate, is saturated in lower level for larger P_0. Therefore, we can conclude that the

incompressible effect leads to the reduction of the rate of driven reconnection.

References

1. P.D.Lax, B.Wendroff, Comm. Pure Appl. Math. **13** 217 (1960).
2. T.Sato, T.Hayashi, Phys. Fluids **22** 1189 (1979).
3. D.Biskamp, Phys. Lett. **105A** 124 (1984).
4. D.Biskamp, Phys. Fluids **29** 1520 (1986).
5. L.C.Lee, Z.F.Fu, J. Geophys. Res. **91** 6807 (1986).
6. Z.F.Fu, L.C.Lee, J. Geophys. Res. **91** 13,373 (1986).
7. K.Kusano, J. Phys. Soc. Jpn. **56** 963 (1987).

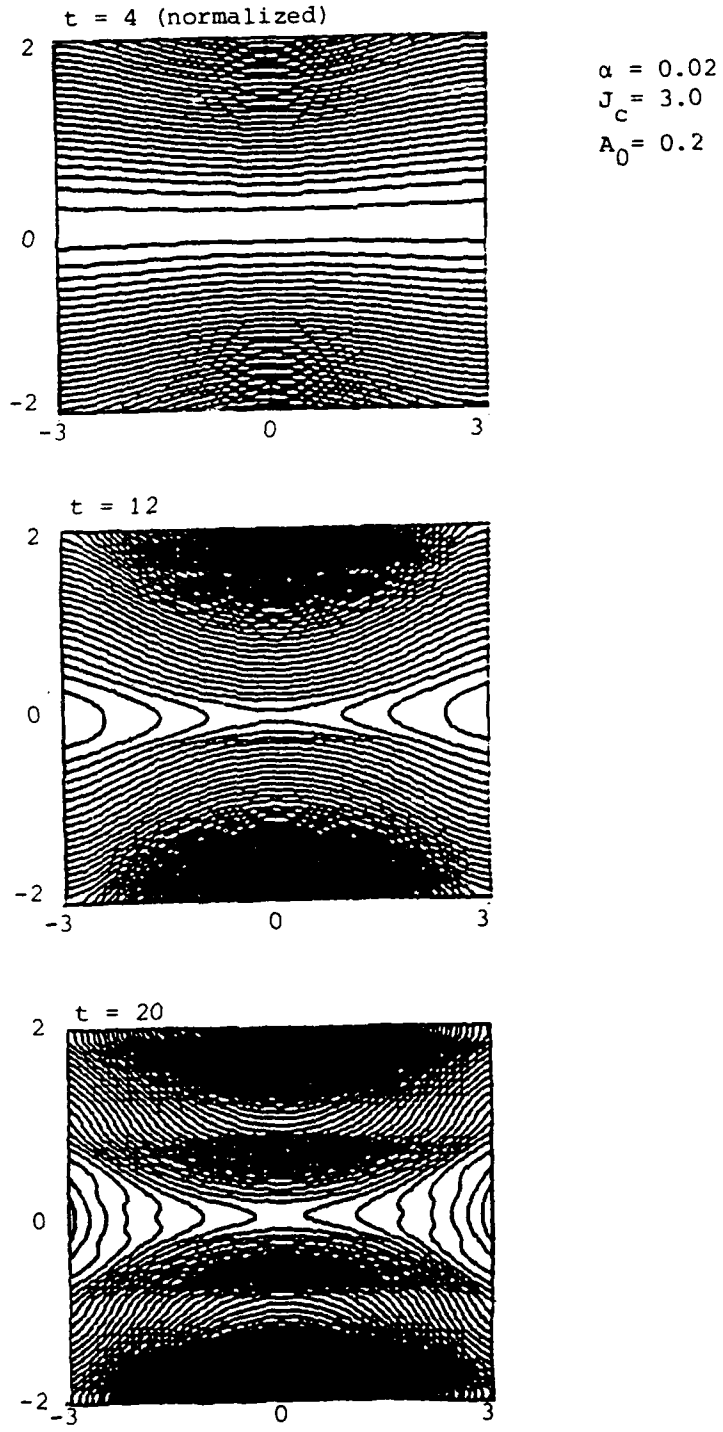

Fig.1. Contour plots of magnetic flux at three different times.

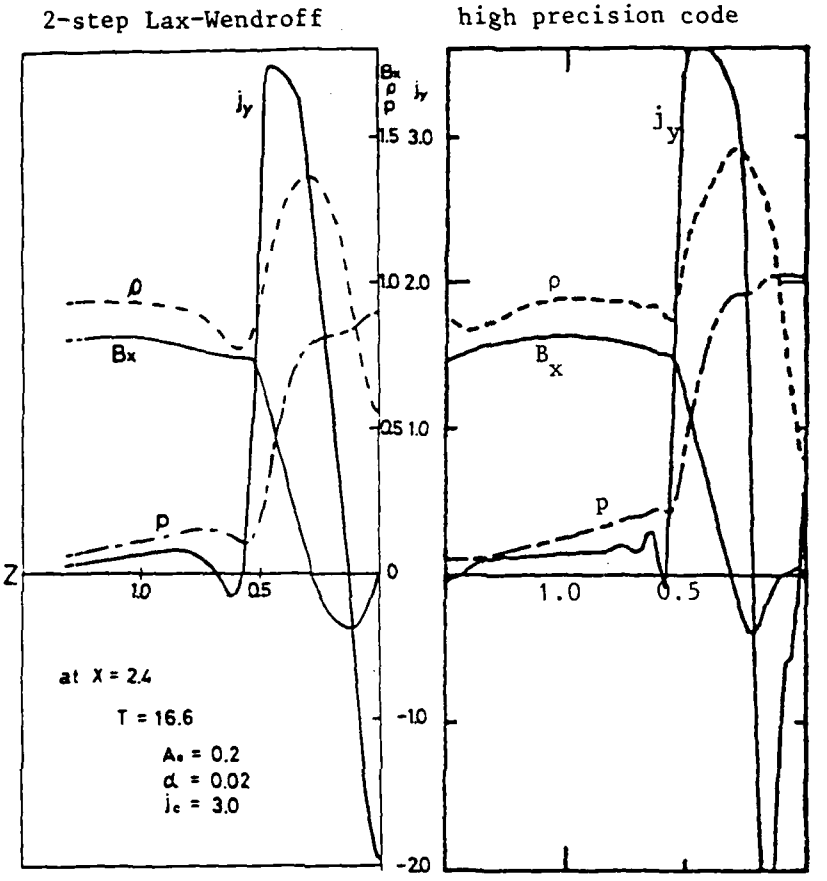

Fig.2. Cross sectional distributions of the current (j_y), x component of the magnetic field (B_x), pressure (p), and density (ρ) on a plane at $x \approx 2.4$. Note the opposite changes of B_x and p (and ρ) across the current layer, thus showing evidence of slow shocks.

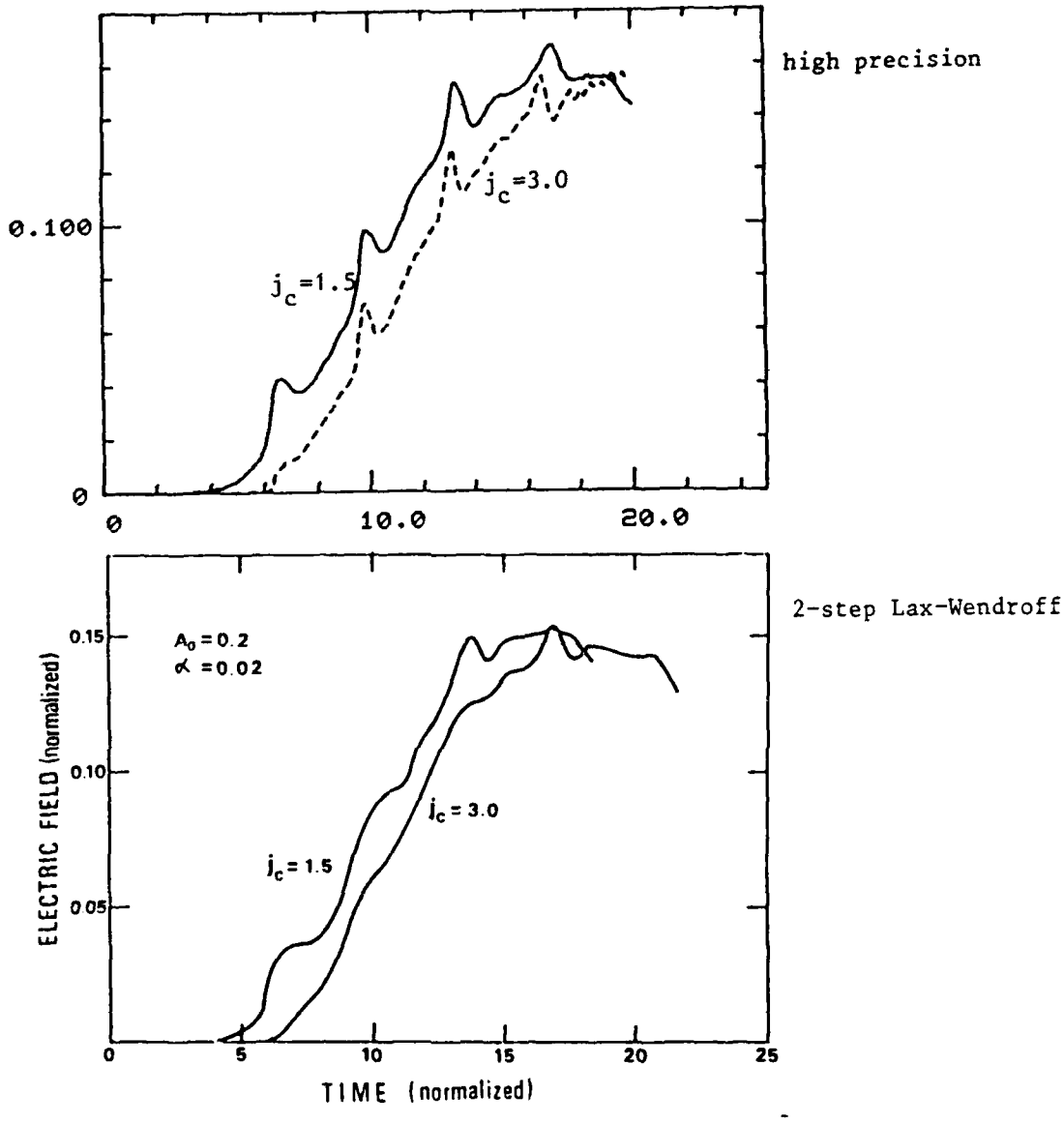

Fig.3. Developments of neutral point electric fields for two different threshold currents j_c. Note that there exists no marked difference.

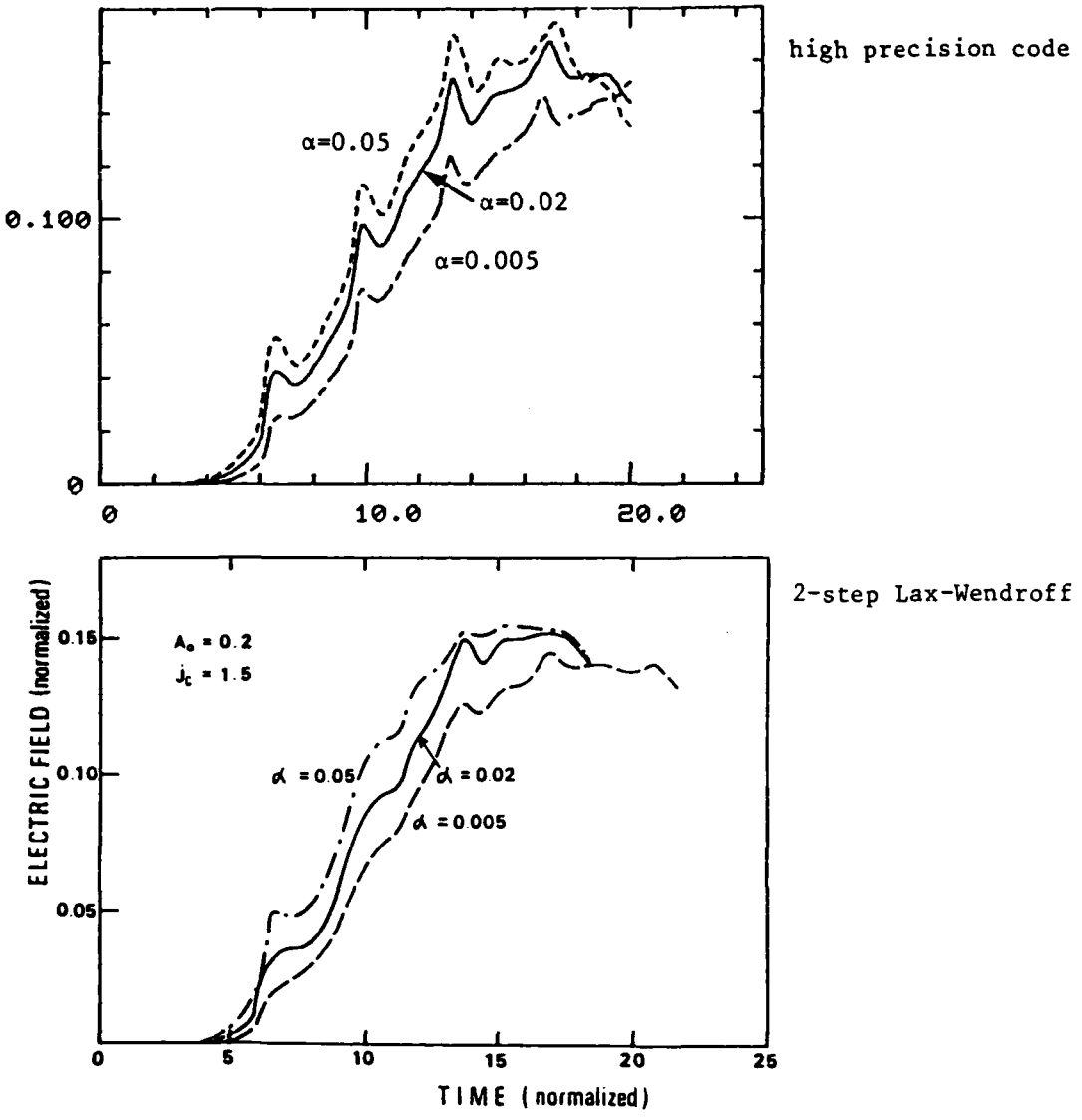

Fig.4. Developments of neutral point electric fields for three different resistivity coefficients α. Note that there exists no marked difference.

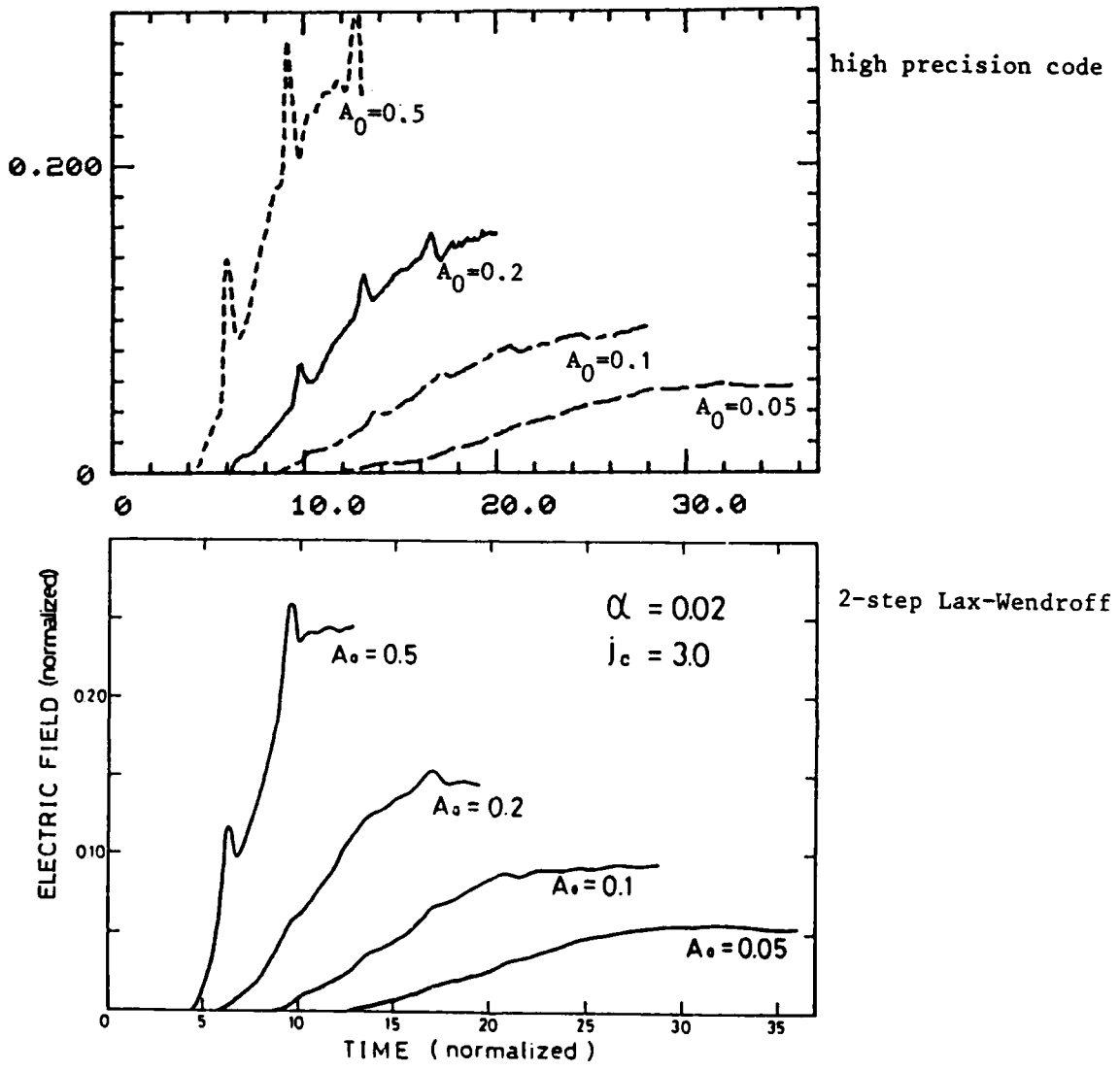

Fig.5. Developments of neutral point electric fields for four different input fluxes A_0. Note a marked dependence on the input flux.

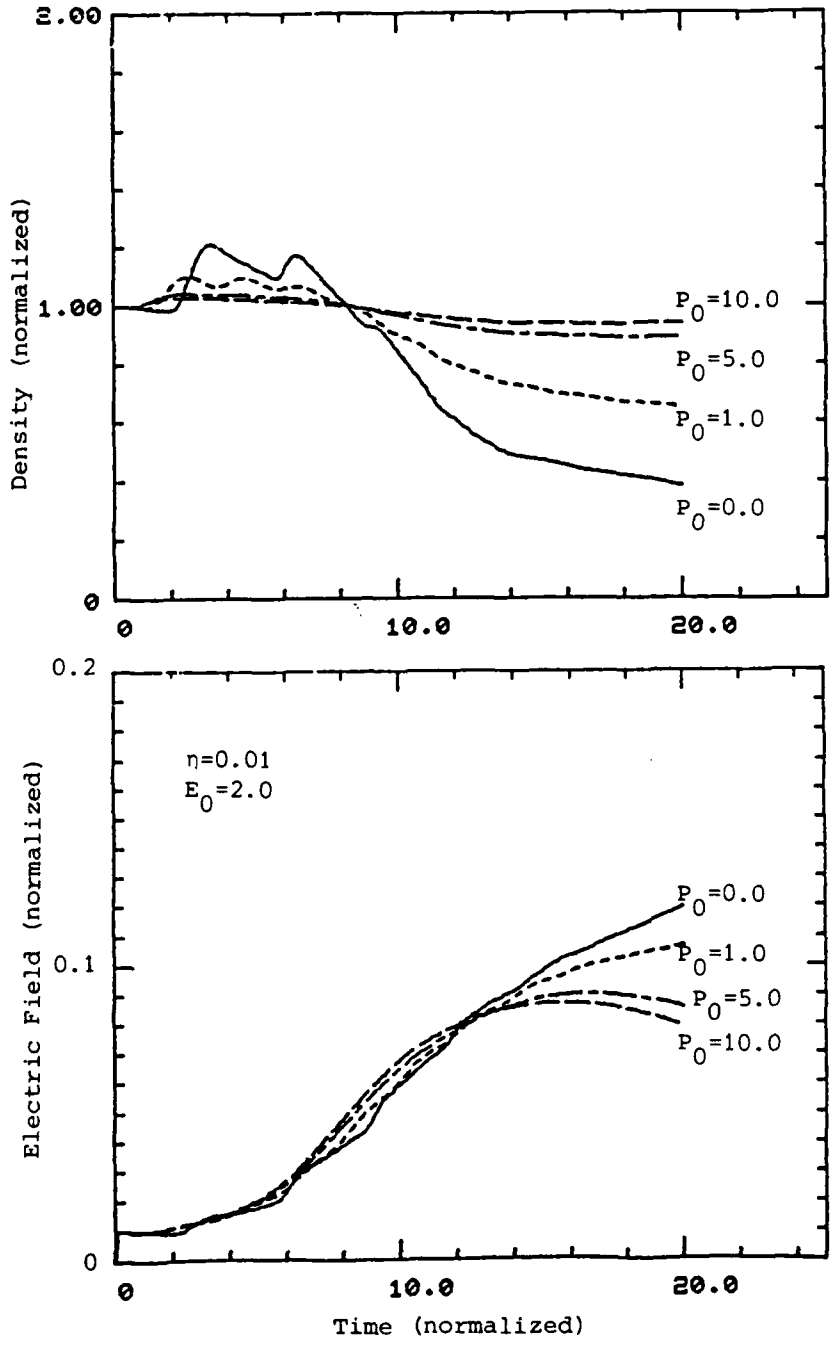

Fig.6. Developments of plasma density and electric field on X-point for four different P_0.

An MHD Simulation of the Solar Wind and Cometary Plasma
(An MHD Model with Plasma Production)

T. Ogino[1], R.J. Walker[2], and M. Ashour-Abdalla[2,3]

[1]The Research Institute of Atmospherics, Nagoya University
Toyokawa, Aichi 442, Japan
[2]Institute of Geophysics and Planetary Physics
University of California Los Angeles, California 90024
[3]Department of Physics
University of California Los Angeles, California 90024

ABSTRACT

Interaction between the solar wind and the plasmas produced from cometary gases has been modeled by using a three-dimensional time-dependent magnetohydrodynamic (MHD) simulation with the cometary mass loading. The model reproduced several features observed by the recent missions to comet Halley. A weak bow shock was located at 3.2×10^5 km in front of the comet. The magnetic field increased by a factor of 3.7 across this weak bow shock and continued to increase up to the contact surface ($B_{max}/B_{IMF}=6\sim8$). The plasma temperature increased across the bow shock and decreased nearer to the comet. IMF lines were hung up on the comet and formed a long plasma tail in which the lobe field was quite strong and $B_{lobe}/B_{IMF}\sim5$. A cold dense plasma sheet formed in the tail and this thin plasma sheet was oriented normal to the IMF direction.

1. Introduction

Interaction between the solar wind and a comet is somewhat different from that between the solar wind and unmagnetized planets like Venus. The difference may occur because the comet has a very small mass or a small gravitational force. Therefore, a large amount of gas is evaporated from the cometary icy nucleus and extends into the solar wind where it is ionized by the photoionization process due to the solar ultra-violet ray and the charge exchange process. Thus a quite broad dayside interaction region, which is composed of three discontinuities, the outer shock, contact surface and inner

shock, can be formed around the comet [Brant and Mendis, 1979; Mendis and Ip, 1977; Mendis and Houpis, 1982; Niedner, 1984]. The cometary plasma tail frequently has a complicated structure with narrow rays, kinks and condensations. Moreover it sometimes shows a mysterious behaviour which is known as a disconnection event [Niedner and Brandt, 1978, 1979; Niedner et al., 1981]. That is, the cometary tail is disconnected and propagates down the tail from the comet.

In the international spacecraft missions to comet Halley, the Suisei probe got to a closest approach of 1.51×10^5km at 13:06 UT on 6 March 1986 [Itoh and Hirao, 1986]. The plasma flow vectors, the proton density and the estimated directions of draped magnetic field in the sun side strong interaction region were demonstrated during the Suisei encounter with comet Halley [Mukai et al., 1986a, b]. The transition corresponding to the bow shock was clearly shown and the shape of the bow shock was given by a parabola. The shock distance from the comet was estimated to be 3.5×10^5km on the sun-comet line at the time of the closest approach of the Suisei probe. The Geotto magnetometer experiment [Neubauer et al., 1986] demonstrated that the magnetic field was strongly enhanced (B=50~60nT) near the comet and suddenly disappears in the cometary center region or probably inside the contact surface. The many features of the strong interaction region have been made clear from the satellite observations. On the other hand, a disturbance of the plasma tail of comet Halley was also observed by handreds of photographs and its dynamics was discussed in connection with the disconnection events of cometary plasma tail [Saito et al., 1986].

Schmidt and Wegmann [1982] solved the full set of MHD equations to model the interaction between the solar wind and the cometary ionosphere in the region exterior to a fixed contact surface by introducing the cometary gas production. Two surfaces of discontinuity, the shock front and the contact surface are reproduced and the embedded magnetic field induces an asymmetry in the plasma flow and in the density distribution of cometary tail. Fedder et. al. [1986 a,b] also simulated the interaction processes to demonstrate the overall structure of the cometary tail. A spheroidal head and a long ribbon-like tail were formed for a steady solar wind and interplanetary magnetic field (IMF). Furthermore, predictions for comet Giacobini-Zinner were presented by the MHD simulation of comets. The interaction of the solar wind with the outflowing plasma from a comet was simulated by using a 2 dimensional MHD model to reproduce the contact surface and the cometary magnetotail [Ogino et al., 1986b]. For a constant IMF, tail magnetic

reconnection begins to occur at several points in a thin plasma sheet. A plasmoid with high plasma density appears in the cometary tail and propagates tailward with a local Alfven speed. When the IMF orientation is reversed, dayside magnetic reconnection occurs at the subsolar point, and a larger disturbance occurs in the whole tail region and propagates down the tail.

In the present paper, the interaction processes between the solar wind and comet Halley have been successively studied by using a 3 dimensional time-dependent MHD model with a cometary plasma production. The model reproduced several features of the comet and solar wind interaction predicted by earlier theories and observed from the recent missions to comet Halley.

2. Simulation Model

The present purpose is to study the interaction between the solar wind and the cometary plasmas by using a 3 dimensional MHD simulation [Ogino, 1986a] with plasma production. Therefore, the plasma production rate is added to the MHD equations as it was given by Schmidt and Wegmann [1982]. The normalized MHD equations are written as follows,

$$\frac{\partial \rho}{\partial t} = -\vec{\nabla} \cdot (\vec{v} \rho) + D \nabla^2 \rho + A \tag{1a}$$

$$\frac{\partial \vec{v}}{\partial t} = -(\vec{v} \cdot \vec{\nabla}) \vec{v} - \frac{1}{\rho} \vec{\nabla} P + \frac{1}{\rho} \vec{J} \times \vec{B} + \frac{1}{\rho} \vec{\phi} - A \frac{(\vec{v} - \vec{v}_c)}{\rho} \tag{1b}$$

$$\frac{\partial p}{\partial t} = -(\vec{v} \cdot \vec{\nabla}) p - \gamma p \vec{\nabla} \cdot \vec{v} + D_p \nabla^2 p + \frac{(\gamma-1)}{2} A |\vec{v} - \vec{v}_c|^2 + \frac{p_c}{\tau_c} \tag{1c}$$

$$\frac{\partial B}{\partial t} = \vec{\nabla} \times (\vec{v} \times \vec{B}) + \eta \nabla^2 \vec{B}, \tag{1d}$$

where,

$$A = \frac{m_c Q_o}{4\pi \lambda_c r^2} e^{-r/\lambda_c}$$

stands for the cometary plasma production, $\vec{J}=\vec{\nabla}\times\vec{B}$ is the current density, ρ the plasma density, v the flow velocity, p the plasma pressure, B the magnetic field, $\phi \equiv \mu \nabla^2 v$ the viscosity, $\gamma=5/3$ the ratio of specific heats, $\eta=\eta_o(T/T_o)^{-3/2}$ the resistivity and T/T_o the normalized temperature. For the sake of convenience the units of distance, velocity and time are respectively defined by the earth's radius ($R_e=6.37\times10^6$m), the Alfven velocity ($v_A=6.80\times10^6$m/s) and the Alfven transit time ($t_s=R_e/v_A=0.937$s). The other numerical parameters are $\eta_o=0.01$, $\mu/\rho_{sw}=D=D_p=0.005$ where ρ_{sw} is the solar wind density, and the small diffusion terms in (1a), (1b) and (1c) are simply added in order to suppress numerical MHD fluctuations. For the present comet

simulation, v_c amd p_c for the cometary plasma are neglected because $|v_c| \ll |v|$ and $p_c \ll p$. The magnetic Raynold's number, which is the magnetic diffusion time devided by the Alfven transit time, S is larger than 400.

The coordinate system used in the 3 dimensional MHD simulation is shown in Figure 1, where $x_o=y_o=z_o=7.7\times10^5$km and $x_1=-1.54\times10^6$km. The solar wind accompanying a uniform IMF in the z-direction flows into the simulation box through the boundary at $x=x_o$ and begins to interact with the cometary plasma. The mirror boundary is used at z=0 and y=0, on the other hand the free boundary, where the spatial derivative of the physical quantities is zero, is used at $z=z_o$, $y=y_o$ and $x=x_1$.

The typical parameters of the solar wind are v_{sw}=500km/s, n_{sw}=15/cc, $T_{sw}=2\times10^5$°K and $B_{IMF}=B_z$=6nT for a closest approach of the Suisei probe to comet Halley [Itoh and Hirao, 1986; Mukai et al., 1986a, b]. Moreover, the parameters of the plasma production for comet Halley are as follows: the plasma production rate, $Q_o=1.0\times10^{30}s^{-1}$, the ionization rate, $\sigma=3.3\times10^{-6}s^{-1}$, the radial flow velocity, v_r=1km/s, the ionization distance, $\lambda_c=v_r/\sigma=3.03\times10^5$km and the effective cometary mass ratio of the water group to the proton, m_c=16 [Mukai et al., 1986a, b]. The MHD equations are solved by the two step Lax-Wendroff method as an initial value problem on the grid points of (N_x, N_y, N_z)=(90, 30, 30) , (150, 50, 50) or (120, 60, 60) except for the boundary. The mesh size is $\Delta x=\Delta y=\Delta z$=4Re, 3Re or 2Re and the time step, Δt is selected as $8\Delta x$ (=30s for $\Delta x=4R_e$) in order to assure the numerical stability.

3. Simulation Results

Interaction processes between the solar wind and comet Halley were simulated by using the observed parameters for the closest approach of the Suisei probe [Mukai et al., 1986a, b] as was previously mentioned. Stating from the initial conditions where a uniform solar wind only exists, the code was run until a quasi-steady state configuration resulted. This required about 1024 time steps or 8.5 hours in real time.

In Figure 2 is shown a quasi-steady state configuration of the interaction between the solar wind and comet Halley in the x-z and x-y planes for no uniform IMF where $B_{IMF}=B_z$=0nT, v_{sw}=500km/s and n_{sw}=15/cc. The plasma density, ρ and the plasma pressure, p are depicted by the contours and the flow velocity by the arrows. A bow shock is formed at 3.2×10^5km as is shown in the plasma pressure and the velocity flow pattern, and a cometary dense

plasma extends toward the downstream. The plasma flow changes its direction toward the outside across the bow shock, however it is rather parallel to the sun-comet line in the further tail. The configuration of interaction is symmetric in the x-z and x-y planes because of no uniform IMF. When a uniform IMF of $B_{IMF}=B_z=6nT$ is introduced in the z direction, the quasi-steady state configuration is modified as is shown in Figure 3. On the top panel the magnetic field is also depicted by the arrows. The position of the bow shock moves little and an asymmetry appears in the x-z and x-y planes. The plasma density and pressure are thinner in the z direction parallel to the uniform IMF, which comes from the draping effect of hanged IMF lines. The megnetic field has a strongly disturbed feature in the neibourhood of the bow shock and is again well ordered in the tail region. The field magnitude is quite large even in the tail lobe (B=30nT). It should be noted that a high density lump appears at $x=-8.8x10^5$km in the tail and propagates tailward. The tailward velocity is about 50km/s which is comparable with a local Alfven velocity, $v_A=40$km/s.

In Figure 4 are shown the profiles of the magnetic field, B, temperature, T, x-component of velocity, v_x and density, ρ on the sun-comet line where M is an effective mass ratio to the proton. The weak bow shock is formed at $x=3.2x10^5$km and the Mach number of the fast magnetosonic wave is about M=2.0 on the sun-comet line, which is quite reduced from the solar wind value, M=6.45. This is because that the plasma temperature increases whereas the velocity decreases in the upstream region of the bow shock due to the cometary plasma production processes. In fact, the simulated temperature, velocity and density are $T/M=1.3x10^{6}$K, v=350km/s and $\rho=Mn=22$/cc in front of the bow shock. The temperature increases across the weak bow shock and then decreases nearer to the comet. The magnetic field increases by a factor of 3.7 across this weak shock and continued to increase up to the contact surface ($B_{max}/B_{IMF}\sim6$). A cold and dense plasma extends toward the tail and the high density lump is seen at $x=-8.8x10^5$km. The magnetic field also exhanced on the comet side of the high density lump at $x=-7.6x10^5$km.

In Figure 5 are shown the profiles of the magnetic field, B, temperature, T, density, ρ, velocity, v and the direction of velocity, θ_v at $x=1.7x10^5$km in the dayside interaction region. The sharp gradients at $z=y=5x10^5$km for T/M, B, v and ρ correspond to the weak bow shock. The velocity somewhat decreases even in the outside of the weak shock from the solar wind value, $v_{sw}=500$km/s due to the plasma production. The flow velocity decreases from 460km/s to 260km/s across the weak shock and

gradually approaches a minimum value of 80km/s on the sun-comet line. The plasma density and the magnetic field increase about 2.7 times across the shock and continue to increase toward the sun-comet line. The flow angle, θ_V deviates about 25° from the sun-comet direction (θ_V=180°) inside the bow shock. These features are very similar to the Suisei probe observation when they are compared with Figure 2 in the article of Mukai et al. (1986a). The plasma temperature increases about 6.8 times across the weak bow shock and decreases toward the sun-comet line. It is noted that the magnetic field strongly fluctuates along the z-direction as well as the y-direction inside the bow shock.

In Figure 6 are shown the profiles of the magnetic field, B, temperature, T, density, ρ and velocity, v at x=-8.1×10^5km in the cometary tail. The magnetic field is enhanced up to about 5 times the IMF value in the tail lobe and is a little enhanced up to 10nT along the y-axis perpendicular to the uniform IMF. The magnetic field does not extremely decreases near the sun-comet line at x=-8.1×10^5km, which means the intrusion of the magnetic field into the cold and dense cometary plasma tail, however it becomes very small in further tail for x<-1.0×10^6km (see Figure 4). The temperature and the velocity decrease at the center of tail and the plasma density increases there. The high plasma density in the tail is thin in the z-direction or in the uniform IMF direction and expands in the y-direction, which is consitent with the draping picture of hanged IMF lines.

In Figure 7 are shown the cross sectional patterns of the plasma pressure, p, density, ρ and the x-component of magnetic field, B_X in the tail for B_Z=6nT and 0nT. Tail lobes and a thin cold plasma sheet are cleary formed by draping effect of IMF lines (see B_X component). The cold plasma sheet is thin in the parallel direction to the uniform IMF, and the tendency becomes remarkable in the distant tail. On the other hand, the plasma sheet is naturally symmetric for no uniform IMF, B_Z=0nT as are shown in the lower two panels.

In Figure 8 are shown the three dimensional configuration of the magnetic field lines and their projection onto the three planes for the interaction between the solar wind and comet Halley, where considerably draped IMF lines are only depicted and the colour means a measure of the field draping. It is clearly seen on the figures that the IMF lines hang up to the cometary plasma as was suggested by Alfven [1957] and slip away toward the tail. The slipped magnetic field lines gradually come close toward the sun-comet meridian (plane at y=0) in the further tail.

4. Conclusion

The interaction between the solar wind and the cometary plasmas has been simulated by using a three dimensional MHD model in order to compare with the recent sattelite observations to comet Halley. As the result, several features of the interaction which are consistent with the Suisei probe and the Giotto observations have been reproduced when the parameters proposed from the satellite observations for the solar wind, the IMF and the plasma production of comet Halley were used.

The simulated position of the weak bow shock, and the spatial variation of the plasma density, velocity and temperature in the sun side interaction region are consistent with those of the observational results from the Suisei probe. The dense and cold cometary plasma sheet extends toward the downstream of the solar wind and becomes thinner down the tail in the parellel direction to the upstream IMF. The magnetic field is enhanced up to about 3 times the IMF value across the weak bow shock and continues to increase up to 6~8 times the IMF value near the comet. The field magnitude of the draped IMF is not small even in the tail lobes and keeps about 5 times the IMF value.

The MHD fluctuations were enhanced in the neibourhood of the weak bow shock. The plasma production, which in turn captures the IMF lines into the cometary interaction region, as well as the Kelvin-Helmholts instability due to the velocity shear must have the responsiblity to the excitation of the MHD waves. A further simulation is needed to study the excitation mechanism of MHD waves in the neibourhood of bow shock and also cometary tail dynamics such as the magnetic reconnection and disconnection events.

Acknowledgements

We would like to acknowledge helpful discussions with Drs. D.A. Mendis, T. Mukai and T. Terasawa. This work was supported by a Grant-in Aid for Science Research from the Ministry of Education, Science and Cultrure and by the NASA Solar Terrestrial Theory Program Grant NAGW-78. The simulations were performed at the Computer Center of Nagoya University.

References

Alfven, H., On the theory of comet tails, Tellus, 9, 92, 1957. Brandt, J.C.,

and D.A. Mendis, The interaction of the solar wind with comets, in Solar System Plasma Physics, Vol. II, edited by C. F. Kennel et al., p. 253, North Holland Publ. Co., Amsterdam, 1979.

Fedder, J.A., S.H. Brecht, and J.G. Lyon, MHD simulation of a comet magnetosphere, Icarus, submitted, 1983.

Fedder, J.A., J.G. Lyon, and J.L. Giuliani, Jr., Numerical simulations of comets: Prediction for Comet Giacobinni- Zinner, EOS, Jan. 14, 1986.

Itoh, T., and K. Hirao, The Sakigake and Suisei encounters with comet Halley, Geophys. Res. Lett., 13, 817, 1986.

Mendis, D.A., and W.-H. Ip, The ionosphere and plasma tails of comets, Space Sci. Rev., 20, 145, 1977.

Mendis, D.A., and H.L.F. Houpis, The cometary atmosphere and its interaction with the solar wind, Rev. Geophys., 20, 885, 1982.

Mukai, T., W. Miyake, T. Terasawa, M. Kitayama, and K. Hirao, Plasma observation by Suisei of solar wind interaction with comet Halley, Nature, 321, 299, 1986a.

Mukai, T., W. Miyake, T. Terasawa, M. Kitayama, and K. Hirao, Ion dynamics and distribution around comet Halley: Suisei observation, Geophys. Res. Lett., 13, 829, 1986b.

Neubauer, F.M., K.H. Glassmeier, M. Pohl, J. Raeder, M.H. Acuna, L. F. Burlaga, N.F. Ness, G. Musmann, F. Mariani, M.K. Wallis, E. Ungstrup, and H.U. Schmidt, First results from the Geotto magnetometer experiment at comet Halley, Nature, 321, 352, 1986.

Niedner, M.B., and J.C. Brandt, Interplanetary Gas XXIII. Plasma tail disconnection events in comets: Evidence for magnetic field line reconnection at interplanetary sector boundaries, Astrophys. J., 223, 655, 1978.

Niedner, M.B., and J.C. Brandt, Interplanetary Gas. XXIV. Are cometary plasma tail disconnections caused by sector boundary crossings or by encounters with high speed streams?, Astrophys. J., 234, 723, 1979.

Niedner, M.B., J.A. Ionson, and J.C. Brandt, Interplanetary Gas. XXVI. On the reconnection of magnetic fields in cometary ionospheres at interplanetary sector boundary crossings, Astrophys. J., 245, 1159, 1981.

Niedner, M.B., Magnetic reconnection in comets, Geophys. Mono., 30, 79, 1984.

Ogino, T., A Three dimensional MHD simulation of the interaction of the solar wind with the earth's magnetosphere: The generation of field-aligned currents, J. Geophys. Res., 91, 6791, 1986a.

Ogino, T., R.J. Walker, and M. Ashour-Abdalla, An MHD simulation of the interaction of the solar wind with the outflowing plasma from a comet, Geophys, Res. Lett., 13, 929, 1986.

Saito, T., K. Yumoto, K.Hirao, K. Saito, T. Nakagawa, and E.J. Smith, A disturbance of the ion tail of comet Halley and the heliospheric structure as observed by Sakigake, Geophys. Res. Lett., 13, 821, 1986.

Schmidt, H.U., and R. Wegmann, Plasma flow and magnetic fields in comets, in Comets: Gases, Ices, Grains and Plasma, edited by L.L. Wilkening, p. 538, University of Arizona Press, Tucson, Arizona, 1982.

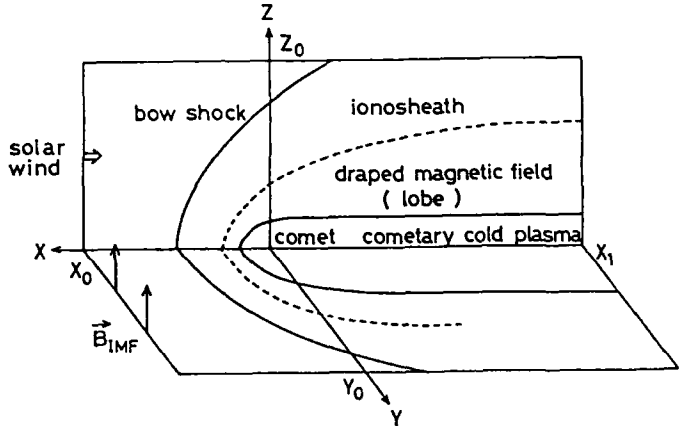

Figure 1. Coordinate system of the solar wind and comet Halley interaction in the 3 dimensional MHD simulation.

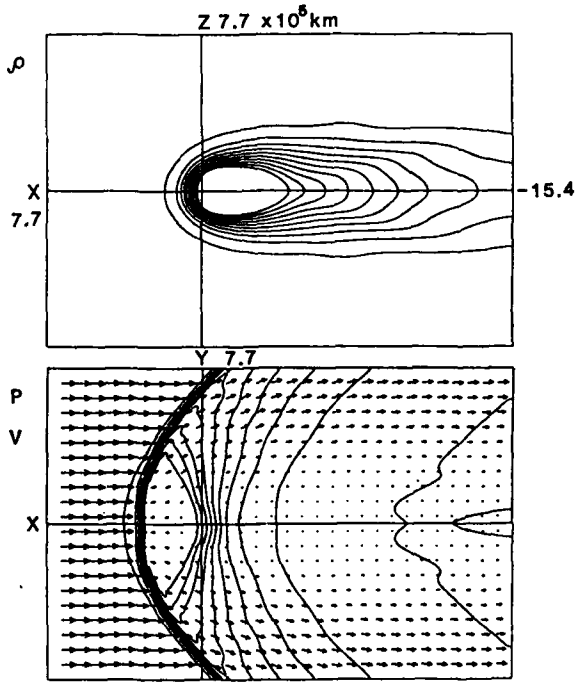

Figure 2. Configurations of the solar wind and comet Halley interaction in the x-z and x-y planes where B_{IMF}=0nT, v_{SW}=500km/s and n_{SW}=15/cc.

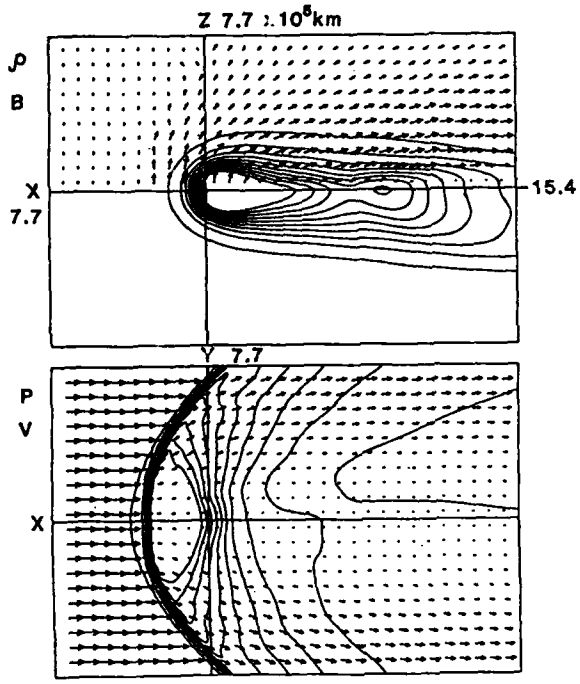

Figure 3. Configurations of the solar wind and comet Halley interaction in the x-z and x-y planes where B_{IMF}=6nT, v_{sw}=500km/s and n_{sw}=15/cc.

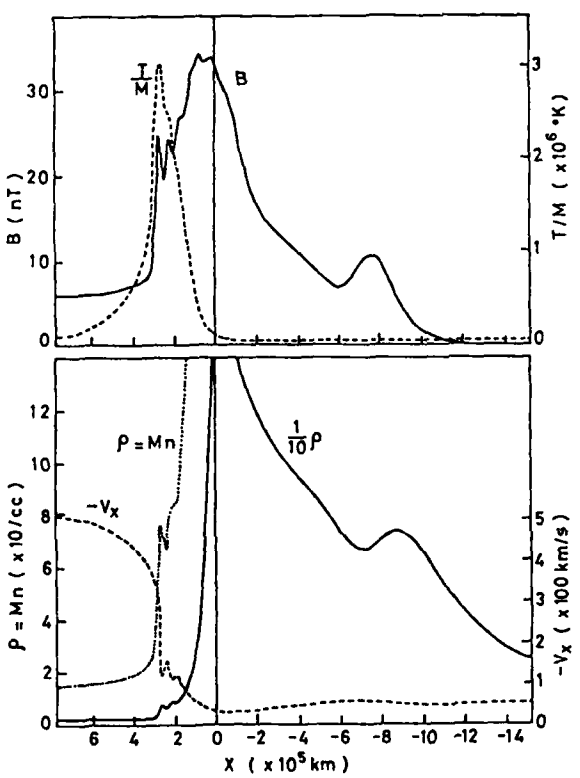

Figure 4. Profiles of the magnetic field, B, temperature, T, x-component of velocity, v_x and density, ρ on the sun-comet Halley line where M is an effective mass ratio to the proton.

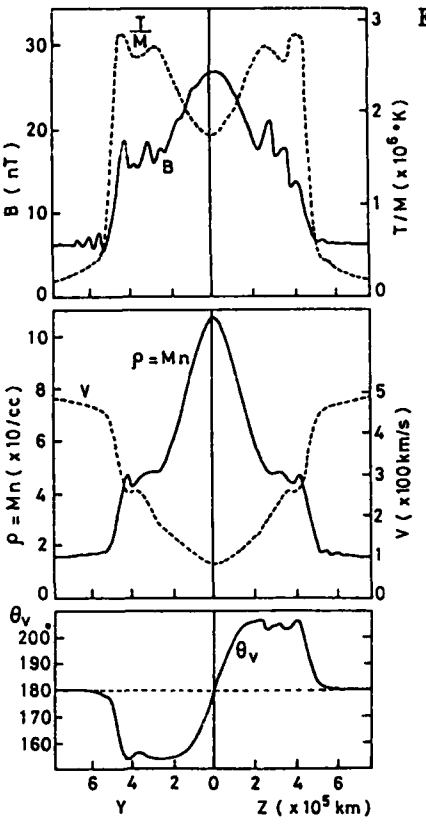

Fig. 5

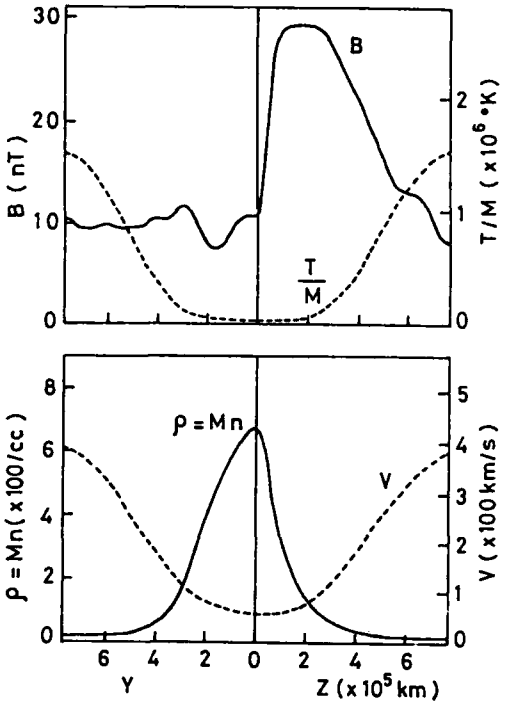

Fig. 6

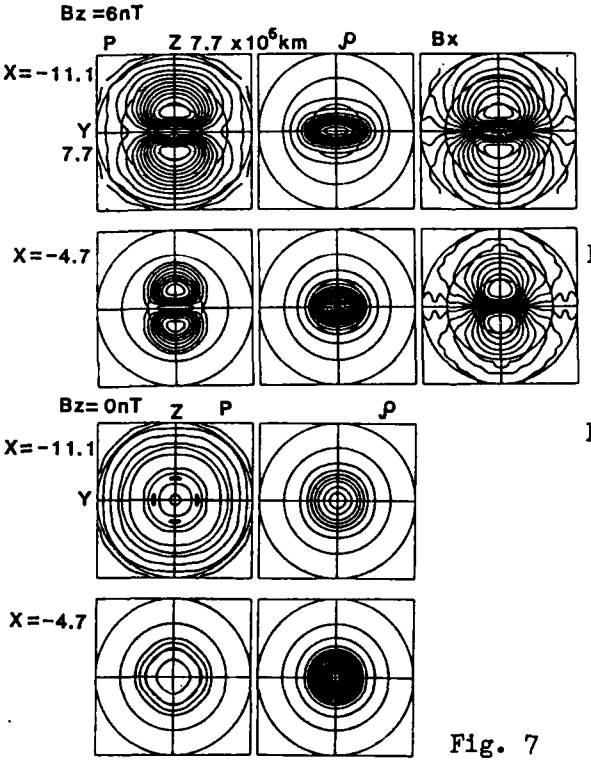

Fig. 7

Figure 5. Profiles of the magnetic field, B, temperature, T, density, ρ, velocity, v and direction of velocity, θ_v at $x=1.7\times10^5$km in the dayside interaction region.

Figure 6. Profiles of the magnetic field, B, temperature, T, density, ρ and velocity, v at $x=-8.1\times10^5$km in the tail region.

Figure 7. Cross sectional patterns of the plasma pressure, p, density, ρ and x-component of magnetic field, B_X in the tail region for B_Z=6nT and OnT. The tail lobes and thin plasma sheet are formed by draping effects of IMF lines.

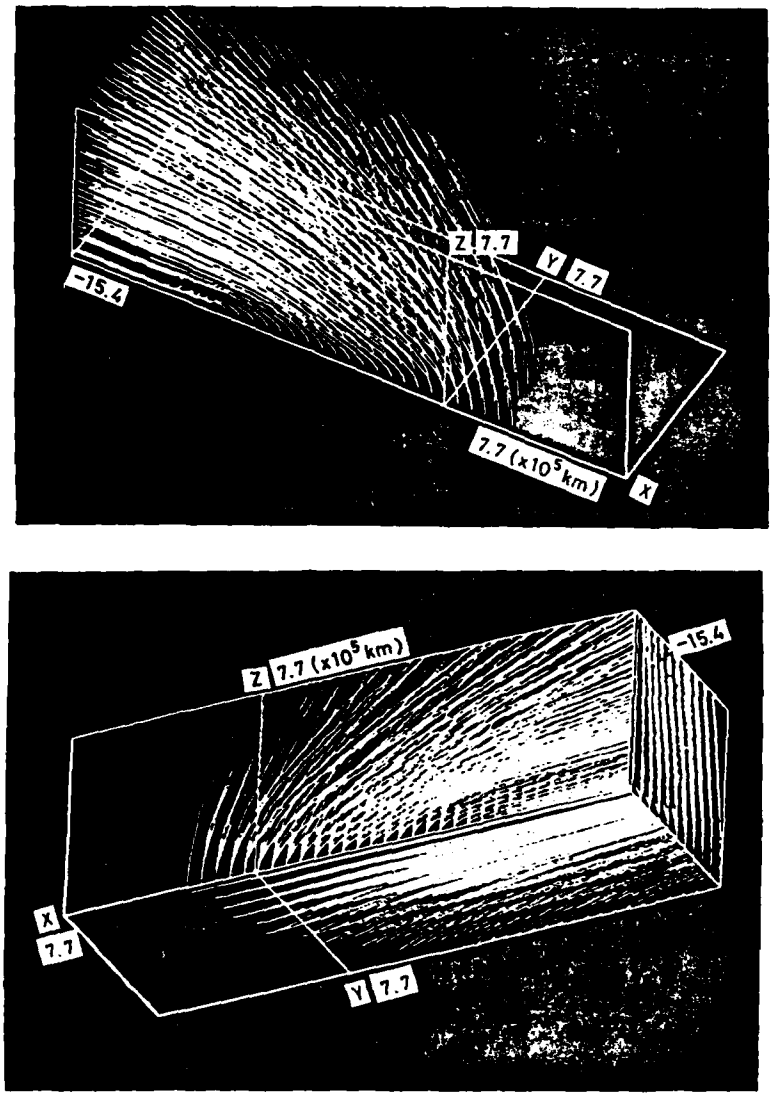

Figure 8. Three dimensional configuration and projection of the magnetic field lines in the interaction regions of the solar wind and comet Halley, where the colour means a measure of the field draping.

NOVA-2: A Kinetic-MHD Stability Code

C. Z. Cheng

Plasma Physics Laboratory
Princeton University
P.O. Box 451, Princeton, N.J. 08544

To study the effect of energetic particles on MHD instabilities, a kinetic-MHD stability code (NOVA-2) has been developed. A low-frequency drift kinetic model is employed to describe energetic particle dynamics and the MHD fluid model for the bulk plasma. NOVA-2 is and extension of the previously developed nonvariational ideal MHD stability code(NOVA) for computing stability of low -n modes in toroidal geometry. Some numerical examples of the energetic particle driven toroidicity-induced shear Alfven waves anf fishbone modes will be presented.

A HYBRID VLASOV-FLUID MODEL WITH KINETIC IONS AND MASSLESS FLUID ELECTRONS*

John M. Dawson

University of California, Los Angeles
Department of Physics,
405 Hilgard Los Angeles, Calif. 90024

We have developed two-and three-dimensional models with kinetic ions and massless fluid electrons. The use of fluid electrons allows us to eliminate the electric field so that it never has to be solved for. We are then able to derive a Vlasov equation for the particle ions and obtain the linear dispersion relation from it. We compare the results from this theory with simulation results from our model; excellent agreement is found. The model exhibits Alfven waves, ion cyclotron waves, low frequency whistler waves and ion Bernstein waves. We have used the model to simulate instabilities such as might be caused by the injection of an energetic neutral beam into the plasma.

We have also implemented a two time step correction technique into code which improves energy conservation by a factor of 10(3) and allows us to use time steps which are an order of magnitude larger.

*Work done in collaboration with F. Kazeminejad, J.N. Leboeuf, and R. Sydora.

GYROKINETIC PARTICLE SIMULATION OF FINITE-BETA PLASMAS

W.W. Lee and T.S. Hahm and R.D. Sydora*

Plasma Physics Laboratory
Princeton University
P.O. Box 451, Princeton, N.J. 08544

Gyrokinetic particle simulation for finite-beta plasmas will be discussed. The four main topics are: 1) the basic formulation of the nonlinear gyrokinetic equations including magnetic perturbations, 2) numerical properties of the simulation plasma such as time step, grid spacing and noise level, 3) special techniques for the evaluation of the generalized Ohm's law, and 4) the relationship between the gyrokinetic equations and the MHD equations.

* University of California, Los Angeles Department of Physics 405 Hilgard Ave. Los Angeles, Calif. 90024

MACROSCALE PARTICLE SIMULATION OF KINETIC ALFVEN WAVES

Motohiko Tanaka[1], Tetsuya Sato[1], and Akira Hasegawa[2]

[1] Institute for Fusion Theory, Hiroshima University, Hiroshima 730, Japan
[2] AT&T Bell Laboratories, Murrray Hill, New Jersey 07974, U.S.A.

Abstract

Simulation of the kinetic Alfven wave, which has many applications in space and fusion plasmas, has been performed by using macroscale (magnetohydrodynamic scale) particle simulation code. Dispersion properties and wave-particle interactions of the kinetic Alfven wave (such as Landau damping and electron acceleration) are successfully obtained in the simulation.

1. Introduction

The kinetic Alfven wave is the Alfven wave for which wave-particle interactions are important[1-3]. This wave has received much attention recently in connection with particle acceleration along the auroral field lines[4,5] and plasma heating in fusion plasmas[6]. The kinetic Alfven wave can also be an active agent to heat the plasma in the solar corona[7] and in Jupiter. Moreover, the structure of the auroral arcs seem to be determined partly by this wave[8] since the latitudinal scale of the arcs ($\approx 100km$) is comparable to the ion Larmor radius.

The existence of the kinetic Alfven wave has been suggested only for limited experimental observations in space and in the laboratory. The Pc 5 magnetic pulsations observed on geostationary satellites[9] show small azimuthal wavelength $\lambda \approx 300-1000km$ and an azimuthal (westward) propagation speed of the order of $10km/sec$. The wavelength and azimuthal phase speed of the kinetic Alfven wave ($k_z/k_x \ll 1$) are theoretically scaled by $2\pi\rho_i$ and $(k_z/k_x)v_A$, respectively, where the typical proton Larmor radius ρ_i on the geostationary orbit is $100km$ and the Alfven speed $v_A \approx 1000km/sec$. In a small tokamak experiment at Lausanne[10], they observed low frequency density fluctuations and spa-

tial damping of the wave which could be the kinetic Alfven wave.

Numerical simulation of Alfven waves were restricted to a scale length comparable to the Debye length λ_e when the conventional particle code was employed. This is because the parallel electric field of the wave, which appears as a consequence of the finite ion Larmor radius, must be solved properly; but the space and time scales of the kinetic Alfven waves are in the magnetohydrodynamic scales. So far, simulation of plasma heating by the antenna-launched Alfven wave was made using a long time scale but Debye length scale Darwin particle code[11].

2. Simulation model and common parameters

Two types of simulations of the kinetic Alfven wave[12] are presented here by using a newly developed macroscale particle simulation code[13] which enables us to follow individual particle dynamics in the MHD scales, namely, in the scale length much larger than the Debye length. In this code, low frequency electromagnetic electric and magnetic fields are solved by eliminating high frequency oscillations such as the light modes; the scalar potential electric field is solved by eliminating Langmuir oscillations. This is achieved by using the decentered time differential scheme which can be coded in semi-implicit algorithm[13] or in full-implicit algorithm. Both ions and electrons are treated as particles with finite mass whose motions are governed by the relativistic version of the equations of motion. The electron motion along the magnetic field line is, therefore, properly treated in this code.

The simulation system is assumed doubly periodic in the x and z directions. An ambient magnetic field is applied in the z direction. The velocity is normalized by the speed of light c, the time by ω_{pe}^{-1}, and the electric and magnetic fields normalized as $eE/m_e c\omega_{pe}$ and $eB/m_e c\omega_{pe}$, respectively. The number of the grids is 32×64 with the system length $L_x=50c/\omega_{pe}$ and $L_z=400c/\omega_{pe}$ (except $L_x=100c/\omega_{pe}$ for the run in the next section and run A in Table 1). This system size corresponds to nearly $250\lambda_e\times2000\lambda_e$. 32768 particles are used for each ion and electron species with the particle size of $a=3c/\omega_{pe}$. The parameters used for the background thermal plasma are the ion beta $\beta=0.36$, the ratio of the electron cyclotron frequency to the plasma frequency $\omega_{ce}/\omega_{pe}=1$ (*i.e.*, $eB_0/m_e c\omega_{pe}=1$), the ion to electron temperature

ratio $T_i/T_e=4$, and the mass ratio $m_i/m_e=50$. Then the Alfven speed becomes $v_A=0.14c$ and the ion Larmor radius $\rho_i=v_i/\omega_{ci}\approx 3c/\omega_{pe}$ where $v_i=(T_i/m_i)^{1/2}$ is the ion thermal speed.

3. Simulation results: Kinetic Alfven wave eigenmode in a thermally near equilibrium plasma

Let us first describe the simulation which successfully detects the kinetic Alfven wave eigenmode in a thermally near-equilibrium plasma by means of power spectrum analysis. As the initial condition, the plasma particles are loaded as quietly as possible without giving any drifts and density perturbations. Figure 1 shows the measured power spectrum for the y component of the magnetic field as functions of the perpendicular wavenumber k_x and the frequency ω for fixed $k_z=2\pi/(400c/\omega_{pe})$. The amplitude of the spectral power is plotted in a logarithmic scale above (to the right of) each baseline for descrete k_x values. Here for the spectral analysis, the maximum entropy method has been emplyed. The peaks in Figure 1 show the presence of the eigenmode in the low frequency range, *i.e.*,$\omega/\omega_{ci}<0.1$. The measured frequency increases with the perpendicular wavenumber when $k_x\rho_i$ becomes comparable to unity. The other small peaks at the higher frequencies $\omega\approx\omega_{ci}$ and $2\omega_{ci}$ are noises due to ion gyromotion. The line in Figure 1 corresponds to the theoretically derived wave frequency for the kinetic Alfven wave. The dependence of this measured eigenmode frequency on the perpendicular wavenumber shows good agreement with the theory.

4. Simulation results: Finite amplitude kinetic Alfven wave and associated particle acceleration

As the second type simulation, the propagation of the finite amplitude kinetic Alfven wave and associated nonlinear effects are presented. Four runs are made by systematically changing the perpendicular wavenumber k_x with the parallel wavenumber k_z being fixed (Table 1). To set up a monochromatic plane wave initially, the density and current perturbations are calculated using an electromagnetic kinetic dispersion

solver. The perturbation assumes the form of $\delta n \sim \sin\psi$, $\delta v_x \sim \sin\psi$, $\delta v_y \sim \cos\psi$, and $\delta v_z \sim \sin\psi$ where $\psi = k_x x + k_z z$. The amplitudes of these initial perturbations are given in Table 1. To represent the density perturbation which is characteristic of the kinetic Alfven wave, the particle spacing is modified in the particle loading. The drift velocities of the aforementioned forms are given to the particles in superposition to the random thermal spread.

The scalar potential field ϕ, the x and z components of the electric field (E_x, E_z) and the magnetic field B_y are shown, respectively, in Figure 2(a), (b) and (c) for $t/\tau_A = 1.8$ of run B where $\tau_A = 2\pi/k_z v_A$ is the Alfven wave period. It is seen that the loaded wave propagates in the direction almost perpendicular to the ambient magnetic field keeping well the initial wave pattern in the two-dimensional magnetic plasma. The major fields are the x-component of the electric field E_x and the y-component of the magnetic field B_y. A small but finite parallel electric field, a unique property of the kinetic Alfven wave, exists as seen in Figure 2(b) owing to the finite Larmor radius effect (this will be discussed below).

The y-component of the magnetic field B_y sliced at constant x positions for runs A, B and C are shown against the positions z and time t in the bird's-eye view plots of Figure 3(a), (b) and (c), respectively. For run A with $k_x \rho_i = 0.19$, the loaded wave propagates with the parallel phase velocity close to the Alfven speed (see also Table 1). As the perpendicular wavenumber k_x increases for run C, the parallel phase velocity becomes appreciably large, as seen in Figure 3(c).

The phase velocity of the waves in the direction parallel to the ambient magnetic field, ω/k_z, is plotted in Figure 4 against the perpendicular wavenumber which is normalized with the ion Larmor radius, $k_x \rho_i$. As $k_x \rho_i$ increases, the parallel phase velocity increases parabolically as shown by solid circles in the figure. The solid line shows the theoretical dispersion relation for the kinetic Alfven wave.

Shown with the open circles in Figure 4 are the damping increments of the loaded waves. The numerical damping rate of the wave is estimated to be $\gamma_N/k_z v_A < 3 \times 10^{-3}$ at most, which is negligibly small except for run A. For run D with $k_x \rho_i \approx 1.1$, the damping increment is so large that the loaded wave decays substantially in a few wave periods $[(2\pi\gamma/\omega)_{obs} \approx 0.5]$. The dashed line in the figure shows the theoretical

damping increment of the kinetic Alfven wave. Both the measured parallel phase velocity and the damping increment of the loaded waves are in excellent agreement with the theory.

The damping of the kinetic Alfven wave occurs due to the Landau damping. Under the parameters used in this study, the damping is primarily due to the electrons. The initial Maxwellian distribution of the electrons parallel to the ambient magnetic field in Figure 5(a) evolves into a non-symmetric one with respect to $v_z=0$, which has a plateau on the positive side around $v_z \approx \omega/k_z (\approx v_e)$ as shown in Figure 5(b). However, the locations of both edges of the velocity distribution remained unchanged. The parallel electron effective temperature continues to increase, especially when the wave amplitude is large. On the other hand, ion parallel temperature stays almost the same. The electron heating rate is found to be proportional to the damping increment of the wave for runs A to D, which is scaled as $\partial T_{ez}/\partial t \approx 16\gamma\epsilon_B$ where $\epsilon_B = \delta B_y^2/16\pi$ is the magnetic field energy.

The electrons are monotonically accelerated towards the direction of the wave propagation. The acceleration is not appreciable for run A. For runs B, C and D, the acceleration occurs in the early time when the electric field energy $\epsilon_E = \delta E_x^2/16\pi$ is large, *i.e.*, $\epsilon_E/T_e > 2\times 10^{-3}$. At the end of run D, the total increase in the electron parallel velocity amounts to nearly 10% of the initial electron thermal speed. The increasein the parallel momentum density of electrons is found, with an accuracy of 10%, to be in agreement with the decrease in the total wave momentum density, $(\delta B_y^2/8\pi)(k_z/\omega)$. This fact supports the validity of nonlinear results obtained by using the macroscale particle simulation code.

The electron acceleration and heating are attributed to the small but non-vanishing parallel electric field. In order to estimate the torque on the electrons, the parallel electric field is averaged with the electron density as a weight, *i.e.*, $<(-e)E_z\delta n_e>/<n_e>$. (The normal average field $<E_z>$ vanishes exactly due to the periodicity.) The weighted average electric field becomes $\approx 1\times 10^{-5} eB_0$ for run C when the electron acceleration is occurring and is consistent with the time rate of increase in the parallel electron momentum (note the initial wave amplitude $E_{xk}(t=0) \approx 3\times 10^{-2} B_0$). This results from the occurrence of a positive correlation between the electron motion and the electric field, *i.e.*, the phase difference between the electron density perturbation and the

electric field becomes within 90 *degrees*. Using the measured values, $<(-e)E_z\delta n_e>/<n_e>\approx 1\times 10^{-5}eB_0$ and $(<E_z^2>)^{1/2}\approx 1\times 10^{-4}B_0$, the phase angle difference is estimated to be 78 *degrees*. (Note that $<\sin\psi\sin(\psi+\delta)>=\cos\delta/2$ where the average is made over ψ.) Similarly, the energy transfer rate to the electrons from the wave is estimated by measuring $<(-e)n_e v_{ez}E_z>/<n_e>$. This quantity becomes positive definite, *i.e.*, $4\times 10^{-6}ceB_0$ for run C, only during the electron heating. These facts quantitatively verify the electron acceleration and heating observed in the simulation.

5. Conclusion

A successful application of the newly developed macroscale particle simulation code was shown for the kinetic Alfven wave, which has many applications in space and astrophysical plasmas. The detailed wave characteristics, the dependences of the frequency and the Landau damping on the perpendicular wavenumber, were examined and excellent agreements were found between the simulation and theoretical prediction. Some fundamental nonlinear interactions of the kinetic Alfven wave with the particles (parallel acceleration of the electrons) were also found.

The present simulation work assumed a periodic (closed) system. In the space environment, however, particle acceleration (heating) occurs in an open geometry. Moreover, the Alfven speed changes its magnitude in an inhomogeneous plasma, for example, along the magnetic field line of the earth. In that case, particles resonating with the wave may be accelerated and convected toward the direction of the wave propagation. Consequently, the distribution function of the particles may evolve into a bi-Maxwellian one rather than formation of the plateau. These specific problems of the kinetic Alfven wave will be reported in the future.

Acknowledgments. This work was supported by a grant-in-aid from the Ministry of Education, Sciences and Culture of Japan. It was also supported by Toray Science Foundation, NSF grant ATM 12512 and NASA grant NAGW-894.

References

1. A.B. Mikhailovskii, and L.I. Rudakov, The stability of a spatially inhomogeneous plasma in a magnetic field, *Zh. Eksp. Theor. Fiz., 44*, 912, 1963 [*Sov. Phys.-JETP, 17*, 621, 1963].
2. R.J. Stefant, Alfven wave damping from finite gyroradius coupling to the ion acoustic mode, *Phys. Fluids, 13*, 440, 1970.
3. A. Hasegawa, and L. Chen, Kinetic processes in plasma heating by resonant mode conversion of Alfven waves, *Phys. Fluids, 19*, 1924, 1976.
4. A. Hasegawa, Particle acceleration by MHD surface wave and formation of aurora, *J. Geophys. Res., 81*, 5083, 1976.
5. C.K. Goertz, Kinetic Alfven wave on auroral field lines, *Planet. Space Sci., 32*, 1387, 1984.
6. L. Chen, and A. Hasegawa, Plasma heating by spatial resonance of Alfven waves, *Phys. Fluids, 17*, 1399, 1974.
7. J.A. Ionson, Resonant absorption of Alfven surface waves and the heating of the solar coronal loops, *Astrophys. J., 226*, 650, 1978.
8. K. Watanabe, and T. Sato, A numerical simulation of magnetosphere-ionosphere coupling: Preliminary results, *J. Geophys. Res., 91*, 6973, 1986.
9. K. Takahashi, P.R. Higbie, and D.N. Baker, Azimuthal propagation and frequency characteristic compressional Pc 5 waves observed at geostationary orbit, *J. Geophys. Res., 90*, 1473, 1985.
10. R. Behn, G.A. Collins, J.B. Lister, and H. Weisen, Observation of density fluctuations at the resonance layers during Alfven wave heating, *LRP No.296*, Ecole Polytechnique Federale de Lausanne (Switzerland), 1986.
11. J.L. Geary, T. Tajima, J.-N. Leboeuf, E.G. Zaidman, and J.H. Hahn, Two and three dimensional magneto-inductive particle codes with guiding center electron motion, *IFS Report No.239*, University of Texas, 1986.
12. M. Tanaka, T. Sato, and A. Hasegawa, Numerical simulation of the kinetic Alfven wave, *EOS Trans.* (American Geophysical Union) 67, 1164, 1986; *Geophys. Res. Lett.*, in press (1987).
13. M. Tanaka, and T. Sato, Macroscale particle simulation of relativistic electron beam injection into a magnetized plasma channel, *Phys. Fluids, 67*, 1164, 1986.

Table 1

The initial perturbation of density, δn, and the drift velocities, $\delta v_x, \delta v_y, \delta v_z$, for the ions (electrons) in the left (right) column (upper part). The measured phase velocity (frequency) (ω/k_z) and the damping increment γ of the wave (lower part). k_x and k_z are, respectively, the perpendicular and parallel wavenumber; ρ_i is the ion gyroradius; v_A is the Alfven speed.

	Run A	Run B	Run C	Run D
$\delta n/n_0$	(0.069, 0.071)	(0.126, 0.129)	(0.219, 0.227)	(0.275, 0.288)
$\delta v_x/c$	$(2.5\times10^{-3}, -5.4\times10^{-4})$	$(2.4\times10^{-3}, -6.4\times10^{-4})$	$(2.3\times10^{-3}, -6.7\times10^{-4})$	$(2.2\times10^{-3}, -6.7\times10^{-4})$
$\delta v_y/c$	$(-2.7\times10^{-2}, -2.8\times10^{-2})$	$(-2.4\times10^{-2}, -2.8\times10^{-2})$	$(-1.6\times10^{-2}, -3.1\times10^{-2})$	$(-8.2\times10^{-3}, -3.6\times10^{-2})$
$\delta v_z/c$	$(\approx0, 1.2\times10^{-2})$	$(\approx0, 2.4\times10^{-2})$	$(\approx0, 4.7\times10^{-2})$	$(\approx0, 6.9\times10^{-2})$
$\tan^{-1}(k_x/k_z)$	76.0	82.9	86.4	87.6
$k_x\rho_i$	0.19	0.38	0.76	1.13
$\omega/k_z v_A$	1.03	1.07	1.41	1.98
$\gamma/k_z v_A$	$(7.2\pm3.6)\times10^{-3}$	$(1.3\pm0.7)\times10^{-2}$	$(5.9\pm0.9)\times10^{-2}$	$(1.6\pm0.2)\times10^{-1}$

Figure captions

Fig. 1 The power spectrum for the y-component of the magnetic field in a thermally near-equilibrium plasma. The abscissa is the perpendicular wavenumber normalized with the ion Larmor radius, and the ordinate is the frequency ω/ω_{pe}. The power amplitudes are plotted in a logarithmic scale above (to the right of) each baseline with the 10^4 range between two adjacent baselines.

Fig. 2 The scalar potential field ϕ, the x and z-components of the electric field (E_x, E_z), and the y-component of the magnetic field B_y for $t/\tau_A = 1.8$ of run B. The maximum amplitudes are (a) $e\phi/m_e c^2 \approx 0.22$, (b) $eE_x/m_e c\omega_{pe} \approx 3.5 \times 10^{-2}$, and (c) $eB_y/m_e c\omega_{pe} \approx 0.17$.

Fig. 3 The y-component of the magnetic field sliced at constant x positions plotted against position z and time t for runs A, B and C from top to bottom, respectively.

Fig. 4 The parallel phase velocity (solid circles) and the damping increment (open circles) of the initially loaded waves of runs A to D. The solid and dashed lines, respectively, show the theoretical parallel phase velocity and the damping increment.

Fig. 5 The electron velocity distribution function parallel to the ambient magnetic field at (a) $t = 0$ and (b) $t = 1.8\tau_A$ of run C. The scale in the ordinates is the same in (a) and (b).

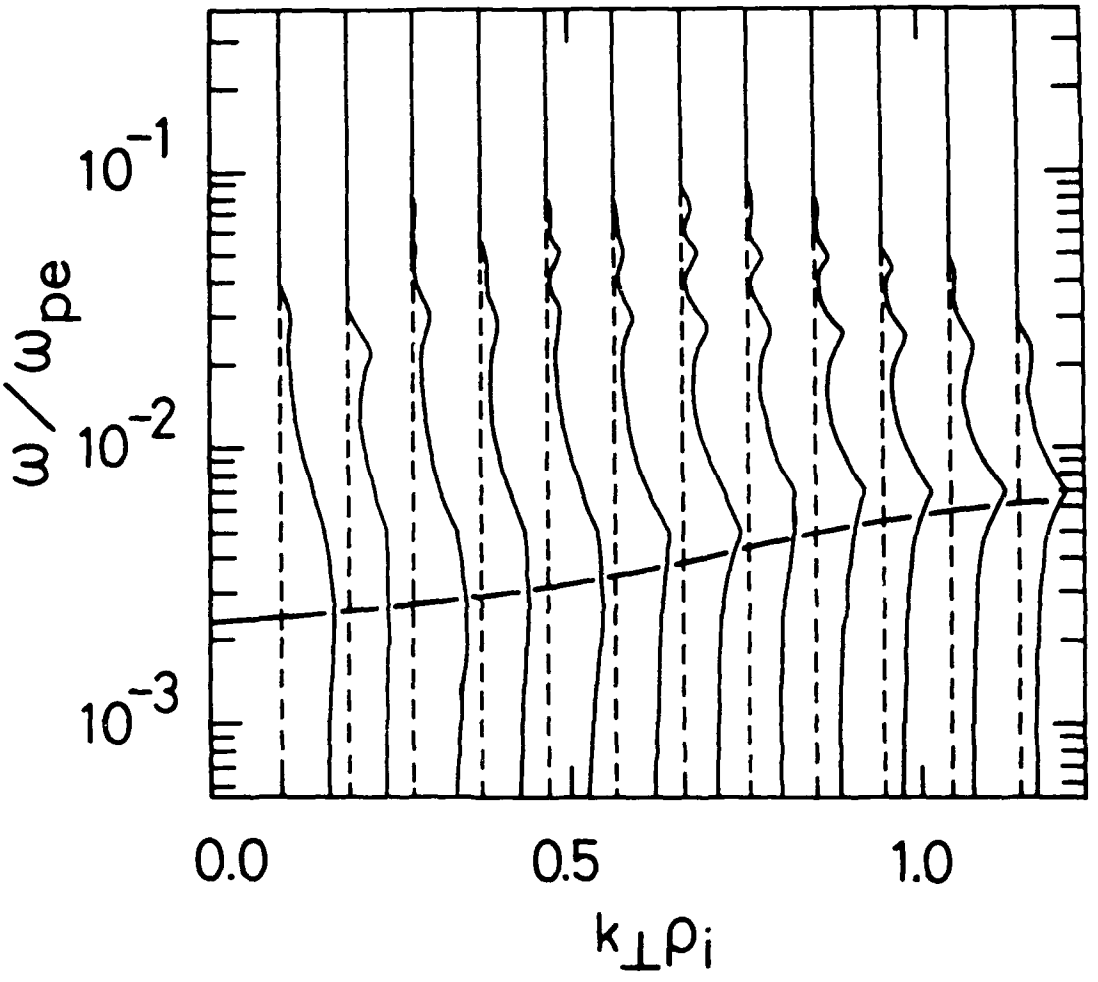

FIG. 1

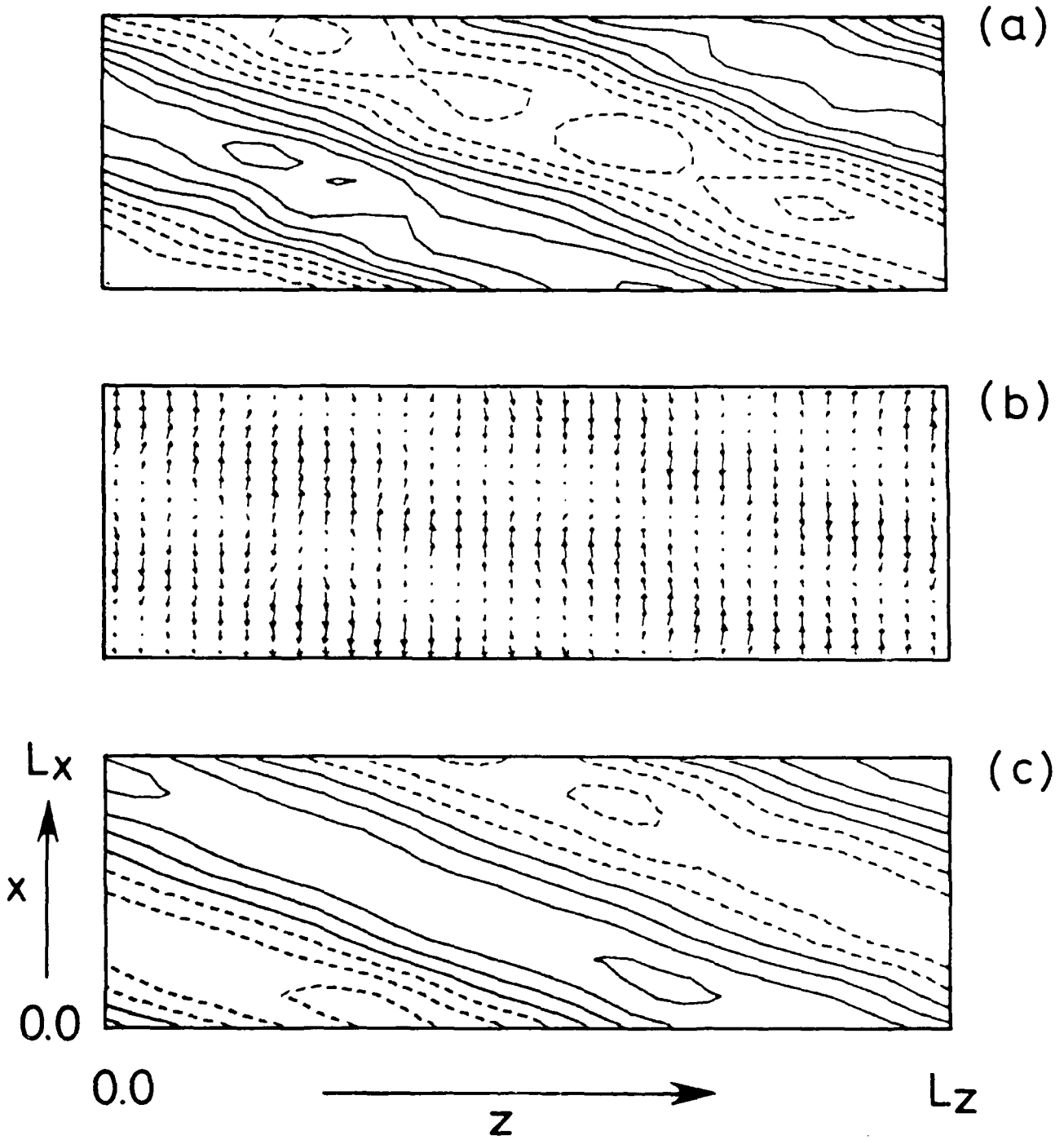

FIG. 2

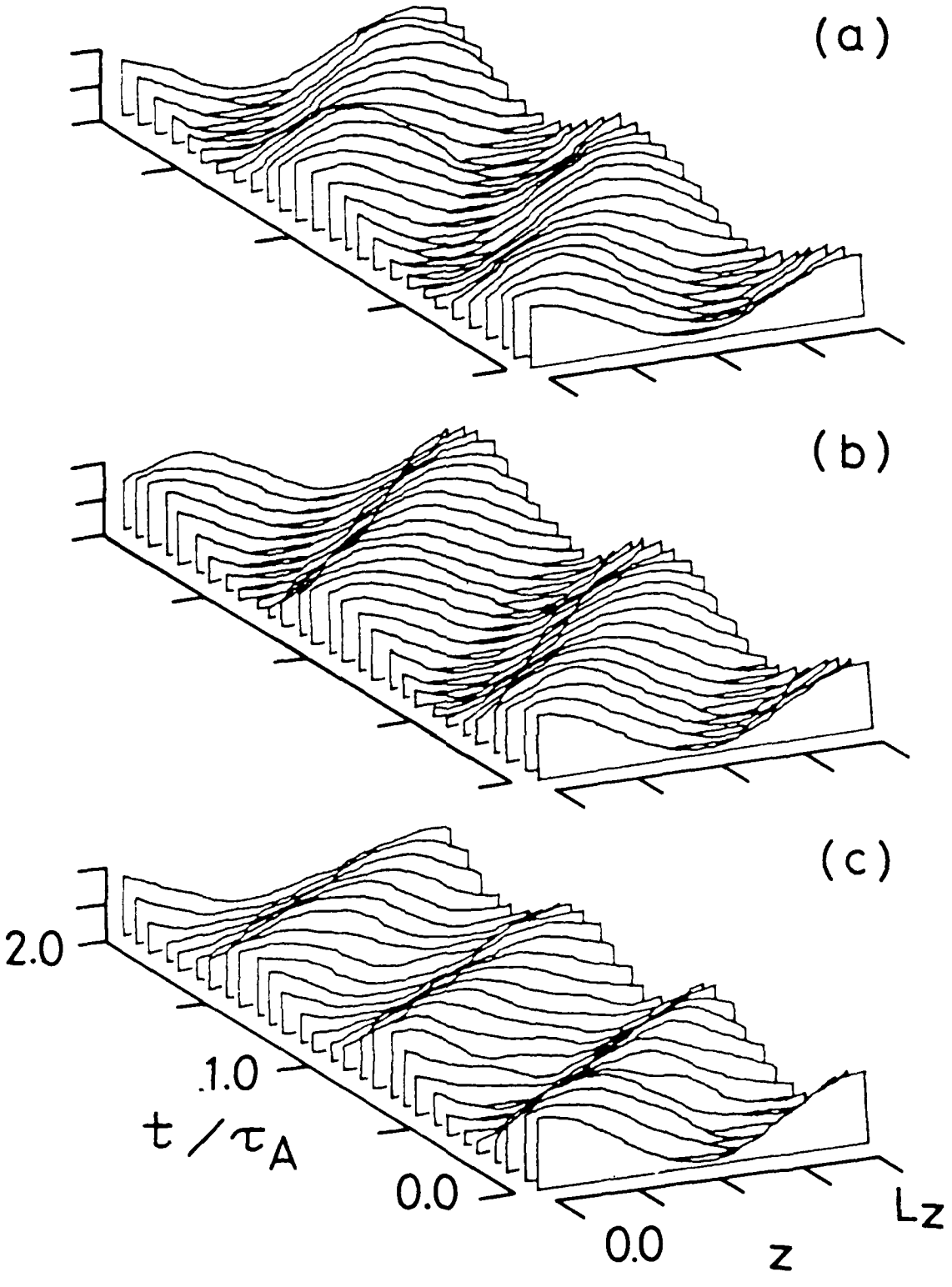

FIG. 3

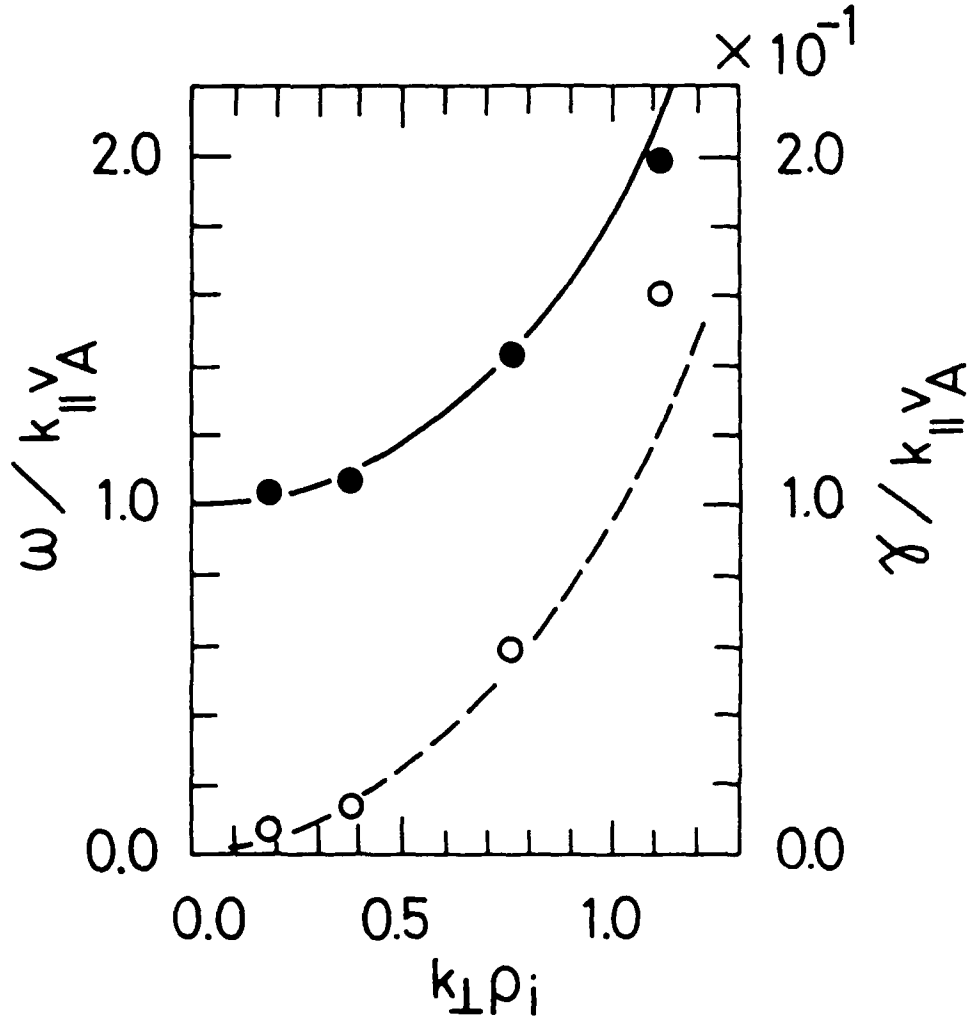

FIG. 4

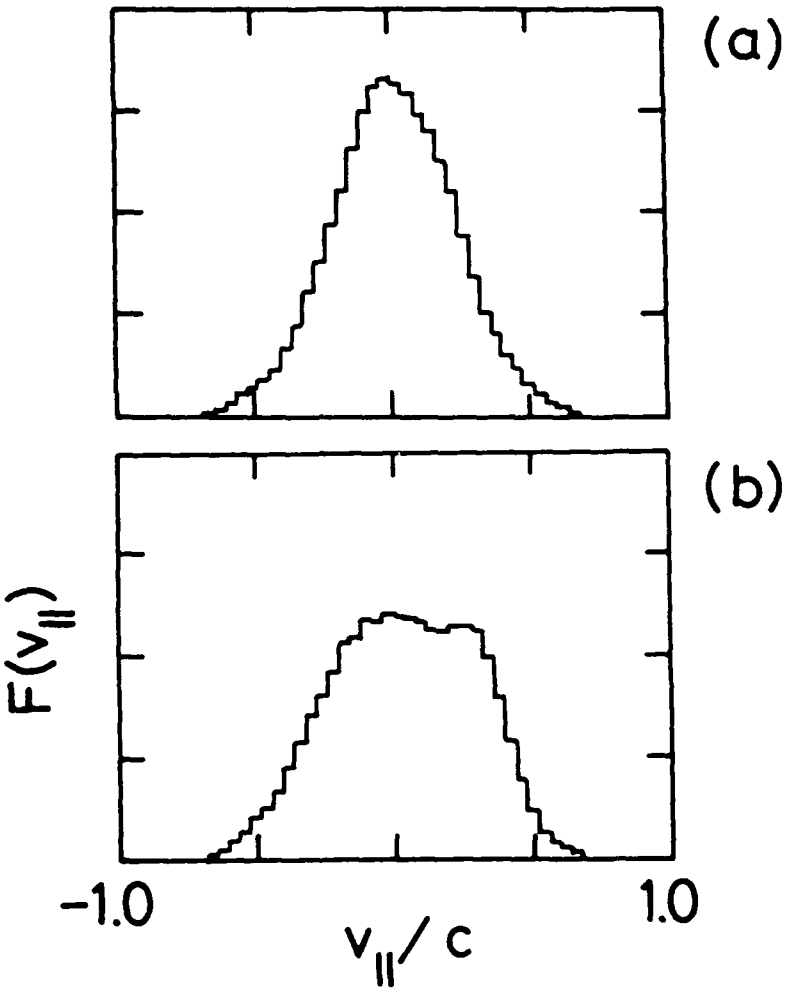

FIG. 5

PARTICLE-PARTICLE PARTICLE-MESH CODE FOR NONIDEAL HIGH DENSITY PLASMA AND ITS APPLICATION ON RAYLEIGH-TAYLOR INSTABILITY IN ICF PLASMA*

Katsunobu Nishihara

Institute of Laser Engineering, Osaka University
Suita, Osaka 565

In an inertial confinement fusion plasma, the Coulomb coupling constant, $\Gamma \equiv (Ze)^2/ak_BT$, becomes of the order of one, where a is the Wigner-Seitz radius defined as $a=(3/4\pi ni)^{1/3}$. In such a strongly coupled plasma ($\Gamma \geqq 1$), the Coulomb interaction can not be treated as perturbations and the system begins to exhibit features qualitatively different from those in an ideal collisionless plasma. To study dynamics of a strongly couples plasma, we have developed three-dimensional two-component particle-particle particle-mesh code. The code calculates exact Coulomb forces among particles within a short distance, while the PIC method is used for long distance forces. We have observed the pair distribution functions and the result has been found to agree quite well with the hypernetted chain theory and Thomas-Fermi model.

We use the code to study effect of a contact potential on the Rayleigh-Taylor instability between two plasmas with different charge state. The preliminary results will be discussed.

*Work done in collaboration with H. Furukawa and M. Kawaguchi

TRIPIC: Triangular-Mesh Particle-in-Cell Code for LIB Diode

Shigeo Kawata, Masami Matsumoto and Yukio Masubuchi

The Technological University of Nagaoka
Nagaoka, Niigata 940-21, Japan

A particle-in-cell code using triangular meshes (TRIPIC code) is described to simulate the motion of charged particle in an electromagnetic field self-consistenly in some complicated computational space region. TRIPIC is fitted for the simulation of LIB (Light Ion Beam) diode, for example.

1. Introduction

Up to now many particle simulations have been done [1-5] and many particle-in-cell (PIC) codes [2,6,7] have been developed to study a self-consistent interaction between charged particles and electromagnetic field. In many codes usually rather regular space meshes are employed to describe the computational regions. On the other hand, recently, we have a problem of, for example, intense LIB diode simulation in which the computational space region has a nonuniform or curved boundary. TRIPIC code employs triangular space meshes to simulate such the problem. The paper presents the description for TRIPIC code.

In order to solve the electromagnetic field on triangular meshes, we have a finite element method and finite differencial one which is, for example, developed by Winslow [8]. Here we focus on the latter method. Winslow developed the numerical method in nonuniform triangular meshes to solve the Poisson type of equation. SUPERFISH code [9] was also developed by the similar method. A descendant of these two codes is TRIDIF code [10] which is a time-dependent code to solve a magnetic

diffusion. Based on this method the Poisson equation and the equation of magnetic vector potential are solved in TRIPIC code.

In TRIPIC code a particle pusher is solved by the Buneman scheme. The interaction between particles and space meshes are accomplished by a simple weighting method.

2. Structure of TRIPIC code

At first space meshes are generated in the x-y or r-z plane. In the space-mesh generator two Poisson type of equations are solved [8], because of the 2.5 dimensional code of TRIPIC. The logical meshes are composed of two kinds of lines with labels K and L, shown in Fig. 1. We have to do the mapping to the real space region. In the real space mapped lines are considered to be like equi-potential lines. If the two Poisson equations are solved inversely in the logical space with the appropriate boundary conditions, the numbering of the space meshes can be accomplished. Figure 4-a) shows an example for the generated meshes.

The following basic equations are used in TRIPIC code:

$$dP/dt = (q/m)\ (\ E + VxB\ ),$$

$$\nabla xE = -\partial B/\partial t, \quad \nabla xB = \mu(\ J + \partial D/\partial t\ ), \quad D = \varepsilon E$$

$$\nabla \cdot D = \rho$$

TRIPIC code employs the Coulomb gauge and, the Poisson equation for the static electric potential and the equation of the magnetic vector one are solved on triangular meshes. These equations can be solved on the cartesian or cylindrial coordinate in TRIPIC code. Following Winslow the descretization method is described for the generalized Poisson equation:

$$\partial\phi/\partial t = \nabla(\lambda\nabla\phi) + s,$$

$$\nabla\phi = [(\phi_i - \phi)S^{+}_{i+1} - (\phi_{i+1} - \phi)S^{+}_{i}]/(S_i S^{+}_{i+1}) .$$

The computational region covered by triangular mashes has sets of six triangles surrounding a vertex, that is called the primary mesh. The area of the secondary mesh is one third of the primary one, shown in Fig. 2. Over the secondary mesh the generalized Poisson equation is integrated, assuming the gradient of physical quantities constant in each triangles. The Gauss law is adapted to the first term at the right hand side of the above equation. Then the sum of the flux is computed. Finally we obtain the descretized equation of the generalized Poisson one on the triangular meshes:

$$(\phi^{n+1} - \phi^{n})/\partial t = [(\Sigma w_i (\phi_i - \phi) + S)/G]^{n+1/2}$$

$$w_i = (\lambda_{i+1/2} \cot\theta_{i+1/2} + \lambda_{i-1/2} \cot\theta_{i-1/2}),$$

$$G = \Sigma a, \qquad \Sigma = \Sigma_{i=1-6}, \qquad a: \text{area of the secondary mesh}$$

$$S = \Sigma s_{i+1/2} a_{i+1/2} .$$

By using this method basic equations are also descretized for the electromagnetic field. The resulting matrixes of the basic equations are solved by the direct Gaussian forward- and backward-subtraction method [9].

By using electric and magnetic fields particles are pushed. In order to find the electric and magnetic fields on a particle we should find the particle position in the logical space. If the logical meshes are numbered in series, we remember the position at the former time step and the time step is enough small, to find the new particle position is

accomplished by searching the several meshes just surrounding the mesh in which the particle was located at the former time step. To accomplish the interaction between the particles and the space meshes each particle has a finite radius and meshes locating in this circle interact with the particle. In the weighting method the weight is defined by the inverse of the distance between the particle and the mesh points(see Fig. 6). By this method the new current and charge densities are computed.

In addition TRIPIC has an additional subroutine for the particle generation at the specified region as an option. The generation rule is the space-charge limitted condition. For example electrons and ions generated at the electrodes in an intense-ion diode[11].

As a boundary condition the Dirichlet-boundary condition is used for the static Poisson equation. For example at the anode surface in an intense-ion diode the applied voltage is imposed at the anode surface. At the surface of the perfect conductor the condition that a parallel electric field is zero is imposed. This is done even at the curved boundary surface by using the coupled equation of the vector potential which is the summed-up equation of parallel component of equations for Ax (or Ar) and Az in the x-z (or r-z) plane.

As a summarization of this section we present the time chart of TRIPIC.

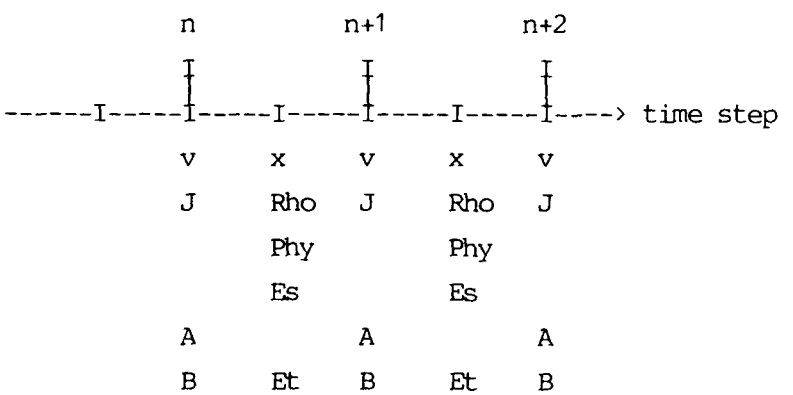

Here v is the velocity, x the space coordinate, Rho the charge density, Phy the static electric potential, Es the static electric field, J the current density, A the vector potential, B the magnetic field and Et the transeverse electric field.

3. Example of Computation

In this section examples of numerical computations are presented.

3.1 Mesh generation

The mapping is done from the uniform mesh in the logical space (K-L space, see Fig. 1) to the nonuniform real space mesh. Figure 4-a) shows an example of mapped meshes. In Fig. 1 the computational region is the non-hatched region and the hatched outer region is used for the boundary treatment of particles and the fields. Therefore the mesh size of most outer region has no need to be same with the mesh size in the computational region.

3.2 Potential

A computed electric static potential in the region of Fig. 4-a) is presented in Fig. 4-b). The equi-potential lines are plotted by dotted lines. In this case curved electrodes has constant voltages in time, respectively and the system is cylindrically symmetric.

Figure 5 shows the propagation of an electromagnetic single-mode wave. The propagation of vector potential is presented in Fig. 5-a) and Fig. 5-b) shows the electric and magnetic fields. In the direction of the wave vector the cyclic boundary condition is used.

3.3 Particle

In order to check TRIPIC code we simulate the Child-Langmuir current in a diode gap. Figure 7 shows an example of electron map in the diode gap. In this case a gap distance is 0.5 cm and the applied

voltage is 1 volt because of the avoidance of the particle bending by the self-magnetic field. The simulated current coincides well with the analytical value which is obtained only in the case of no magnetic field. The particle emission is controled by the space-charge limit condition.

4. Conclusion

A particle-in-cell code TRIPIC was developed to do the particle simulation in the irregular boundary by using the nonuniform triangle meshes. The electromagnetic fields are solved by the finite differencial method in the nonuniform triangle meshes. The particles are pushed by solving the relativistic equation of motion. The interaction between the particles and the meshes can be accomplished by the simple weighting method. The weight is proportional inversely to the distance between the particle and the mesh. Our particle has a shape of circle in 2 dimensional space. The radius is comparable with the mesh size. The meshes inside of the circle can interact with the particle. This weighting method can be easily switched to the other weighting one.

TRIPIC code can simulate the space region with the irregular boundary. Therefore, for example, TRIPIC is fitted for the simulation of an ion or electron diode [11] which has a curved electrodes to focus the beam.

The technique in TRIPIC code can be also used in other type of PIC code, that is fluid PIC code.

Acknowledgement

This work is partly supported by the Institute of Plasma Physics of Nagoya University, Japan.

[1] J. M. Dawson, Rev. Mod. Physics, 55(1983)403.

[2] C. K. Birdsal and A. B. Langdon, "Plasma Physics via Computer Simulation", McGraw-Hill, 1985.

[3] R. W. Hockney and J. W. Eastwood, "Computer Simulation Using Particles", McGraw-Hill, 1981.

[4] for example, T. Tajima and J. M. Dawson, Phys. Rev. Lett., 43(1979)267. "Special Issue on Plasma-Based High-Energy Accelerators", IEEE Transactions on Plasma Science, PS-15(1987).

[5] for example, S. A. Slutz, D. B. Seidel and R. S. Coats, J. Appl. Physics, 59(1986)11.

[6] for example, A. B. Langdon and B. F. Lasinski, Meth. Comp. Physics, 16(327). J. P. Boris, Proc. Fourth Conf. Num. Sim. Plasmas, Naval Res. Lab., (1970)3.

[7] for example, B. Goplen, R. E. Clark and S. J. Flint, Mission Res. Corp. MRC/WDC-R-001, (1979). J. P. Quintenz, J. Appl. Phys., 49(1978)4377.

[8] A. M. Winslow, J. Comp. Physics, 2(1967)149.

[9] K. Halbach and R. F. Holsinger, Particle accl., 7(1976)213.

[10] J. R. Freeman, J. Comp. Physics, 41(1981)142.

[11] J. P. VanDevender, et. al., Proc. the 6th Int. Conf. on high-Power Particle Beams, (1986)43.

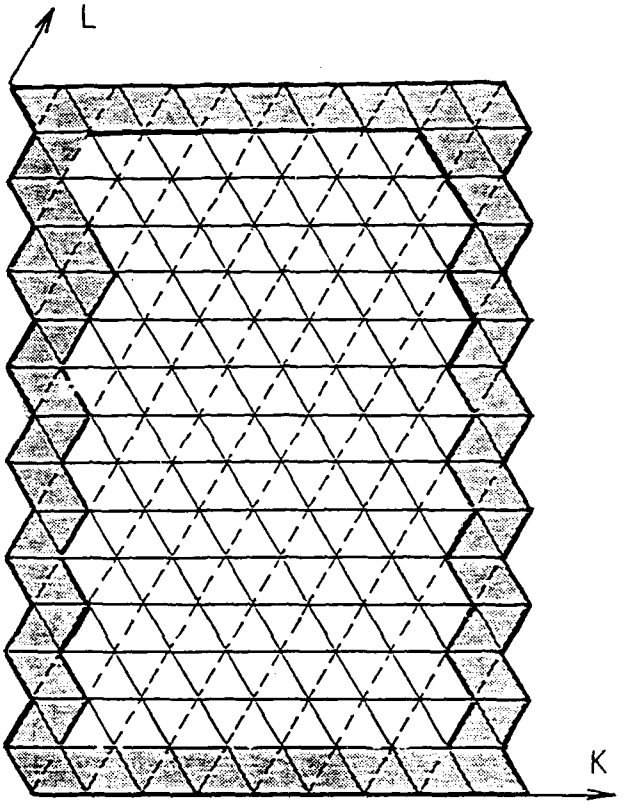

Fig. 1 Mesh in Logical Space

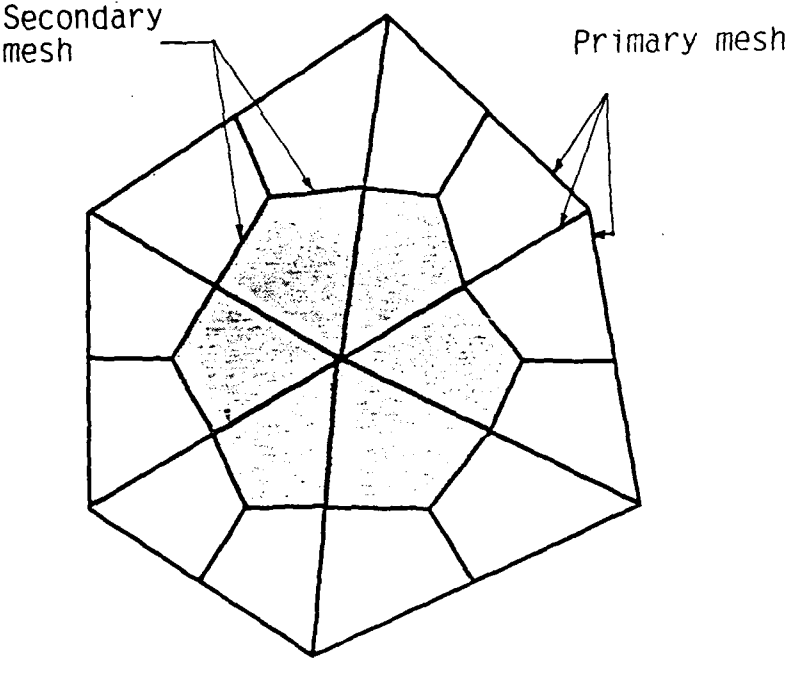

Fig. 2 The primary and secondary meshes in real space

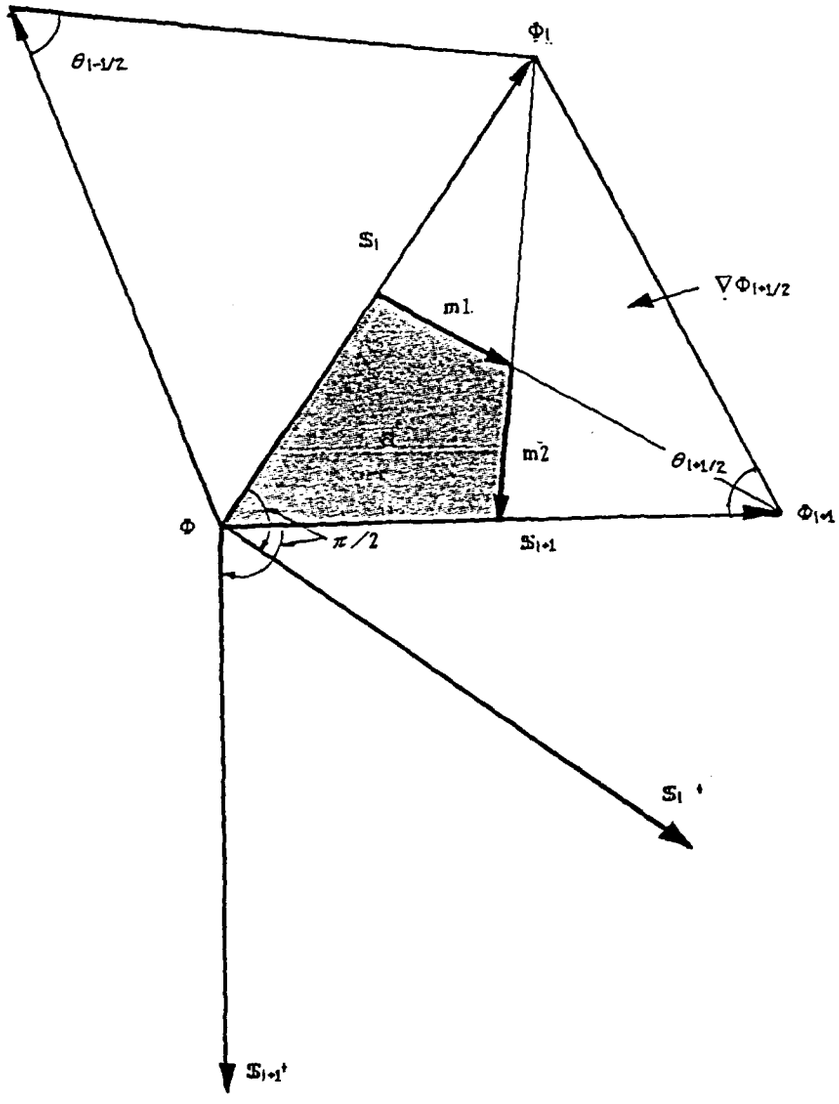

Fig. 3 Notations. A notation of a is the area of the secondary mesh.

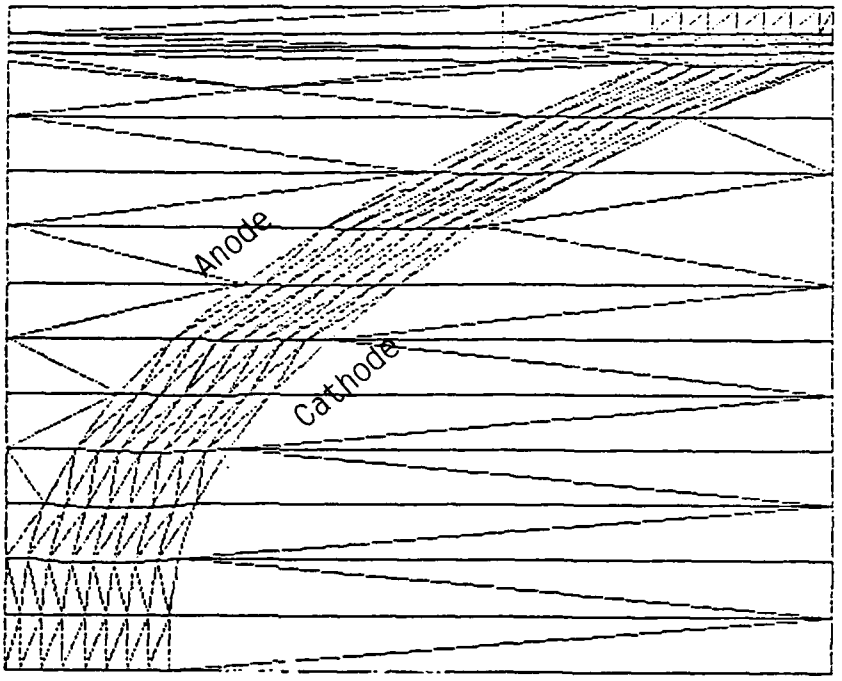

Fig. 4-a) Generated mesh. The computation region is covered by fine meshes.

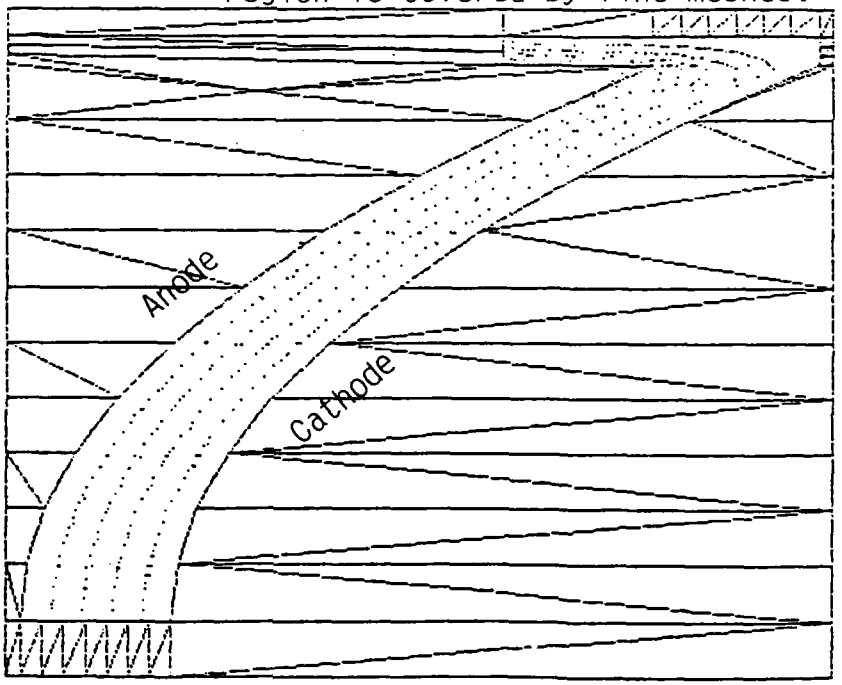

Fig. 4-b) Equi-potential line of static electric field in a diode anode-cathode gap.

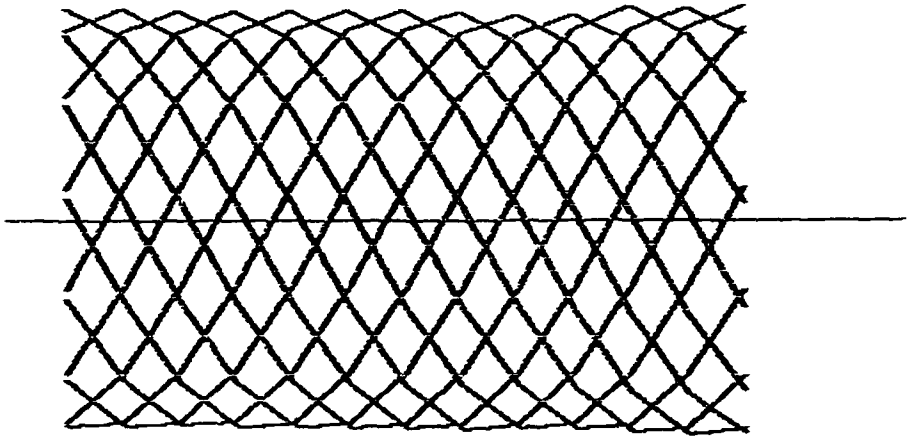

Fig. 5-a) Vector potential in the case of single-em-wave propagation

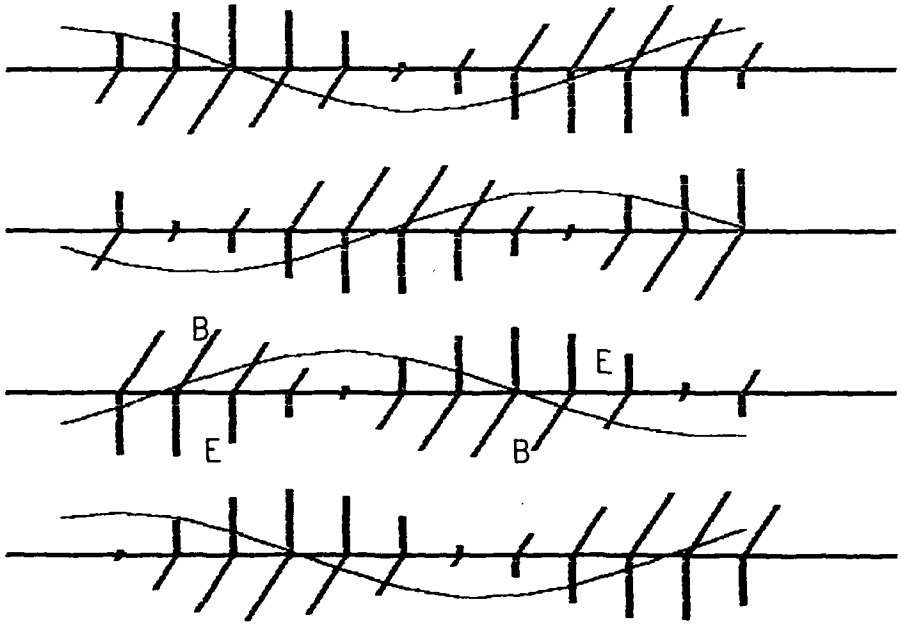

Fig. 5-b) Electromagnetic wave propagation

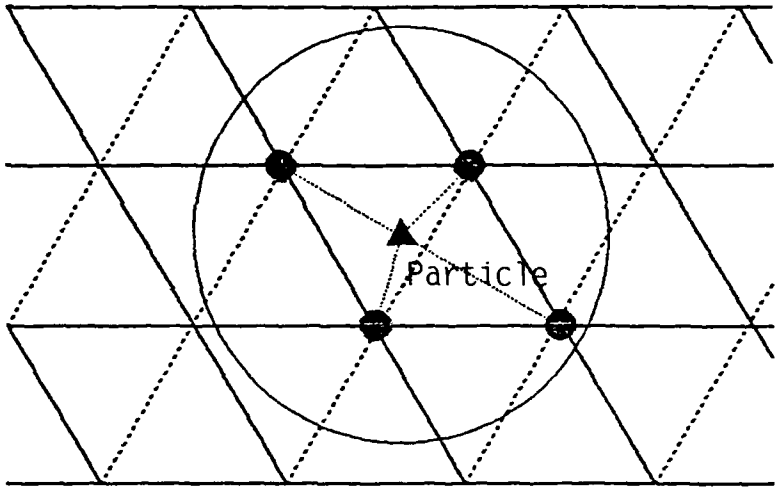

Fig. 6 A particle has a finite radius In TRIPIC code and interacts with grids inside of the circle.

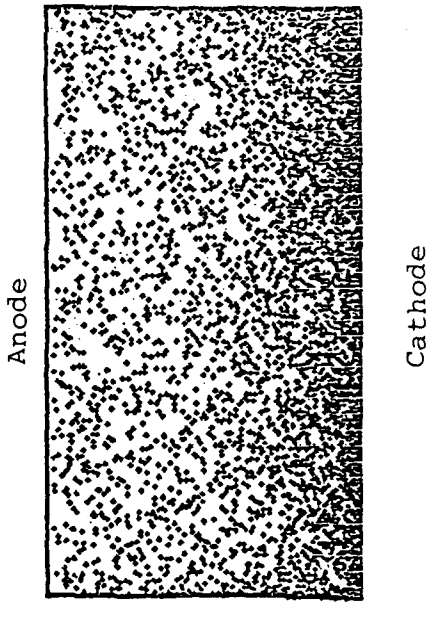

Fig. 7 Electron map in the anode-cathode gap. Applied voltage is 1 volt and the gap is 0.5 cm. This is done for the program check.

A DOMAIN DECOMPOSITION AND OVERLAPPING TECHNIQUE METHOD FOR 3D LARGE SCALE NUMERICAL SIMULATION

Kazuyoshi Miki

Energy Reseasrch Laboratory, Hitachi, Ltd.,
1168 Moriyama-cho, Hitachi-shi, Ibaraki, 316

A direct-solution scheme for numerically solving the 3-dimensional Poisson's problem with arbitrarily shaped boundaries $\nabla \cdot (\lambda \nabla \varphi) = S$ on Ω, $C_1\varphi + C_2 \boldsymbol{n} \cdot (\lambda \nabla \varphi) = C_3$ on $\partial\Omega$, has been developed by using a boundary-fitted coordinate transformation. The scheme also used the technique of decomposing the closed domain Ω into several hexahedron subdomains and then overlapping neighboring hexahedrons to deal with complicated geometries. A large system of linear equations deroved from discretizing the Poisson's equation was solved by suing a biconjugate gradient method with incomplete LU factorization of the nonsymmetric coefficient matrix as preconditioning. The convergence behavior of the different domain decompositions was demonstrated for a numerical experimant. Application to the electrostatic field problem in the electron gun of a color picture tube confirms that the present numerical scheme should provide an efficient and convenient tool for solving many important large-scale engineering problems.

SUBTRACTION TECHNIQUE FOR PLASMA PHYSICS AND EVALUATING NUM ERICAL EFFECTS IN CODES

Viktor K. Decyk

University of California, Los Angeles
Department of Physics,
405 Hilgard Los Angeles, Calif. 90024

(Presented by R.Sydora)

We have developed a technique for simulation of subtle effects in plasmas. This technique consists of performing the simulation twice. The first time one simulates the background plasma, and the second time one uses exactly the same initial conditins plus some small perturbation, such as an extra test charge, or test wave, etc. One then subtracts the results from each of the simulations, to see only the effect of the perturbation. This method has been used to measure precisely the wake field excited by a single electron out of millions. This technique can be applied to new codes in several ways. It can be used as an extremely demanding test to verify that new codes are behaving correctly. It can also be used to explore the physical behavior of new models, where the physical preperties are not well understood beause of numerical approximations used, such as in implicit codes.

NUMERICALLY INDUCED STOCHASTICITY and LONG-TIME BEHAVIOR OF NUMERICAL TRAJECTORIES - SMALL ΔT ANALYSIS

Alex Friedman
Lawrence Livermore National Laboratory
and
Steven P. Auerbach
Berkeley Research Associates

Presented at the
Second US-Japan Workshop on Advanced Plasma Modeling
Nagoya, Japan, March 23-26, 1987.

Numerically Induced Stochasticity

In a one-dimensional anharmonic potential well $\phi(x)$, the period of an orbit is a function of its energy. The true motion in such a well is regular, since energy conservation constrains the velocity v at each value of the coordinate x. Nonetheless, when the orbit is computed numerically, stochastic behavior can result.

We consider simple integrators as *mappings* from (x,v) at one time level to (x,v) at the next. With timestep size Δ and $\phi' \equiv \partial\phi/\partial x$, the leapfrog mover is:

$$v^{n+1/2} = v^{n-1/2} - \Delta\, \phi'(x^n) \;;\quad x^{n+1} = x^n + \Delta\, v^{n+1/2} \;.$$

We linearly interpolate v to time level n, then plot the pair (x^n, v^n). Equivalently, we can write a variant with x,v defined at integer time levels:

$$\tilde{v} = v^n - \frac{\Delta}{2}\phi'(x^n) \;;\quad x^{n+1} = x^n + \Delta\tilde{v} \;;\quad v^{n+1} = \tilde{v} - \frac{\Delta}{2}\phi'(x^{n+1}) \;.$$

In a harmonic well with natural frequency ω_0, the classical leapfrog "dispersion relation" is: $\sin \omega\Delta/2 = \pm\omega_0\Delta/2$, with stability limit $\Delta_c = 2/\omega_0 = (\text{period})/\pi$.

We first noted the phenomenon of numerically induced stochasticity in the potential:

$$\phi(x) = x^2 + \frac{\alpha}{0.25+x^2} \;.$$

For $\alpha > 0.0625$, this well has a central "bump" but is harmonic with natural frequency $\omega_0 = \sqrt{2}$ at large x. We have concentrated on the case $\alpha = 1$ (fig. 1) and begin with a description of the behavior in this double-well potential.

The physical phase plane (fig. 2) consists of closed curves with one separatrix. For small enough Δ ($\lesssim 0.2$), stochastic behavior is limited to orbits near the separatrix which are (analytically) barely trapped in one

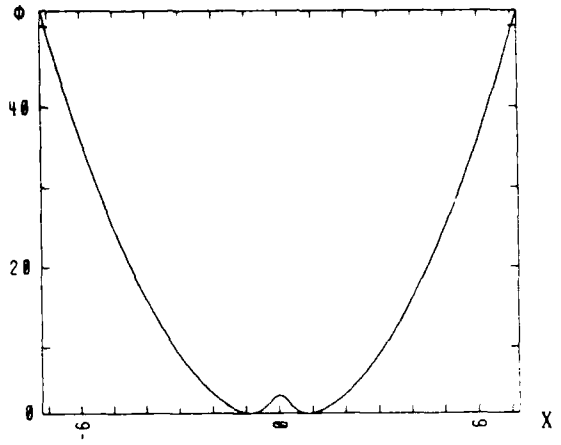

Fig. 1. The double-well potential $\phi(x)$ obtained when $\alpha = 1$.

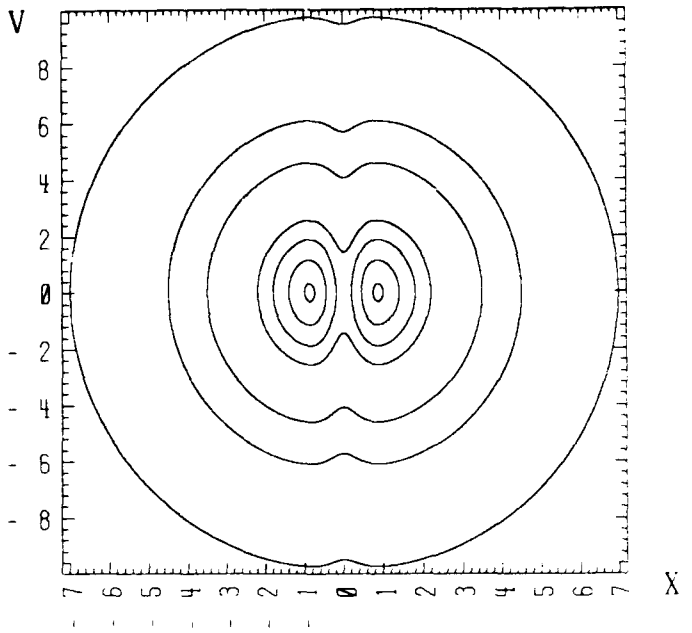

Fig. 2. The (x,v) trajectories of a set of orbits in the potential of fig. 1.

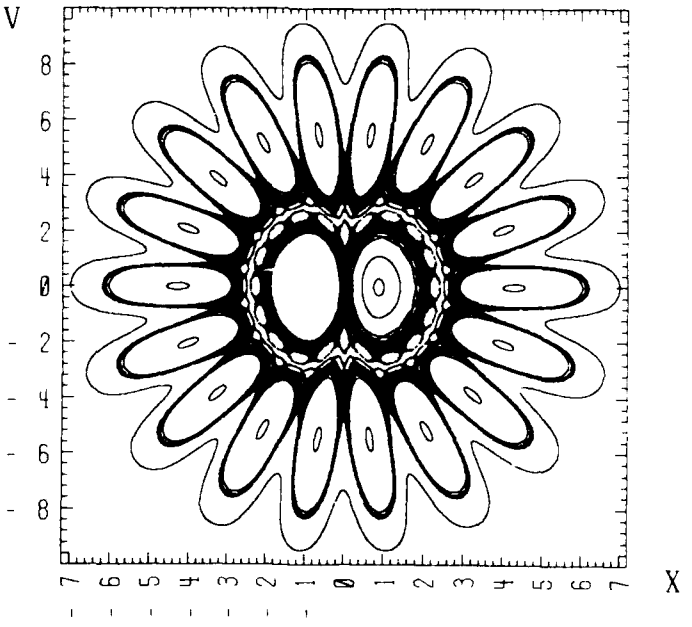

Fig. 3. The (x,v) trajectories of a set of numerically computed orbits in the potential of fig. 1; $\Delta t = 0.25$.

sub-well, or are barely untrapped. There are in addition large trajectory errors (without stochasticity) for orbits which do not carefully sample the central bump.

For larger Δ, a wide range of initial conditions yield a rich stochastic behavior, with a complicated island structure. The situation for $\Delta = 0.25$ is depicted in fig. 3. For small enough energy the motion is confined to a single sub-well and is regular; for intermediate values there is stochasticity; for large values there are large trajectory errors without stochasticity; and for very large energy the central bump is negligible and the motion harmonic (frequency independent of amplitude). These effects occur at timesteps well less than the classical leapfrog stability threshold for the harmonic part of the potential.

Over a large part of phase space (including the region corresponding to "large trajectory errors") we often observe a phase-locking phenomenon; the number of radial oscillations in the locus of points corresponding to an orbit is the nearest integer to the number of steps needed to complete one orbit in the harmonic part of the well. In the run depicted in fig. 3, the harmonic-well period (about 4.44) is 17.77 times the timestep (0.25), and we observe 18 major excursions. When Δ is 0.2, the harmonic period is 22.2 steps, and we observe 22 major excursions. However, while oscillations are still evident at $\Delta = 0.3$, their number is 44, while the harmonic period is 14.8 steps, or a third as long.

Effects of "cantori" are evident in our runs; an orbit often remains trapped in one sub-region of a large chaotic "sea" for a long time before it breaks through to another part of the sea. Runs using single and double precision (Cray-1) arithmetic have been compared; the varying machine roundoff makes the number of steps required to enter the various sub-regions of a large sea differ, confirming that the gaps in the cantori are indeed "found" by the orbit in a random manner. In addition, the island structure is somewhat different, since smaller islands can be resolved in double precision.

We can write the leapfrog mover in a third form most suitable for analysis:

$$x^{n+1} = x^n + \Delta v^n - \Delta^2/2\ \phi'(x^n); \quad v^{n+1} = v^n - \Delta/2\ [\phi'(x^n) + \phi'(x^{n+1})]\ .$$

The Jacobian of the mapping $(x^n,v^n) \rightarrow (x^{n+1},v^{n+1})$ is $J \equiv \partial(x^{n+1},v^{n+1})/\partial(x^n,v^n) = 1$, and thus the leapfrog integrator is an area-preserving map. In fact, the leapfrog motion in the potential well $\phi(x) = A \cos x$ is equivalent[1] to Chirikov's "Standard Map"[2]: $\theta^{n+1} = \theta^n + I^{n+1}$; $I^{n+1} = I^n + K \sin \theta^n$. In the leapfrog scheme as usually written, we redefine $\Delta v^{n+1/2} = V^{n+1}$; then $\Delta v^{n-1/2} = V^n$, and we obtain: $x^{n+1} = x^n + V^{n+1}$; $V^{n+1} = V^n + A\Delta^2 \sin x^n$. Thus, we make the correspondence: $x \Leftrightarrow \theta$; $V \Leftrightarrow I$; $A\Delta^2 \Leftrightarrow K$, and so the Standard Map theory is directly applicable to leapfrog motion in a sinusoidal potential.

The usual Standard Map orbits (fig. 4) are symmetric about neither $\theta = 0$ nor $I = 0$ (i.e., $x = 0$ nor $v = 0$). By replacing the usual leapfrog mover with our variant that defines v at integral time levels, we have synthesized a "Symmetrized Standard Map" (fig. 5) which posesses both of these symmetries and may prove useful in other contexts. In our experience with small-Δ analyses of various movers we have found that simpler power-series expansions result from symmetrized schemes.

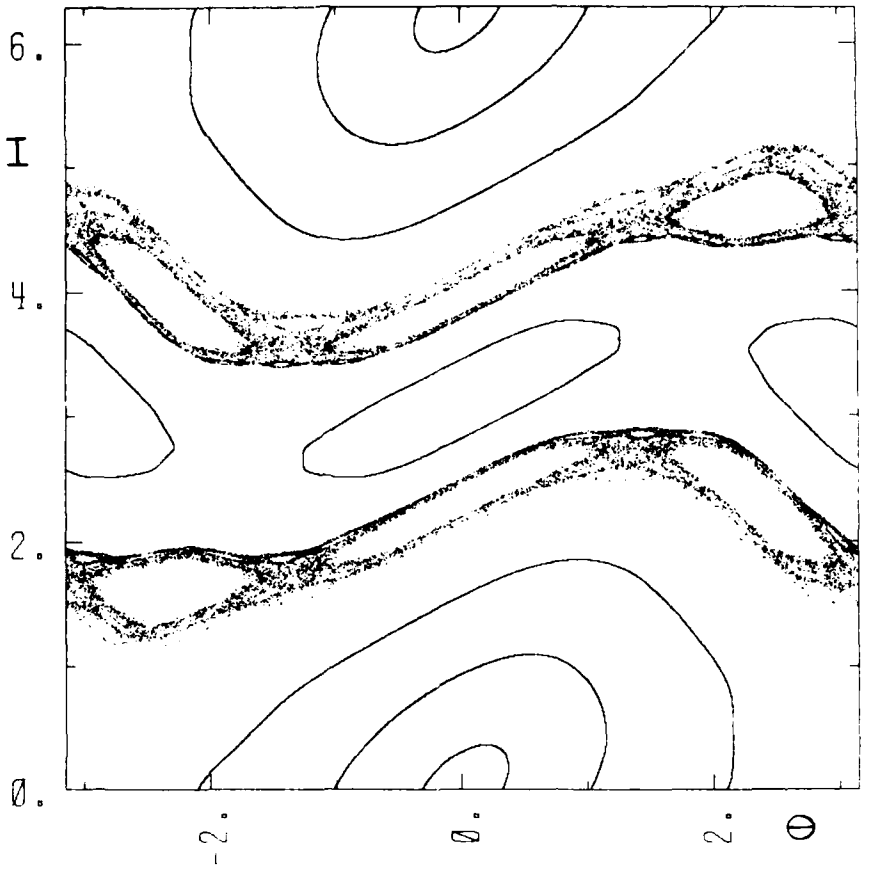

Fig. 4. These Standard Map orbits with K = 1.0 are symmetric about neither $\theta = 0$ nor I = 0 (i.e., x = 0 nor v = 0).

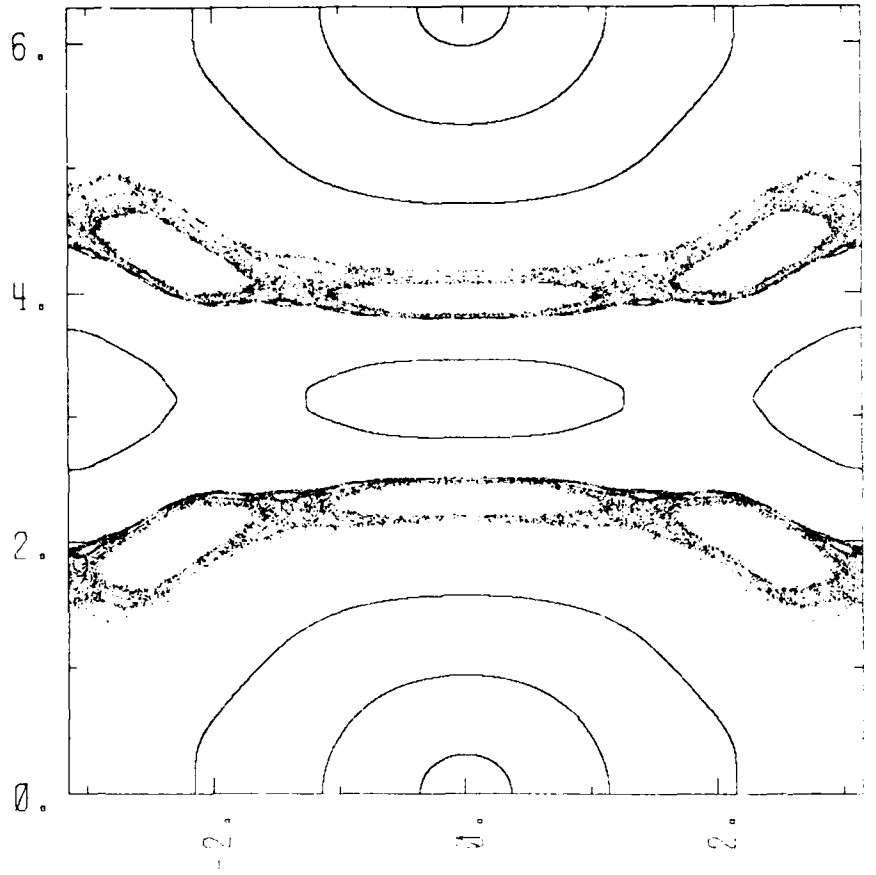

Fig. 5. These "Symmetrized Standard Map" orbits exhibit symmetry about $\theta = 0$ and I = 0.

We have examined other wells, and find that stochasticity is not limited to double wells. For example, the single-well potential $\alpha = 0.0625$ admits a chaotic leapfrog orbit for $\Delta = 0.75$. Chaotic motion is more pervasive in double-wells; it sets in at infinitesimal Δ because the phase plane entails a separatrix even in the absence of finite-timestep perturbations.

We have also examined other particle moving algorithms; the second mover we consider is an implicit, time-centered mover which is stable for all Δ:

$$v^{n+1} = v^n - \Delta/2 \{\phi'(x^{n+1}) + \phi'(x^n)\} \; ; \quad x^{n+1} = x^n + \Delta/2 \{v^{n+1} + v^n\} \; .$$

In a harmonic well with natural frequency ω_0, the dispersion relation is: $\tan \omega\Delta/2 = \pm\omega_0\Delta/2$. With $\alpha = 1$ and $\Delta = 0.25$, this mover exhibits behavior similar to that of the leapfrog. In the "stiff spring" potential $\phi = x^4$ it yields stochasticity for large enough energy and Δ.

The implicit mover is not (locally) an area-preserving map. The Jacobian of the mapping from (x^n,v^n) to (x^{n+1},v^{n+1}) is: $J = [1+(\Delta^2/4)\phi''(x^n)] \; / \; [1+(\Delta^2/4)\phi''(x^{n+1})]$. Note that interchanging x^n and x^{n+1} amounts to changing J into $1/J$, as it must for any "reversible" scheme which retraces its steps if the sign of Δ is reversed. Any change in phase space area due to motion in one direction is made up for when the particle moves in the other direction. Thus, we can expect no net change in phase space area after integration over a complete orbit. For this scheme, the fact that $J \neq 1$ has no global consequences.

Our third mover is a second-order predictor-corrector algorithm:

$$\tilde{x} = x^n + \Delta v^n \; ; \qquad \tilde{v} = v^n - \Delta\phi'(x^n) \; ;$$
$$x^{n+1} = x^n + \frac{\Delta}{2}(v^n + \tilde{v}) \; ; \quad v^{n+1} = v^n - \frac{\Delta}{2}\{\phi'(x^n) + \phi'(\tilde{x})\} \; .$$

This mover yields orbits that don't lie on closed curves even for small timestep. It is not an area-preserving map, and does poorly because the Jacobian of the transformation is always greater than unity: $J \simeq 1 + \Delta^4(\phi'')^2/4$. This can't integrate to zero around an orbit, and so the phase-space area of a given set of initial conditions will grow continuously. Since only $(\phi'')^2$ enters, the orbit will diverge even in a purely harmonic well, with a dispersion relation: $\omega = \omega_0 + (\Delta^2\omega_0^3/6) \; [1 + i\Delta\omega_0]$.

The fourth difference scheme[3] we consider conserves energy identically; it derives from a symmetrized discretization of Hamilton's equations. Let a subscript * denote the advanced time level; the scheme is, for any Hamiltonian $H(q,p)$,

$$\frac{q_* - q}{\Delta} = \frac{1}{2}\left\{\frac{H(q_*,p_*) - H(q_*,p)}{p_* - p} + \frac{H(q,p_*) - H(q,p)}{p_* - p}\right\} \; ;$$

$$\frac{p_* - p}{\Delta} = -\frac{1}{2}\left\{\frac{H(q_*,p_*) - H(q,p_*)}{q_* - q} + \frac{H(q_*,p) - H(q,p)}{q_* - q}\right\} \; .$$

Using such a scheme, the points of a numerically computed orbit will fall on the exact phase plane curves (for a one dimensional Hamiltonian). In a one-dimensional potential well, the Hamiltonian is: $H = v^2/2 + \phi(x)$, and the difference scheme becomes:

$$\frac{x^{n+1} - x^n}{\Delta} = \frac{v^{n+1} + v^n}{2} \; ; \quad \frac{v^{n+1} - v^n}{\Delta} = - \frac{\phi(x^{n+1}) - \phi(x^n)}{x^{n+1} - x^n} \; .$$

By energy conservation, the latter equation can be replaced by:

$$(v^{n+1})^2/2 - (v^n)^2/2 = \phi(x^n) - \phi(x^{n+1}) \; .$$

For most potentials either form must be solved iteratively; for the harmonic oscillator potential the scheme reduces to the centered-implicit one described above. For $\phi(x) = x^2/2$, the orbits are exactly the circles $x^2 + v^2 = 2H$, but there are phase errors which grow, in a single step, by an amount $\simeq -\Delta^3/12$. The Jacobian of the mapping is: $J = (1-\Delta^2 Q/2)/(1+\Delta^2 Q_*/2)$, where $Q \equiv (\phi' - D)/(x_* - x)$, $Q_* = (\phi_*' - D)/(x_* - x)$, and $D = (\phi_* - \phi)/(x_* - x)$. As was the case for the centered-implicit scheme above, interchanging x and x_* changes J into 1/J; the scheme is reversible and thus area preserving on the average.

Other researchers have advocated the use of both energy conserving[3] and symplectic[4] (in 1d, area-preserving) schemes. However, at least in 1d these desirable attributes seem to be incompatible, since the only scheme which satisfies both criteria yields a series of points along the true orbit, within a uniform (same for all orbits) rescaling of the time parameter. Thus, it seems one would need to know the solution in order to devise such a scheme. The energy conserving scheme in 1d has the advantage of making only phase errors, and is at least area preserving on the average, so it has real merit for at least a restricted class of problems; it is still an open question which property is the more useful in higher dimensions.

The phenomenon of numerically induced stochasticity has significance in several contexts. Firstly, a numerical investigation of the regions of phase space accessible to an orbit may lead to erroneous results, if the timestep is too large or the mover inappropriate. Furthermore, conclusions about orbital stability based on numerical integrations may be erroneous, since neighboring chaotic orbits diverge exponentially, even if the chaos is numerically induced. When studying the dynamics of a physical system, one should demonstrate that any chaos observed is not numerically induced. Also, linearized simulations of collective phenomena must avoid numerically induced stochasticity, since the zero-order and perturbed trajectories are "neighboring". Finally, trajectory crossings in PIC simulations can lead to enhanced noise and other errors.[5]

Long-Time Behavior of Numerical Trajectories - Small Δt Analysis

One can construct a "pseudo-energy" which is conserved along the numerical trajectory. We define:

$$\Psi(x,v) = v^2/2 + \phi(x) + \Delta\Psi_1(x,v) + \Delta^2\Psi_2(x,v) \ ,$$

and expand $\Psi(x_*,v_*)$ in a Taylor series using the leapfrog expressions for x_* and v_*. Defining $f = -\phi'$ and keeping terms through Ψ_1,

$$\Psi(x_*,v_*) = \Psi(x,v) + \Delta^2[v\Psi_1' + f\partial\Psi_1/\partial v] + \ldots$$

Thus Ψ is conserved if the derivative of Ψ_1 along the unperturbed orbit is zero :

$$\frac{d\Psi_1}{dt} = v\frac{\partial\Psi_1}{\partial x} + f\frac{\partial\Psi_1}{\partial v} = 0.$$

This differential equation has solution Ψ_1 = constant, so the conserved quantity is just the usual $v^2/2 + \phi$.

Through the next order we find:

$$\Psi(x_*,v_*) = \Psi(x,v) + \Delta^3[\frac{d\Psi_2}{dt} + \frac{vff'}{4} + \frac{v^3f''}{12}] \ ,$$

and thus the equation for Ψ_2 is:

$$d\Psi_2/dt = -vff'/4 - v^3f''/12.$$

With x,v at interlaced times, the first-order term $\Delta\Psi_1$ does not drop out. Ψ_1 satisfies the equation:

$$\frac{d\Psi_1}{dt} = \frac{1}{2}\left(\frac{\partial\phi}{\partial x}\right)^2 - \frac{v^2}{2}\left(\frac{\partial^2\phi}{\partial x^2}\right) \ .$$

For the harmonic oscillator potential $\phi(x) = x^2/2$, we find that:

$$\Psi(x,v) = \tfrac{1}{2}(x^2 + v^2 - \Delta xv) + \ldots \ .$$

This amounts to a skewing of the constant-energy curve in the (numerical) x,v plane due to the leapfrog points being defined at "different times on the orbit".

One can explicitly solve for the $O(\Delta^2)$ correction to the conserved energy. From before, $\Psi_2 = -\int dt\ [\ v\phi'\phi''/4 - v^3\phi'''/12\ ]$. We use:

$$dt = dx/v \ ; \quad v^2 = 2\ (\epsilon-\phi) \ ; \quad \frac{d}{dx}\frac{\phi'^2}{2} = \phi'\phi''$$

to write:

$$\begin{aligned}\Psi_2 &= -\int dx\ [\ \phi'\phi''/4 - v^2\phi'''/12\ ] \\ &= -\int dx\ [\ d(\phi'^2/8)/dx - \epsilon\phi'''/6 + \phi\phi'''/6\ ] \ .\end{aligned}$$

We then use: $d(\phi\phi'')/dx = \Phi\Phi''' + d(\phi'^2/2)/dx$ to write:

$$\Psi_2 = -\int dx \frac{d}{dx}\left\{ \frac{\phi'^2}{8} - \frac{\epsilon\phi''}{6} + \frac{1}{6}(\phi\phi'' - \phi'^2/2) \right\}$$
$$= -\frac{\phi'^2}{24} + \frac{\epsilon\phi}{6}\phi''$$
$$= \frac{v^2\phi''}{12} - \frac{\phi'^2}{24} .$$

Thus, the conserved quantity is:

$$\Psi = \frac{v^2}{2} + \phi + \Delta^2 \left[\frac{v^2}{12}\phi'' - \frac{\phi'^2}{24} \right] + \ldots .$$

Along a numerical orbit, we do indeed find it to be better conserved than $v^2/2 + \phi$.

Using this "Hamiltonian," we can derive an equation of motion which puts the particle on the leapfrog points at integer times, but is smooth in between. Consider x as position, v as canonical momentum:

$$dx/dt = \partial\Psi/\partial v \; ; \quad dv/dt = -\partial\Psi/\partial x.$$

This clearly conserves Ψ on a trajectory:

$$d\Psi/dt = (\partial\phi/\partial x)\, dx/dt + (\partial\Psi/\partial v)\, dv/dt = 0.$$

It also conserves phase space volume; the volume after a time $\Delta = n\delta$ is unchanged (we take n infinitesimal steps each of size δ to get there, then let $n \to \infty$):

$$x(\delta) = x + \dot{x}\delta + \ldots \; ; \quad v(\delta) = v + \dot{v}\delta + \ldots$$

$$J(\delta) = \frac{\partial[x(\delta),v(\delta)]}{\partial[x,v]} = \begin{vmatrix} 1 + \delta\partial\dot{x}/\partial x + \ldots & \delta\partial\dot{v}/\partial x + \ldots \\ \delta\partial\dot{x}/\partial x + \ldots & 1 + \delta\partial\dot{v}/\partial v + \ldots \end{vmatrix}$$

$$= 1 + \delta(\partial\dot{x}/\partial x + \partial\dot{v}/\partial v) + O(\delta^2)$$
$$= 1 + \delta(\Psi_{vx} - \Psi_{xv}) + O(\delta^2)$$
$$= 1 + O(\delta^2)$$

Thus, after a time Δ,

$$J(\Delta) = \frac{\partial[x(\delta),v(\delta)]}{\partial[x,v]} \times \frac{\partial[x(2\delta),v(2\delta)]}{\partial[x(\delta),v(\delta)]} \times \ldots$$

$$= [\, 1 + O(\delta^2) \,] \times [\, 1 + O(\delta^2) \,] \times \ldots$$

There are n terms, so

$$J(\Delta) = 1 + O(n\delta^2) = 1 + O(\Delta^2/n) \to 1 \text{ as } n \to \infty.$$

The equation of motion along this "dynamical" trajectory is explicitly expressible (through order Δ^2) as:

$$dx/dt = v\,(1 + \Delta^2\phi''/6)$$

$$dv/dt = -\phi' + \Delta^2/12\,(\,\phi'\phi'' - v^2\phi'''\,) .$$

Note that we have given up on $dx/dt = v$.

For a second-order equation for x, we find:

$$d^2x/dt^2 = dv/dt\ (1 + \Delta^2\phi''/6) + v\Delta^2/6\ v\phi'''$$

$$= -\phi' + \Delta^2/12\ (\ v^2\phi''' - \phi'\phi''\ ).$$

We compare this with the harmonic oscillator, for which the analytic solution is:

$$d^2x/dt^2 = -\phi'\ (\ 1 + \Delta^2/12\ \phi'' + \ldots\ )\ .$$

Thus, x and v will agree, to order Δ^2, with the leapfrog solution. The "dynamical" trajectory is synchronized with the numerical one.

It is, in fact, true in general that the motion along the "dynamical" trajectory is synchronized with the leapfrog motion through at least order Δ^3. Consider the position as a function of time:

$$x(\Delta) = x + \Delta\dot{x} + \Delta^2\ddot{x}/2 + \Delta^3\dddot{x}/6 + \ldots$$

$$= x + \Delta v(1+\Delta^2\phi''/6) - \Delta^2\phi'/2 - \Delta^3 v\phi''/6$$

$$= x + \Delta v - \Delta^2\phi'/2 + O(\Delta^4)\ .$$

This is the same expression as that for leapfrog. The derivation for v is similar.

ACKNOWLEDGMENTS

This work was performed under the auspices of the U.S. Department of Energy by the Lawrence Livermore National Laboratory under Contract W-7405-ENG-48.

REFERENCES

[1]Ronald H. Cohen, private communication.

[2]A.J. Lichtenberg and M.A. Lieberman, **Regular and Stochastic Motion**, Springer-Verlag, New York, 1983.

[3]Richard H. White, "A Finite Difference Analog for Hamilton's Equations," LLNL Rept. UCRL-78723 (1976); D. Greenspan, "Conservative Numerical Methods for $\ddot{x} = f(x)$," J. Comput. Phys. 56, 28 (1984).

[4]R.D. Ruth, "A Canonical Integration Technique," IEEE Trans. on Nucl. Science NS-30, 2669 (1983); P.J. Channell, "Symplectic Integration Algorithms," Los Alamos National Laboratory Accelerator Theory Note AT-6:ATN-83-9 (1983); V.K. Decyk and C.R. Menyuk, "Discrete Hamiltonian Particle Simulation," Proc. US-Japan Workshop on Advanced Plasma Modeling, IPP Nagoya, Sept. 24-7 1985.

[5]H.R. Lewis, D.C. Barnes, and K.J. Melendez, "The Liouville Theorem and Accurate Plasma Simulation," J. Comput. Phys. 69, 267 (1987).

REDUCED ATOMIC MODEL FOR CALCULATION OF CHARGE STATE DISTRIBUTION IN MULTIPLY-CHARGED PLASMAS

Takashi YABE

Institute of Laser Engineering, Osaka University

Suita, Osaka 565, Japan

ABSTRACT

A method to treat particle production and annihilation in paricle code is proposed. This method does not directly produce particles and hence can be used with less noise. An example is given for a beat wave accelerator. The density change of 0.06 % during one plasma period can seriously affect the excitation of plasma waves. In addition, a new method to economically solve atomic processes is proposed, which can be coupled with particle codes. Finally, the coupling between non-LTE free and bound electrons is analyzed with a simple analytical model and its importance in real systems is pointed out.

I. INTRODUCTION

In fusion plasmas, there exist many application

fields in which bound electrons inside an atom is not in LTE(Local Thermodynamic Equilibrium). The non-LTE treatment needs a solution of coupled rate equations and hence is extremely difficult in high-Z plasmas. Recently, we have developed a new atomic model[1] in which both charge state distribution and level populations are economically calculated. This model enables us to incorpolate the non-LTE calculation into the hydrodynamic processes and has been applied to the X-ray production from laser-heated Au plasmas[2].

Although the non-LTE treatment of bound electrons has been addressed in many studies, free electrons have been assumed to be in LTE-Maxwell-Boltzmann distribution. However, we find that there exist a wide parameter range in which the cross section of free-free binary collision is much less than that of the electron impact ionization. In such a case, even free electrons should be described in non-LTE. There have been an attempt to do this[3], but the electron distribution function was given outside and the modification of the distribution owing to the atomic process was not considered.

In this paper, we discuss the possibility to establish a new particle model to describe non-LTE free electrons incorpolating interactions with non-LTE bound electrons : ionization and recombination. In section II, we propose a simple algorithm to treat an-

nihilation and production of particles. In section III, this scheme coupled with a relativistic electromagnetic particle code, which is essentially the same as ZOHAR[4], is applied to a beat wave accelerator[5,6]. In section IV, the review of recent atomic models are given. In section V, the coupling between the atomic process and the particle distribution is treated by a simple model and the model is applied to a problem on heat flux in laser-produced plasmas.

II. PARTICLE CODES WITH ANNIHILATION AND PRODUCTION

Particle codes have been used in many areas ; electromagnetic particles in plasma physics, gas particle in astrophysics, fluid particles in fluid mechanics and so forth. The code can be easily implemented and is tolerable in large distortion or disturbance. In these applications, however, there have been little attempt to incorpolate the annihilation and production of particles in the codes. This is because the annihilation and production of particles require inefficient and tedious caculations and sometimes cause a serious noise. In this section, we propose a simple algorithm to incorpolate the above process into particle codes.

In most cases, a particle is produced at some

point having a velocity distribution. Let us define the production rate of this disctribution by df(x,v)/dt. In order to replicate this production, a number of particles must be generated ; velocity distribution must be replicated. Furthermore, if df/dt is quite small, a particle will be generated very rarely or discontinuosly leading to noise because mass of generated particle cannot be small ; if the particle mass is taken to be small, number of particles generated will be extremely large. In the present scheme, the particle is not directly generated. Instead of generating directly the paricles, the produced particles are stored into a cell as in a form of a velocity distribution $f_i(v)$, which is advanced in time as

$$f_i^{n+1}(v)=f_i^n(v)+df(x_i,v)/dt.\Delta t, \qquad (II-1)$$

where x_i is the location of the i-th cell center and n denotes the time step, and Δt is the increment of the time step. The distribution does not propagate in space and has no response to forces generated or imposed. In our algorithm, new particles will not be produced unless the severe condition described later is met. Instead of generating new particles, the mass of existing particles which are in the i-th cell are increased by the following procedure;

$$N_p^{new}(x_p,v_p)=N_p^{old}(x_p,v_p)+\alpha f_i^{n+1}(v_p)\Delta v, \quad (II-2)$$

where x_p and v_p are the location and velocity of the

particle, and Δv is the velocity volume ; f_i is divided into many cells in velocity space. In turn, the stored particle decreases according to

$$f_i^{new}(v_p)=(1-\alpha)f_i^{n+1}(v_p), \qquad \text{(II-3)}$$

in one time step. In the example given in section III, α is set to 1 or 0 (see also Eq.(II-4)).

We should impose the maximum and minimum size, N_{max} and N_{min} on the particles. N_{max} avoids too large particle which may become a source of noise. Then

$$\alpha = 0 \quad \text{if } N_p^{new} > N_{max} \qquad \text{(II-4)}$$

Once the mass increase stops as in Eq.(II-4), $f_i(v_p)$ corresponding to this particle may increase intolerably. This situation is unavoidable, particularly for cold streaming electrons in uniform ion background ; some of these beam electrons collide with bound electrons inside ions and a new "non-drifting" electron should appear. Since there is no electron in this velocity range, a new particle must be generated. However, if f_i is used, this procedure can be simply performed. Thus, if $f_i(v_p)\Delta v \geq N_{min}$, a particle having v_p and N_{min} is generated inside the i-th cell.

Annihlation of particles is very simple in this procedure. It should be noticed that a particle will not disappear even if $N_p < N_{min}$.

The only problem is how to store this distribution with less computation memory ; space times velocity dimensions is required.

III. APPLICATION TO BEAT WAVE ACCELERATOR

In this section, we give a very simple application of the procedure given in the previous section. That is a beat wave accelerator[5,6]. There have been a number of particle simulations on this problem, while none has incorpolated ionization effects into the particle code. In some of experiments on the beat wave accelerator, medium-Z materials are used as a plasma source. Even in this medium-Z plasmas, ions may not be fully ionized. During the heating of plasmas, the ion density gradually increases in time. Although the rate of density change is very small, it can affect the excitation of plasma waves. This was first pointed out by J.P.Matte *et al.*[7].

It is well known that plasma waves excited by beat wave saturate because of a relativistic detuning[6]. This is due to the increase of $\gamma = [1-(v/c)^2]^{-1/2}$, where v and c are the speeds of a particle and light, respectively. The idea by J.P.Matte *et al.* is to compensate this reduction of plasma frequency by increasing the ion density through ionization. This change in $\delta\omega_p$ is approximately written[8] as

$$\delta\omega_p/\omega_p = -1/2\ (9a_1a_2/8)^{2/3} \qquad \text{(III-1)}$$

where a_1, a_2 ($\ll 1$) are the normalized quiver

velocities $eE_1/(m\omega_1 c)$, $eE_2/(m\omega_2 c)$. Hence the density change δn which compensates for the change given by Eq.(III-1) should be

$$\delta n/n = (9a_1a_2/8)^{2/3} \qquad \text{(III-2)}$$

Since the time to saturate is

$$\omega_p \tau_s = (4/3^{1/3})(a_1a_2/4)^{-2/3}, \qquad \text{(III-3)}$$

the rate of density change is

$$\delta n/n\omega_p \tau_s = (3^{1/3}/4)(9/32)^{2/3}(a_1a_2)^{4/3}. \qquad \text{(III-4)}$$

For CO_2 laser (10.6 and 9.6 μm) at $10^{14}W/cm^2$, a_1a_2 = 0.0074 and hence Eq.(III-2) gives $\delta n/n$ = 0.04. This indicates that this small change of density can affect the excitation of plasma waves.

Since $\omega_p \tau_* = 184$ and $\delta n/n\omega_p \tau_s = 2.2\times10^{-4}$, the density changes by only 0.022% in one plasma period (ω_p^{-1}). However, even this small change can be successfully described with the algorithm given in section II.

Let us give an example ; $a_1=a_2=0.1$, $\omega_1/\omega_p=10.9$, $\omega_2/\omega_p=9.9$, the system size is $6.35c/\omega_p$, total spatial meshes 256. The initial electron temperature is $m_ec^2/25$. The ejected electrons through ionization are stored into $f_i(v)$ as in Eq.(II-1) ; the velocity space is divided inot 10x10 meshes for the range $-1 \leqq v_x/c$, $v_y/c \leqq 1$. N_{max} and N_{min} are set to $2.0N_0$ and $0.5N_0$, N_0 being the initial particle mass.

Figure III-1 shows the time evolution of particles in phase space (x,u_x) ; this is the case without ionization. Figure III-2 shows the time

evolution of the maximum electrostatic potential induced by beat wave ; III-2a and 2b correspond to the cases without and with ionization, respectively. In the latter case, ionization rate $\delta n/n\omega_p\tau$ is 6.25 x 10^{-4}, whereas the value given by Eq.(III-4) is 3.33 x 10^{-4}. As clearly seen from these figures, even this small change of the density can seriously modify the beat wave acceleration. This may also be true for the induced Raman process in laser-produced plasmas.

IV. ATOMIC PROCESS

In this section, the method to solve atomic processes is briefly reviewed. The basic equations for those processes are the rate equation for the population $N_{Z,n}$ of an ion in charge state Z with an excited electron in the n-th level;

$$dN_{Z,n}/dt = -\sum_m I_{Z,n;Z+1,m} N_{Z,n} N_e - \sum_k R_{Z,n;Z-1,k} N_{Z,n} N_e + \sum_{m'} I_{Z-1,m';Z,n} N_{Z-1,m'} N_e + \sum_{k'} R_{Z+1,k';Z,n} N_{Z+1,k'} N_e$$
$$- \sum_l E_{Z,n;Z,l} N_{Z,n} N_e - \sum_s D_{Z,n;Z,s} N_{Z,n} + \sum_s E_{Z,s;Z,n} N_{Z,s} N_e + \sum_l D_{Z,l;Z,n} N_{Z,l} , \qquad (IV-1)$$

This equation is not economical when it is coupled to other equations which determine the plasma parameters.

In practice, it is better to use an approximation to this equation and to make it realistic. There exist three approaches at hand. The first one is the average ion model[9,10], where $N_{Z,n}$ is averaged over Z and then it is sufficient to solve only the equations for the level populations of an average atom. The equation to be solved in this case is

$$d(NP_n)/dt = R_n N_e N Q_n - I_n N_e N P_n + N\left[\sum_{m>n} A_{nm} P_m Q_n - \sum_{m'<n} A_{m'n} P_n Q_{m'}\right] + \sum_{m>n} C^D_{nm} N_e N P_m Q_n$$
$$- \sum_{m'<n} C^D_{m'n} N_e N P_n Q_{m'} + \sum_{m<n} C^U_{nm} N_e N P_m Q_n - \sum_{m'>n} C^U_{m'n} N_e N P_n Q_{m'} , \qquad (IV-2)$$

The derivation of this equation is described in Ref.1 in detail.

As an alternative approach, if a suitable assumption for the populations of the excited level can be

made, the equations required to be solved are those for N_z only; N_z being the abundance of the ion Z. The equation for this is

$$dN_z/dt = -I_z N_z N_e - R_z N_z N_e + I_{z-1} N_{z-1} N_e + R_{z+1} N_{z+1} N_e , \qquad \text{(IV-3)}$$

In this direction, Salzmann and Krumbein[11] proposed a form of the excited-level population such as

$N_{z,s}/N_z = N_0 A \exp(-E_{z,s}/kT)$ for excited levels

$N_{z,s}/N_z^* = N_0$ for a ground level

where A is so chosen that the population becomes close to the value calculated by a detailed rate equation. Here, N_0 is determined from $\Sigma_s N_{z,s}/N_z = 1$ and $E_{z,s}$ is the level energy. However, this is not always possible for high-Z plasmas, since we have no method to determine the adjustable parameter A. Busquet proposed a mixed model where only relatively lower excited levels are calculated by the rate equation whereas highly excited levels are assumed to be of the Boltzmann type. However, he needed a further approximation in the coronal limit.

The third approach is the hybrid atom model[1] developed recently, which is a combination of the former two methods. The basic principle of this approximation comes from the fact that transitions between bound states proceed faster than those between free and bound states. Hence, the level populations

of the excited levels can be approximately estimated by quasisteady equations of bound-bound transitions for an ion of charge Z:

$$N_{z,n}/N_{z,m} \simeq (A_{nm}+C^{D}_{nm}N_e)/(C^{U}_{mn}N_e) = (g_n/g_m)F(E_m,E_n,N_e)\,, \qquad \text{(IV-4)}$$

Equation (IV-4) shows that the normalized population $N_{z,n}/g_n$ can be estimated if only the level energy E_n is known. Although there exist transition processes which may destroy the above characteristics, Eq.(IV-4) motivates us to use an energy-functional form of the normalized population $N_{z,n}/g_{z,n}$: if $N_{z,n}/g_{z,n}$ is only a function of level energies and does not depend explicitly on Z, the normalized populations constructed from the average ion can be rescaled and used for other ions in a different charge state. It should be noticed that we do not use Eq.(IV-4) but use Eq.(IV-2) in the hybrid atome model.

In order to clarify the idea in detail, let us examine the level dynamics of various ions by solving the full rate equation (IV-1) for an aluminum plasma ; it is possible to solve (IV-1) in such a low-Z plasma. In Fig.IV-1, the reduced population probability $W_{z,n}/g_{z,n}$ (= $N_{z,n}/g_{z,n}N_z$, $\Sigma_n W_{z,n}=1$) is plotted versus the excitation energy, which means the level energy measured from the ground-state level. For $N_i=10^{20}$ cm^{-3}, the probability is close to the Boltzmann type

$W_{z,n}=g_{z,n}\exp(-E_n/kT_e)$. Although for $N_i=10^{18}$ cm^{-3} it is also close to the Boltzmann type, the temperature of the bound electrons is much lower than the free electron temperature T_e. In each case, the reduced probability for various ions of +3 to +10 can be well characterized universally by one curve, although this curve depends on the physical parameters as shown by two curves in Fig.(IV-1a).

If this characteristic is taken into account, the common behavior appearing in Fig.(IV-1a) can be satisfactorily described by the average-ion model. Actually, the reduced electron population probability defined later shows the same characteristics as shown in Fig.(IV-1b). Accordingly, once the electron population P_n of the average ion is obtained from Eq.(IV-2), the function $Y_a(E)$ (the reduced electron-population probability) is constructed from P_n as follows ; at some discrete points

$$Y_a(E_n^a) = P_n/g_n\Sigma\, {}_nP_n \quad (n=1,2,\text{--}n_{max}) \qquad \text{(IV-5)}$$

and in other regions $Y_a(E)$ is exponentially interpolated from Eq.(IV-5) : this exponential interpolation is justified by the characteristics appearing in Fig.(IV-1). In Eq.(IV-5) E_n^a is the excitation energy of the average ion and the summation is taken over the ionizing shells. This energy-functional form can be used to generate the population probability even for the ion in a charge state Z different from Z^a of the

average ion :

$$W'_{z,n}=Y_a(E)g_{z,n}. \qquad \text{(IV-6)}$$

It should be noticed that the physical meaning of $W'_{z,n}$ in Eq.(IV-6) differs from $W_{z,n}$ in Fig.(IV-1a) : the former is derived from the electron population but the latter from the ion population $N_{z,n}$. However, both characteristics are similar as seen from Figs.(IV-1a) and (IV-1b). This can be justified by remembering the nature of the average ion model and CR (Collisional-Radiative) model. In the CR model, only one electron is excited in some level. Accordingly, if ions in various charge states are collected together into a fictitious ion, the electron population P_n in the n-th level of this ion will reflect the ion population of the original "real" ions $N_{z,n}$ with an electron in the n-th level.

In the next step, the ionization and recombination rate coefficients are summed up with respect to n using N_z and $W_{z,n}=W'_{z,n}$. Then Eq.(IV-3) for N_z is solved. With this model, all regions including LTE, corona, and those intermediate to them can be described without any adjustable parameter.

Since Eq.(IV-3) is in a tridiagonal form, the numerical procedure to solve it is quite easy. In the present model the main computation time becomes the time to solve only Eq.(IV-2) and is computationally as fast as the average-ion model. If the ionic charge

becomes large, then the validity of the present model is much improved because the range of Z that satisfies $\varepsilon = |Z-Z^a|/Z^a << 1$ becomes wider and the fractional energy change ($\Delta E/E$) for these ions is on the order of ε ; this small change of energy justifies the interpolation in constructing the energy funcion Y_a.

In order to justify the model, let us give an example. Figure (IV-2) shows the relative abundance of the charge state of aluminum at a steady state for $N_i = 10^{20}$ cm^{-3} and various electron temperatures. Here, the rate equation [Eq.(IV-3)] for N_z includes radiative, three-body, and dielectric recombinations, and collsional ionization. In addition, collisional excitations and deexcitations, and radiative deexcitations, are also included in the average-ion model [Eq.(IV-2)]. The results predicted by the hybrid atom model [Eqs.(IV-2) and (IV-3)](solid line) agree quite well with those given by Duston et al.[13] (CR model shown by the dashed line) for $Z \gtrsim 10$. In Ref.13, only levels for $Z \gtrsim 10$ were calculated by the rate equation, whereas for $Z<10$ ions only the ground-state levels were taken into account. The small difference (about 40% at most) between the CR model and our hybrid-atom model is within difference caused by the different rate coefficients.

The superiority of the hybrid atom over the average atom appears in the calculation of radiation

transport in high-Z plasmas. Figure IV-3 illustrates the main feature of this process. Let us consider x-ray emission at some spatial point x_1 and absorption at x_2. In the average-ion model, only one fictitious ion having Z^* exists at each space point, so that the level energy and hence the x-ray spectral energy changes from space point to space point depending on the average charge Z^* which follows physical parameters, the density and the temperature. Consequently, the line radiation emitted in one region can not be absorbed by the same spectral line in another region as shown in Fig.IV-3(a). In actual plasmas, however, there exists an ion having the same charge Z in all regions although the abundance N_z may change from space point to space point. This means that a spectral line emitted in one region is always absorbed by the same line in any other region of space as shown in Fig.IV-3(b). The hybrid-atom model can describe this process.

The line shift due to change of Z is significant in high-Z material because the energy difference between Z and Z+1 ions is about $2I_H Z/n^2$ and hence is about 50 eV for Z=30 and n=4, I_H being 13.6 eV. This value is far beyond the line width broadening. The result[1] with the hybrid-atom model indicates that the charge state of Au plasmas distributes over a relatively large width in Z (Δ Z=5). This result also

agrees with the experimental data[14]. The real lines may spread over 300-400 eV (n=4) in spectral range ; the line of the average ion may locate at the center of this group of lines.

As a simple example, we solve line transfer equation as well as the atomic process. We use exponential profiles for the density and temperature in space making the pressure uniform : the density and temperature ranges from 16×10^{20} to 1×10^{20} cm^{-3} and 100 to 1600 eV. The scale length of these plasmas is 10 μ m. Figures IV-4(a) and 4(b) are obtained from the average-ion model and the hybrid-atom model, respectively. In addition to the atomic processes given above, photoexcitations and radiation transport are included[1]. In the figure, the solid curves are the results in which the energy space is divided into groups of 5 eV width and line broadenings by various processes are neglected for simplicity : one curve is the direct data and another is further averaged over 50 eV for an illustrative purpose. In Fig.IV-4(a), in addition to the above curves, we draw the dashed curve that is the result using the groups of 50 eV width broadened artificially. The comparison between the solid curves in Fig.IV-4(a) and 4(b) shows that the emission intensities and hence opacities with the hybrid-atom model are larger than those with the average-ion model. The difference is concluded to

arise from the charge-state distribution illustrated in Fig.IV-3. It is possible to approximately incorpolate this effect into the average-ion model. If the line width is artificially broadened over the range determined from the charge state distribution as in Fig.IV-4(a) (dashed curve), the result comes closer to that with the hybrid-atom model.

V. COUPLING BETWEEN NON-LTE FREE AND BOUND ELECTRONS

In this section, we will describe an example of coupling between free and bound electrons both in non-LTE state. In order to clarify the physics, the model is largely simplified. However, its basic principle can be used in the particle code described in section II.

In the formulation of section IV and Ref.1, free electrons are assumed to be in LTE. This assumption appears in the rate coefficient R as follows;

$$R=\langle \sigma\, v\rangle = \int \sigma\, v f v^2 dv, \qquad (V\text{-}1)$$

where σ is the cross-section and f the velocity distribution function of free electrons ; f is normalized to satisfy

$$\int f v^2 dv = 1, \qquad (V\text{-}2)$$

and is taken to be the Maxwell distribution in LTE. In this section, however, we determine this distribution function.

It is easy to derive the rate of change in the number of free electrons owing to radiative capture ; the number of free electrons captured within a velocity width Δv at v is given by $(\delta R/\delta v)\Delta v N N_e = \sigma_R f v^3 \Delta v N N_e$. On the contrary, the expression for the impact ionization is more complicated because there are three terms in this process ; 1) velocity change

from v to v' of a projectile electron , 2) from v' to v of the same electron, and 3) the birth of a free electron with v (ionization). If we denote the initial and final velocities of the free electron, and an emerging electron velocity by v_i, v_f, and v_b, respectively, the energy conservation requires

$$v_i^2 = 2I/m_e + v_f^2 + v_b^2, \qquad (V-3)$$

where I is the ionization energy. Since the cross section of binary collision between free electrons is much larger than that of impact ionization at low energy (close to ionization energy I, see Fig.V-1), we need not to take into account the third process (birth of an electron) ; the ejected electron may quickly thermalize through binary collision which can be described as $-\nu (f-f_M)$, where f_M is the equilibrium Maxwell distribution. ν is given by $\sigma_{ee} v N_e$ where σ_{ee} is the cross section of free-free collision.

Furthermore, we can also assume $I/m_e \ll v_i^2, v_f^2$. Thus, we get an approximate equation ;

$$df/dt=-\sigma_R v N_e f(v)+\sigma_I v' N_e f(v')-\sigma_I v N_e f(v) - \nu(v)(f-f_M) \qquad (V-4)$$

where v' is the initial velocity of a projectile electron. If we set $v'=v+\langle \Delta v \rangle$ and expand Eq.(V-4) in $\langle \Delta v \rangle \ll v, v'$, then we get

$$df/dt=-\sigma_R v N_e f+\sigma_I \langle \Delta v \rangle N_e \partial(fv)/\partial v - \sigma_{ee} v N_e (f-f_M). \qquad (V-5)$$

where $\langle \Delta v \rangle$ can be approximately given by $I/m_e v$.

As inferred from the relative magnitude of σ in Fig.V-1, the electrons having high energy may be much affected by ionization σ_I. Figure V-2 shows the nearly quasi-steady solution of Eq.(V-5) for Au plasmas at T=1keV, Z*=41. This change of velocity distribution is quite serious in calculating the thermal flux and other transport coefficients.

Acknowledgement

The author would like to thank Dr.K.Mima at ILE and Dr.T.Kamimura for valuable suggestions and discussions.

REFERENCES

1) M.Itoh, T.Yabe, and S.Kiyokawa, Phys.Rev.**A35** (1987) 233.

2) T.Mochizuki *et al.*,IAEA-CN-47/B-I-3,Kyoto, Japan, Nov.(1986).

3) M.Lamoureux, C.Moller, and P.Jaegle, Phys.Rev. **A30** (1984) 429.

4) A.B.Langdon and B.F.Lasinski, in "Methods in Computational Physics" Vol.16(19??)327.

5) T.Tajima and J.M.Dawson,Phys.Rev.Lett.**43**(1979)267.

6) M.N.Rosenbluth and C.S.Liu, Phys.Rev.Lett. **29** (1972)701.

7) J.P.Matte, private communication.

8) C.M.Tang, P.Sprangle, andR.N.Sudan, Phys.Fluids **28** (1985)1974.

9) W.A.Lokke and W.H.Grasberger, Lawrence Livermore National Laboratory Report, UCRL-52276, 1977.

10) S.Kiyokawa, T.Yabe, and T.Mochizuki, Jpn.J.Appl. Phys. **22**(1983)L772.

11) D.Salzmann and A.Krumbein, J.Appl.Phys. **49**(1978) 3229.

12) M.Busquet, Phys.Rev. **A25** (1982) 2302.

13) D.Duston and J.Davis, Phys.Rev. **A21** (1980) 1664.

14) S.Kiyokawa, T.Yabe, N.Miyanaga, K.Okada, H. Hasegawa, T.Mochizuki, T.Yamanaka, C.Yamanaka,

and T.Kagawa, Phys.Rev.Lett. 54(1985)1999.

FIGURE CAPTIONS

Fig.III-1 : Phase space plot of particles at $\omega_p t$ = 0(top), 100(middle), and 200(bottom).

Fig.III-2 : Time evolution of electrostatic potential (a) without and (b) with ionization.

Fig.IV-1 : The reduced population probability vs the excitation energy for T=50 eV and (i) N=10^{20} cm^{-3} and (ii) N=10^{18} cm^{-3}. (a) The reduced ion population probability vs the excitation energy with CR model for different charge states of ions. (b) The reduced electron population probability vs the excitation energy with the average-ion model.

Fig.IV-2 : The dependence of aluminum abundance in various charge states on electron temperature for an ion density of 10^{20} cm^{-3}. The solid and dashed lines are the results from the hybrid-atom model and collisional-radiative model, respectively.

Fig.IV-3 : The difference between the radiation transport in (a) average-ion model and (b) hybrid-atom

model.

Fig.IV-4 : The emitted x-ray intensity vs photon energy from a typical laser-produced Au plasma. (a) average-ion model, (b) hybrid-atom model.

Fig.V-1 : Comparison between free-free and bound-free collisions ; here T=I is assumed. When T<I, free-free cross section becomes steeper and shifts towards left. ζ is the number of bound electrons.

Fig.V-2 : Quasi-steady solution of Eq.(V-5) for Au plasmas at T=1 keV, Z^*=41. Dashed line shows the Maxwell distribution at T=1 keV.

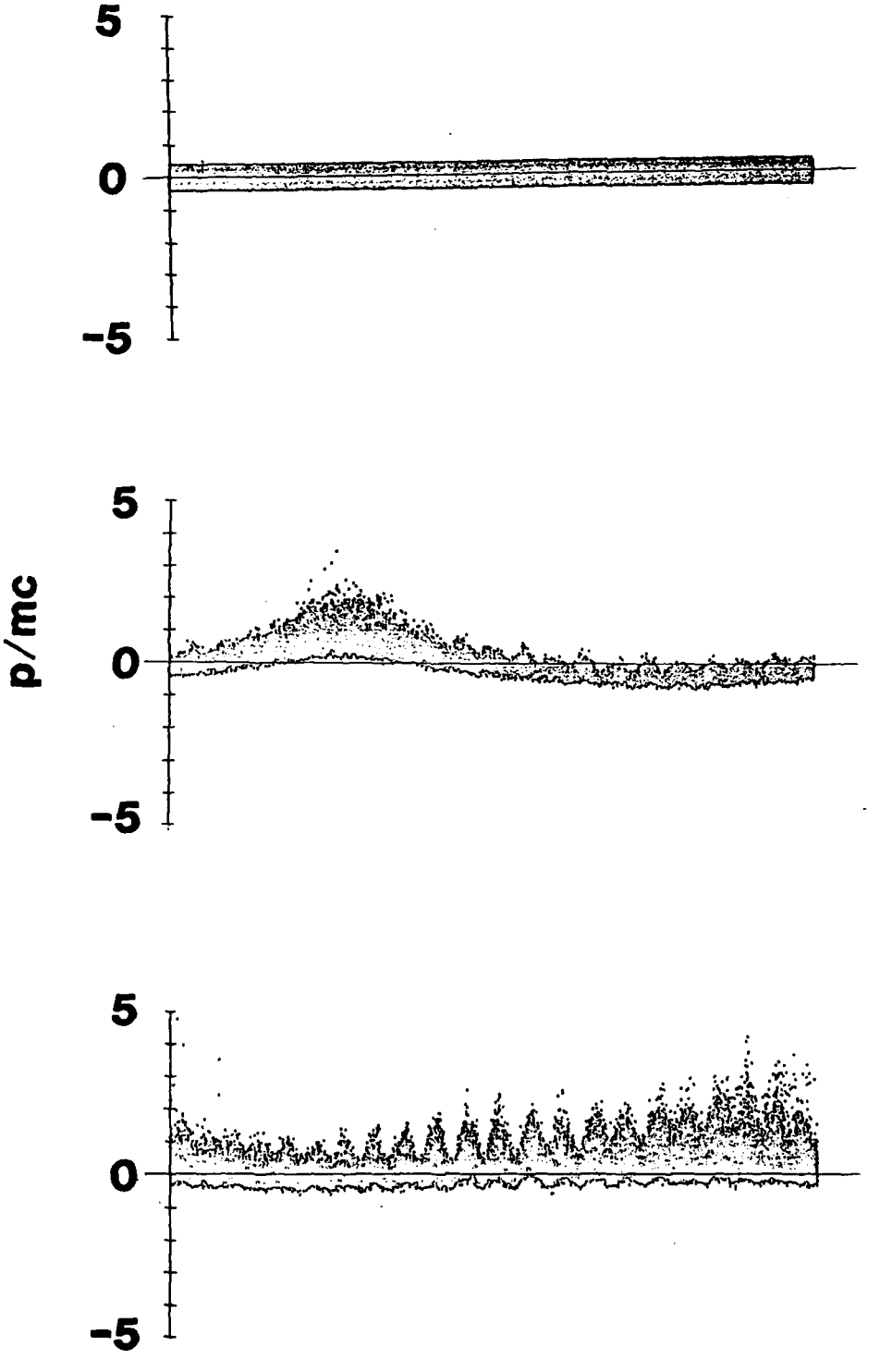

Fig.III-1

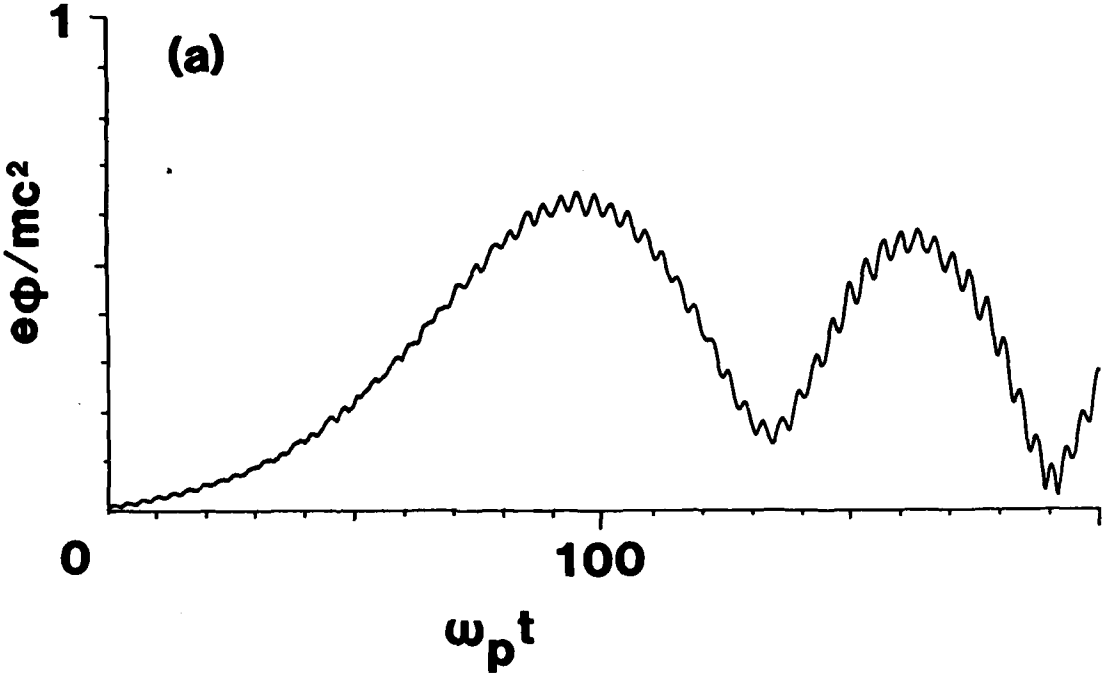

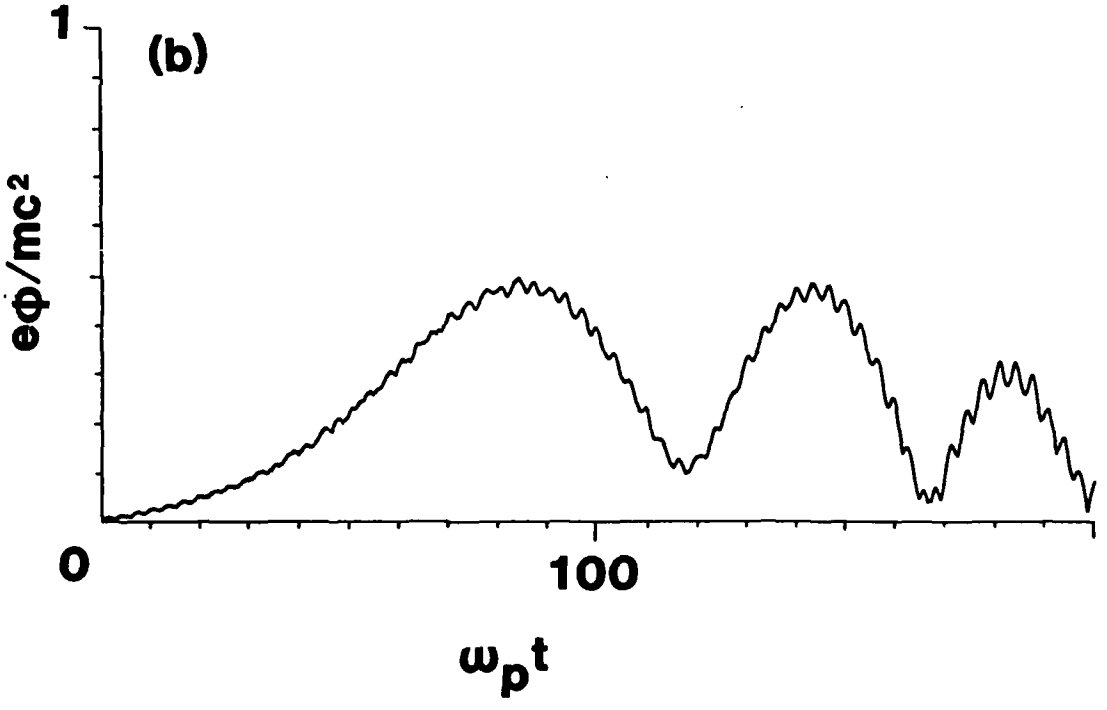

Fig.III-2

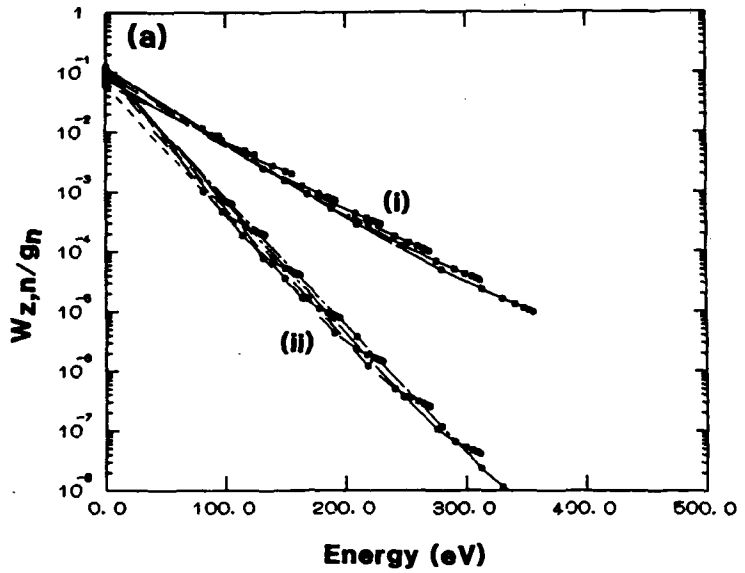
(a)
(i)
(ii)
$W_{z,n}/g_n$
Energy (eV)
0. 0
100. 0
200. 0
300. 0
400. 0
500. 0

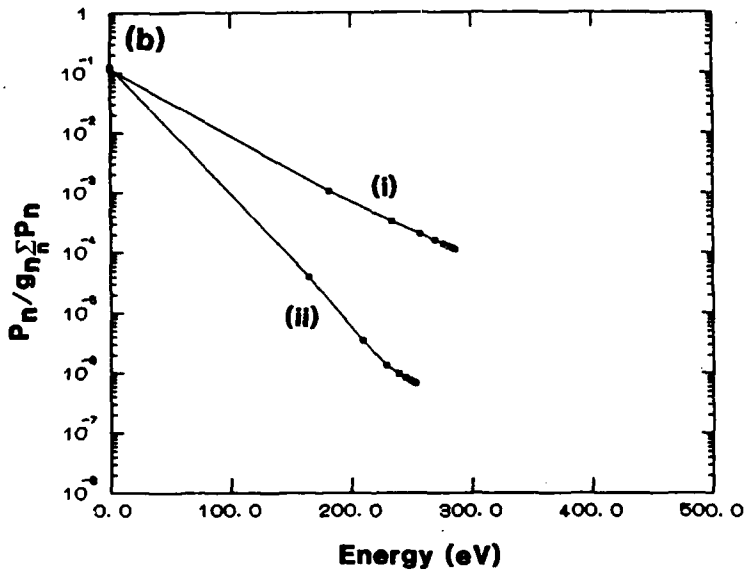
(b)
(i)
(ii)
$P_n/g_n\sum_n P_n$
Energy (eV)
0. 0
100. 0
200. 0
300. 0
400. 0
500. 0

Fig.IV-1

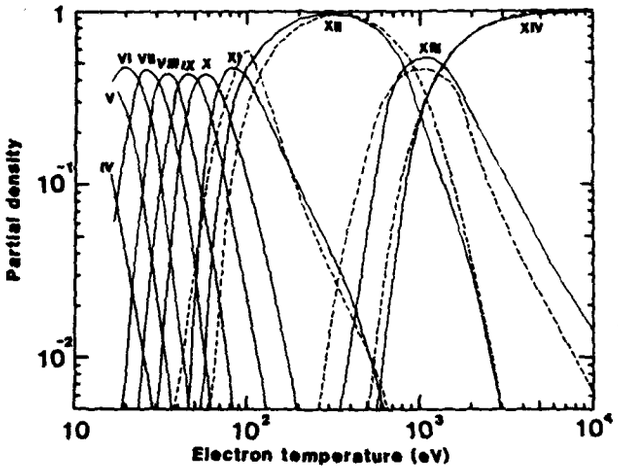

Fig.IV-2

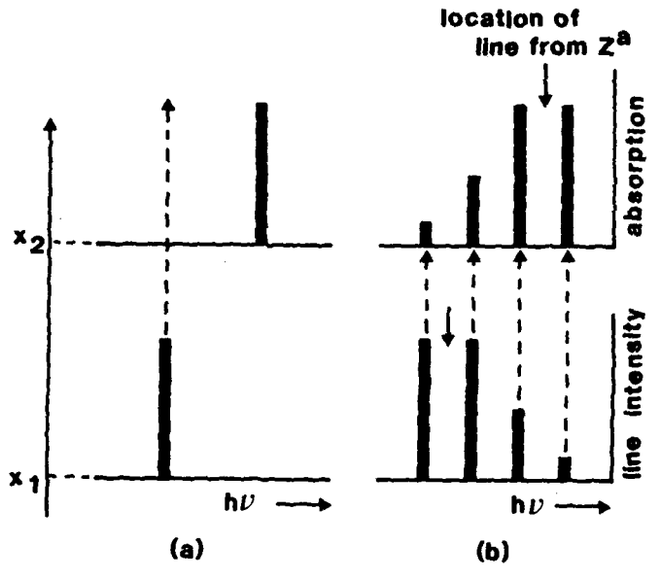

Fig.IV-3

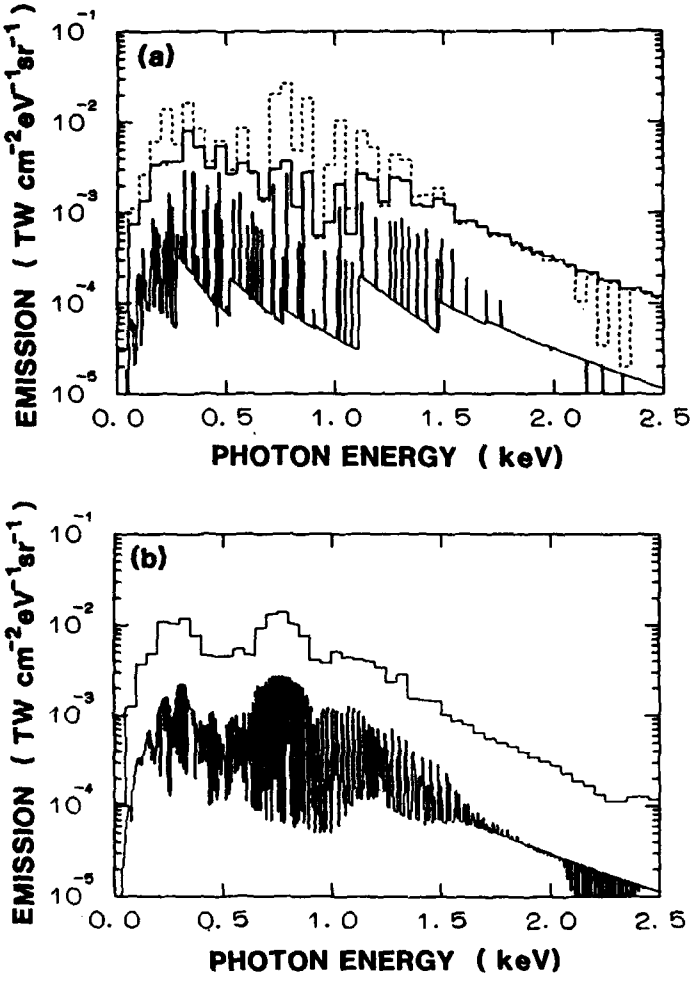
(a)
EMISSION (TW cm^{-2}eV^{-1}sr^{-1})
10^{-1}
10^{-2}
10^{-3}
10^{-4}
10^{-5}
0.0
0.5
1.0
1.5
2.0
2.5
PHOTON ENERGY (keV)
(b)
EMISSION (TW cm^{-2}eV^{-1}sr^{-1})
10^{-1}
10^{-2}
10^{-3}
10^{-4}
10^{-5}
0.0
0.5
1.0
1.5
2.0
2.5
PHOTON ENERGY (keV)

Fig.IV-4

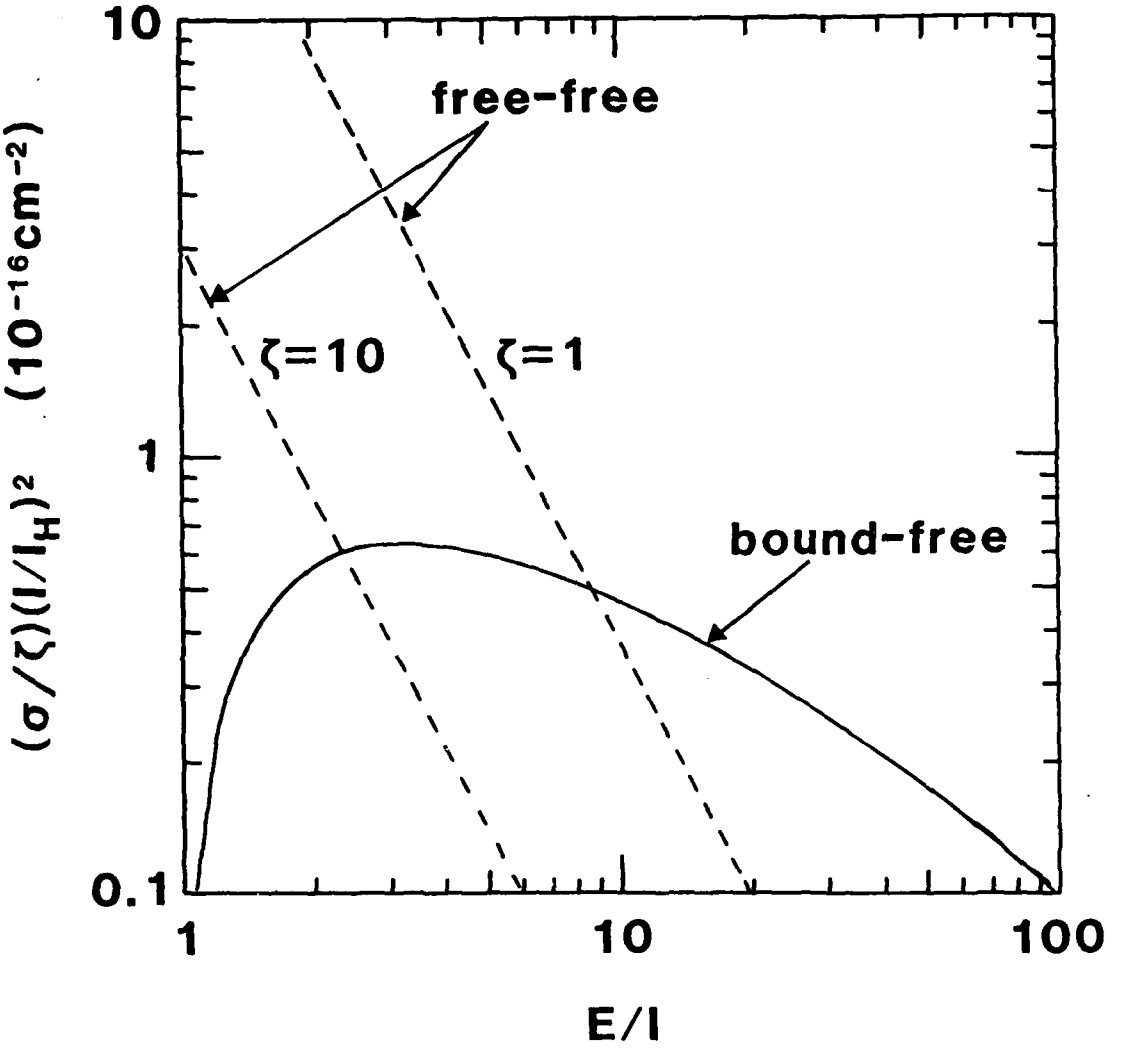
10
1
0.1
1
10
100
E/I
$(\sigma/\zeta)(I/I_H)^2$ $(10^{-16}cm^{-2})$
free-free
ζ=10
ζ=1
bound-free

Fig.V-1

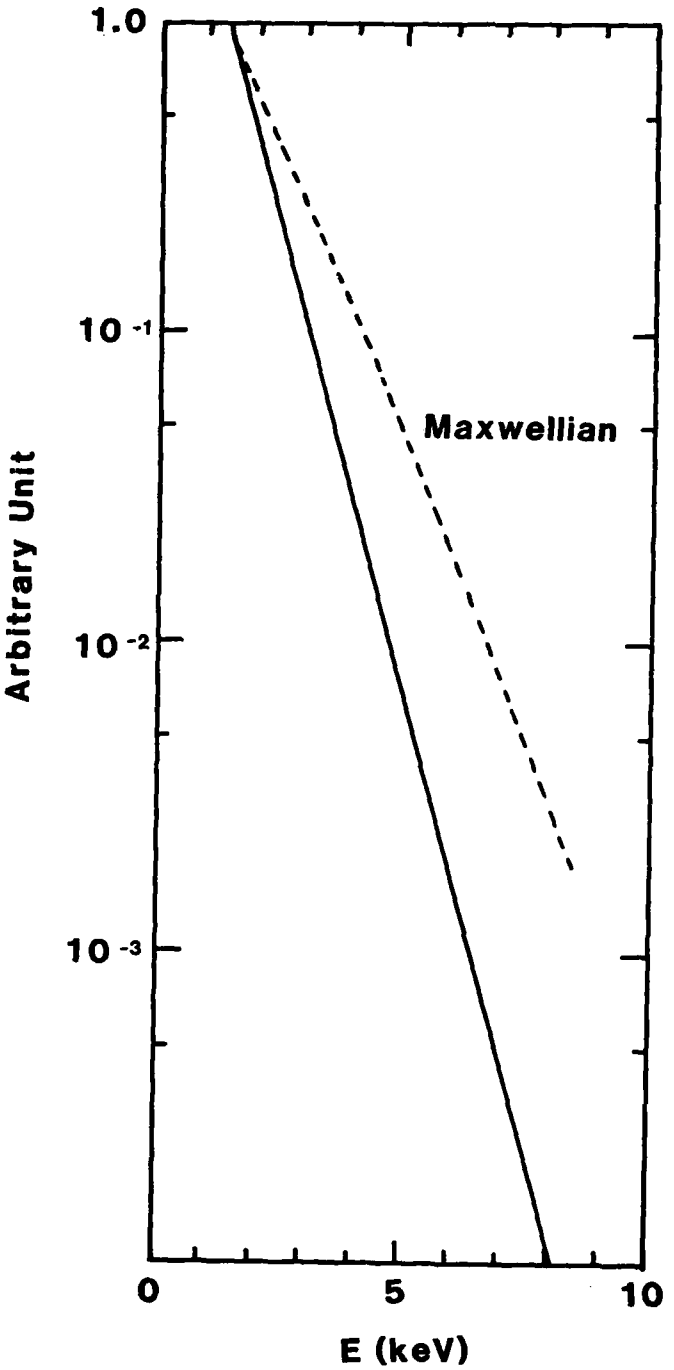

Fig.V-2

INDEPENDENT PARTICLE TIMESTEPS

Alex Friedman
Lawrence Livermore National Laboratory

Presented at the
Second US-Japan Workshop on Advanced Plasma Modeling,
Nagoya, Japan, March 23-26, 1987.

A long-standing goal in plasma simulation has been a method which could treat both detailed kinetic physics and smooth large-scale physics in an efficient and natural way. Until recently, particle simulations were applied almost exclusively to problems of "microscopic" physics, where only a small part of the plasma was modeled. With the advent of implicit particle simulation techniques,[1-5] one can now treat systems of many Debye lengths and follow them for many plasma oscillation times. However, the price paid for this capability is a restriction on the allowed spatial resolution (an accuracy constraint). Thus, at the current state-of-the-art (e.g., in codes such as TESS[6] or AVANTI[7]) a small timestep is still necessary whenever the system incorporates a physically-important small spatial or temporal scale anywhere within its domain.

We are working to develop a new particle-in-cell plasma simulation technique which relaxes these restrictions and would be suitable for strongly inhomogeneous problems involving a wide range of space and time scales. The plasma in any part of phase space would be advanced on its own natural scales. Of course, it seems only natural to advance each particle with its own, independent, series of timesteps; one could imagine using (for example) an ODE solver such as LSODE. The major difficulty in doing this has been the necessity of processing the particles in synchrony due to the requirement of a self-consistent field. We have developed in outline an algorithm which may overcome this difficulty. The code would advance the particles in blocks k, each with an associated timestep Δt_k. For each region of phase space, the nominal timestep (and possibly the mesh spacing) could be chosen in an adaptive manner. A major improvement in economy comes about because the majority of the particles are not processed during any given step; for suitable problems this gain may be two orders of magnitude.

There are many areas of plasma physics where such a capability would be highly desirable, including sheaths at the interface of a plasma with a probe or wall, collisionless shocks, double layers, and a wide variety of astrophysical problems. Even in a relatively tractable problem such as the bump-on-tail instability, significant gains might be realized by pushing only the fast particles with a small timestep; the more numerous bulk particles would be advanced less frequently. Similar methods might prove applicable to problems of gravitating systems and to particle-in-cell fluid modeling.

In the scheme we are testing, particles are advanced only every $j = 2^m$ steps (for some integer $m > 0$) if they reside in a region of phase space where there are no large-amplitude short-wavelength fields ($kv\Delta t$ and $\omega_{trap}\Delta t$ are moderate). In such a region we may additionally employ a coarse mesh or strong

spatial filtering. The large timestep used in such a region should help avoid the finite-grid instability common to explicit codes with coarse meshes.

The direct-implicit field equation is: $\nabla\cdot(1+\chi)\nabla\phi = \rho$, with $\chi(x) = \frac{1}{2}\omega_p^2\Delta t^2$ and $\rho(x)$ a free-streaming density. It is solved over the entire domain every step. In this way, the deposition of charge occurs *implicitly*, one step earlier than in an explicit code. We allow a block to deposit its information j time levels ahead of the current one; this information is then interpolated backward in time to yield the data needed to produce the field a single time level ahead.

As particles move about in phase space, it is necessary to change their timesteps (move them from block to block). We allow changes in Δt by no more than a factor of 2, no matter where the particle is; we'll catch up on the next step anyhow, and the logic is simpler this way. To facilitate doubling or halving the step size "between steps", we employ a variant of the "d1" implicit particle advance with all key quantities defined at integral (not staggered) time levels. This should allow us to preserve second order accuracy in time.

A typical grid might look like:

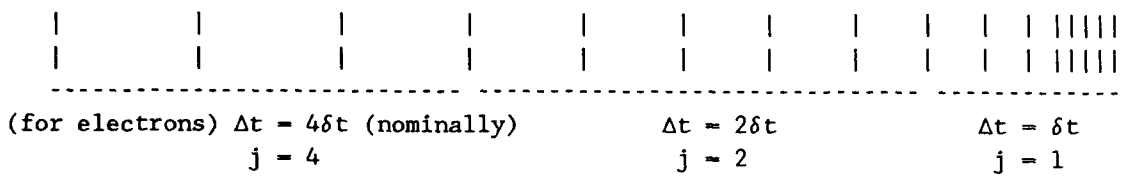

For each value of j there are j blocks:

Block e1: Electrons: push every step
Block e2: Electrons: push on even-numbered steps
Block e3: Electrons: push on odd-numbered steps
Block e4: Electrons: push on steps with (step number mod 4) = 0
Block e5: Electrons: push on steps with (step number mod 4) = 1
Block e6: Electrons: push on steps with (step number mod 4) = 2
Block e7: Electrons: push on steps with (step number mod 4) = 3

Blocks i1-i7 are similar, but contain ions.

Let us abbreviate "time-level" by "tl;" then the code at timestep 7 processes the active blocks (dots denote interpolation in time of ρ and χ):

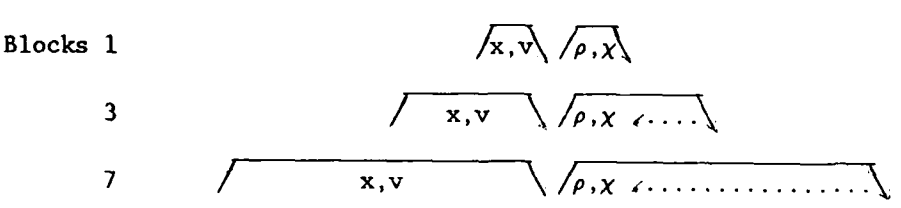

The other blocks were advanced on earlier steps, and we need only interpolate their contributions to ρ,χ back to tl 8 before the field-solve:

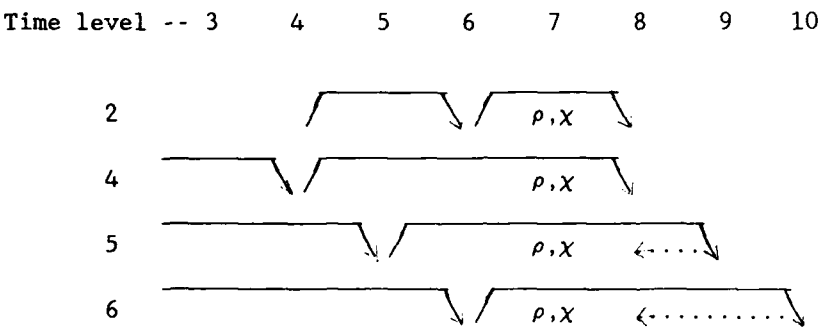

After the active particles have been pushed to tl 7 (and before their χ-contributions have been accumulated), they are moved if their (x,v) so dictate into new blocks. The re-distribution moves particles only into blocks that will be "pre-pushed" on the current step. Then the pre-push to tl 8 (or beyond) is performed. Finally, ρ and χ iare nterpolated to tl 8 (for all blocks, both active and inactive, pre-pushed beyond 8), and the field equation is solved for E_8.

We also must specify what Δt to use in the definition of the contribution to χ from a block; assuming linear interpolation of both ρ and χ, it is correct to use the Δt associated with that block (roughly, also asssociated with a region of (phase) space or a grid spacing). Thus the Δt that goes into the formula for χ is not a constant.

The algorithm may subsume explicit ion-subcycling schemes; ions would normally be processed only at the longest interval. However, initialization is simplified if all particles are placed in blocks el or il at the start, to avoid referencing a negative time-level. During the first few steps some delay in "promoting" particles into higher-number blocks must be imposed, so that (e.g.) blocks i4-7 are uniformly populated. After a few steps, blocks i1-3 will be empty.

The Revised D1 Particle-Advance Algorithm

We seek a variant of the D1 scheme with x,v defined at the same (integer) time level, to facilitate changing the timestep size. We start with the scheme as it is usually written. The "final push" is:

$$\tilde{a}_{n-1} = \tfrac{1}{2}\,[\tilde{a}_{n-2} + (q/m)E_n(\tilde{x}_n)]$$

$$v_{n-1/2} = \tilde{v}_{n-1/2} + (\Delta t/2)(q/m)E_n(\tilde{x}_n)$$

$$x_n = \tilde{x}_n + (\Delta t^2/2)(q/m)E_n(\tilde{x}_n)\ .$$

Then, the "pre-push" is:

$$\tilde{v}_{n+1/2} = v_{n-1/2} + (\Delta t/2)\tilde{a}_{n-1}$$

$$\tilde{x}_{n+1} = x_n + \Delta t\tilde{v}_{n+1/2}\ .$$

We move the computation of $\tilde{x}_{n+1}$ to the beginning of the "final push", where it becomes: $\tilde{x}_n = x_{n-1} + \Delta t \tilde{v}_{n-1/2}$. We then <u>relabel</u> $\tilde{v}_{n+1/2}$, calling it v_n (it's actually centered at tl n, formally, so this is a notational improvement). Then, we can write:

$$v_n = v_{n-1/2} + (\Delta t/2)\tilde{a}_{n-1}$$

$$= v_{n-1} + (\Delta t/2)\tilde{a}_{n-1} + (\Delta t/2)(q/m)E_n(\tilde{x}_n) \ .$$

The Algorithm in its Entirety

We enter a timestep with the particle data x_{n-1}, v_{n-1}, and $\tilde{a}_{n-2}$, and with E_n on the mesh. Strictly speaking, we should write a trivial generalization of the following, with incoming x defined at time level n-j, etc., but we write the algorithm as if j were unity for clarity. In the following, time-subscripted quantities are stored in the particle arrays, while unsubscripted quantities are used only as scratch within the particle loops. Explicitly, the algorithm is:

BEGIN THE "FINAL-PUSH" LOOP OVER BLOCKS AND PARTICLES:

0) $\Delta t = \Delta t$ (current block)

1) $\tilde{x} = x_{n-1} + \Delta t v_{n-1}$

2) $\tilde{a}_{old} = \tilde{a}_{n-2}$

3) $a = (q/m)E_n(\tilde{x})$ (interpolation of field from mesh)

4) $\tilde{a}_{n-1} = \frac{1}{2}\,[a + \tilde{a}_{n-2}]$

5) $v_n = v_{n-1} + (\Delta t/2)\tilde{a}_{n-1} + (\Delta t/2)a$

6) $x_n = \tilde{x} + (\Delta t^2/2)a$

7) Enforce particle b.c.'s; reflect or absorb or shift by one period.

8) If particle has moved to a point in phase space where $\Delta t(x_n, v_n) \leq \Delta t_{block}/2$, set $\tilde{a}_{n-1} = \frac{1}{2}\,[a + \tilde{a}_{n-1}]$, and set "new block" flag.

9) If particle has moved to a point in phase space where $\Delta t(x_n, v_n) \geq 2\Delta t_{block}$, set $\tilde{a}_{n-1} = \tilde{a}_{old}$, and set "new block" flag.

At this point we EXIT THE "FINAL-PUSH" LOOP.

We then treat the special cases:

10) Sort flagged particles into new blocks.

11) Inject any new particles by adding them to the appropriate blocks.

At this point we BEGIN THE "PRE-PUSH" LOOP OVER BLOCKS AND PARTICLES:

12) Update ρ, χ arrays associated with the current block at tl n, using data from the individual particles which change blocks.

13) $\bar{x} = x_n + \Delta t_{block}\, v_n$

14) Using $\bar{x}$, compute ρ, χ arrays associated with the current block at tl n+1.

At this point we EXIT THE "PRE-PUSH" LOOP. We then:

15) Interpolate ρ, χ from all necessary blocks to tl n+1.

16) Execute the field-solve to obtain E_{n+1}.

ACKNOWLEDGMENTS

This work is the outgrowth of a discussion between the author, C.K. Birdsall, Bruce Cohen, and Richard Procassini on new ideas for bounded plasma simulation. This work was performed under the auspices of the U.S. Dept. of Energy by the Lawrence Livermore National Laboratory under Contract W-7405-ENG-48.

REFERENCES

1 R.J. Mason, "Implicit Moment Particle Simulation of Plasmas," J. Comput. Phys. 41, 233 (1981).

2 J. Denavit, "Time Filtering Particle Simulations with $\omega_{pe}\Delta t >> 1$," J. Comput. Phys. 42, 337 (1981).

3 Alex Friedman, A. Bruce Langdon, and Bruce I. Cohen, "A Direct Method for Implicit Particle-in-Cell Simulation," Comments on Plasma Physics and Controlled Fusion 6, 225 (1981).

4 D.C. Barnes, T. Kamimura, J.-N. LeBoeuf, and T. Tajima, "Implicit Particle Simulation of Magnetized Plasma," J. Comput. Phys. 52, 480 (1983).

5 A. Bruce Langdon and D.C. Barnes, "Direct Implicit Plasma Simulation," in **Multiple Time Scales**, J.U. Brackbill and B.I. Cohen (Eds.), Orlando, Academic Press, 1985.

6 B.I. Cohen, M.E. Stewart, and C.K. Birdsall, "Direct Implicit Particle Simulation of Tandem Mirrors," Proc. 11th Int. Conf. on Numerical Simulation of Plasmas, Montreal, Canada, June 25-27, 1985.

7 D.W. Hewett and A.B. Langdon, "Electromagnetic Direct Implicit Plasma Simulation," J. Comput. Phys., August 1987 (updated reference for UCRL-94591).